Master Thesis

Quantifying Unsteady Surface Pressure Fluctuations Induced by a Propeller Slipstream Using a Flexible PCB Measurement Device

Prantik Dutta (5966159)

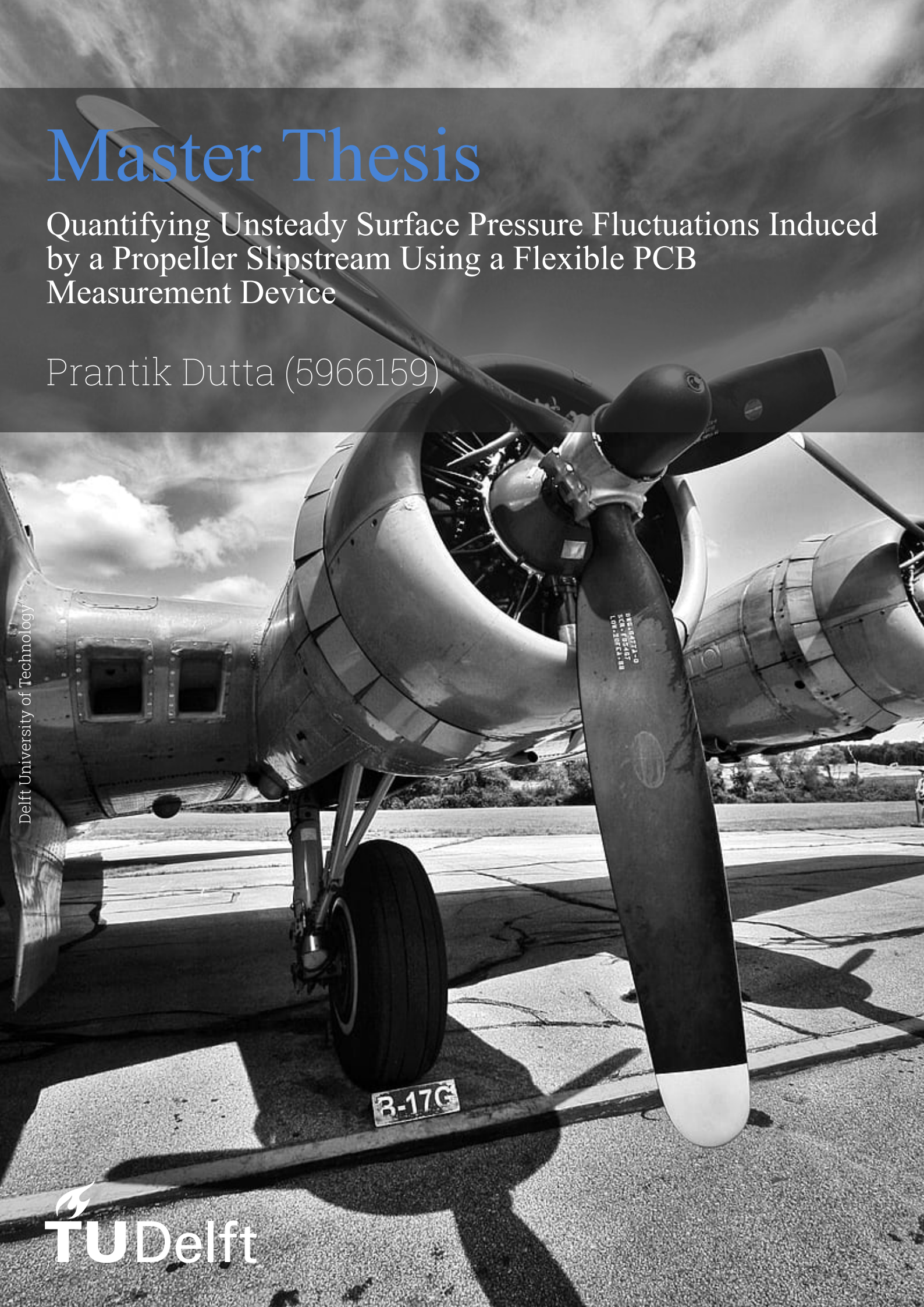

Delft University of Technology

TU Delft

Master Thesis

Quantifying Unsteady Surface Pressure Fluctuations Induced by a Propeller Slipstream Using a Flexible PCB Measurement Device

by

Prantik Dutta (5966159)

For obtaining the degree of Master of Science in Aerospace Engineering at Delft University of Technology

Supervisor(s):	Dr. ir. T. Sinnige Dr. ir. D. Ragni
Thesis Committee:	Dr. ir. T. Sinnige Dr. ir. D. Ragni Dr. ir. A. H. van Zuijlen
Thesis Duration:	Nov. 2024 – Aug. 2025
Faculty:	Faculty of Aerospace Engineering, TU Delft
Cover:	https://www.peakpx.com/en/hd-wallpaper-desktop-gowgo

TU Delft

(This page has intentionally been left blank.)

Acknowledgement

First and foremost, I would like to express my deepest gratitude to my parents for their unwavering support throughout my life. This journey would not have been possible without my father's courage to encourage me to dream freely and pursue my passion for aerospace in a foreign nation, always reassuring me that he had my back. To my mother, who taught me the true meaning of sacrifice and hard work, and who continues to be my home in every sense of the word — thank you. I am also grateful to my younger brother, whose determination and triumphs in the face of his own challenges have been a constant source of inspiration.

I am grateful to all my family, friends and teachers in India and in Delft who made stressful situations easier to bear. A special thanks to the AWE support group — my fellow batch mates and to the small Assamese community in the Netherlands for being my strength on days when I felt lost. Your presence meant a lot to me.

I would like to sincerely thank my supervisors, Dr. Tomas Sinnige and Dr. Daniele Ragni, for their guidance and encouragement throughout this thesis. Tomas' insightful feedback and his research have continuously inspired and shaped my work. Dani's detailed reviews consistently pushed me to improve and refine every aspect of my thesis. A special word of thanks goes to Paolo Comunian for helping and guiding me throughout the entire experimental campaign. This work would not have been possible without their guidance.

Last but not least, I thank my beloved Mahadev for his blessings and for always watching over me and my family.

Prantik Dutta
প্রান্তিক দত্ত

Delft, August 2025

Abstract

With the resurgence of interest in propeller-powered aircraft for short-haul and regional missions, understanding the aerodynamic interaction between propellers and nearby surfaces has become increasingly crucial. While propellers offer superior propulsive efficiency and sustainability benefits, their integration introduces complex unsteady flow phenomena that remain insufficiently explored. Additionally, concepts related to regenerative braking and the negative thrust regime aim to harness the full potential of propellers in the pursuit of sustainable aviation. However, the interactions are more complex in the negative thrust regime and need to be accounted for.

This study investigates the unsteady aerodynamic effects of a pusher-propeller operating upstream of a downstream airfoil, with a focus on both positive and negative thrust regimes. A flexible PCB embedded with microphones and pressure sensors was used to capture unsteady surface pressure fluctuations across different operating conditions. The motivation stems from the limited understanding of unsteady surface pressure fluctuations in negative thrust conditions.

The experimental campaign was conducted in two wind tunnel labs: the M-Tunnel and the Small Low-Turbulence Tunnel in the Low-Speed Wind Tunnel Laboratory of Delft University of Technology, Netherlands. The research was carried out in two experimental phases.

In the first phase, the device was validated to verify the response of the microphones and the pressure sensors. A known tonal excitation case, along with a case involving an upstream cylinder, was conducted to assess whether the results aligned with theory and expected trends from the literature. These validation experiments confirmed the device's capability to capture unsteady flow behaviour. However, certain limitations, such as overshoots in measured pressure data and restricted chordwise and spanwise resolution, were encountered.

The second phase was conducted in the Small Low-Turbulence Tunnel featuring a fixed airfoil section downstream of a rotating propeller. The device, comprising the microphones and BMP390 pressure sensors, was wrapped around the leading edge of the airfoil to measure pressure fluctuations across the airfoil surface. Initial validation confirmed the reliability of the device in measuring the flow in the propeller slipstream, with good agreement with results from the literature. Comparative analysis was performed across multiple cases, including nacelle-only baselines and propeller-on conditions at two different advance ratios. In the positive thrust regime, the propeller generated a strong tip vortex trace, which significantly influenced the laminar separation bubble and led to elevated pressure fluctuations and peaks at the tonal harmonic of the blade passage frequency. In contrast, the negative thrust regime featured a weaker tip vortex trace and a broadband-dominated spectrum, with reduced suction observed on the upper surface due to lower dynamic pressure in the slipstream.

The study also highlights that the influence of the propeller slipstream extends well beyond its boundary across the span of the airfoil model. Key limitations included discrepancies in the data measured by two rows of microphones due to surface mounting issues.

Overall, the device proved to be a valuable measurement tool for investigating the unsteady surface pressure fluctuations associated with propeller–wing interaction. The insights gained contribute to a better understanding of surface pressure fluctuations on a body immersed in a propeller slipstream, particularly in energy-harvesting operating regimes. Recommendations for future work include improving sensor mounting fidelity, increasing chordwise resolution, and incorporating time-resolved flow visualisation techniques to complement the surface pressure measurements and provide additional insight into the spatial and temporal evolution of the flow field.

Contents

Abstract vi

Nomenclature x

List of Figures xvii

1 Introduction 2
- 1.1 Comparison of Tractor and Pusher Propeller Configurations . . . 3
- 1.2 Propeller Slipstream-Induced Effects . . . 5
- 1.3 Propellers in Negative Thrust Regime . . . 10
- 1.4 Gaps and Motivation . . . 15
- 1.5 Research Aim and Objectives . . . 15
- 1.6 Thesis Outline . . . 16

2 Methodology 18
- 2.1 The Measurement Device: Sensor-Embedded Flexible PCB . . . 18
- 2.2 Validation of the Device: The First Experiment . . . 19
  - 2.2.1 Overview of the Test Cases . . . 19
  - 2.2.2 Wind Tunnel Facility . . . 19
  - 2.2.3 Blockage Correction . . . 20
  - 2.2.4 Experimental Setup and Test Model . . . 21
- 2.3 Propeller Wake-Wing Interactions: The Second Experiment . . . 24
  - 2.3.1 Overview of the Test Cases . . . 24
  - 2.3.2 Wind Tunnel Facility . . . 24
  - 2.3.3 Blockage Correction . . . 25
  - 2.3.4 Experimental Setup and Test Models . . . 26
- 2.4 Data Processing . . . 29
  - 2.4.1 Power Spectral Density (PSD) . . . 29
  - 2.4.2 Root Mean Square of Pressure Fluctuations (p_{rms}) . . . 31
  - 2.4.3 Phase-Locked Averaging (PLA) . . . 31

3 Validation of the Device: The First Experiment Results 34
- 3.1 Validation of the Microphones . . . 34
  - 3.1.1 CASE A: Known Tone Excitation . . . 34
  - 3.1.2 Calibration of the Microphones . . . 36
  - 3.1.3 CASE B: Vortex Shedding Response from Upstream Cylinder . . . 37
- 3.2 Validation of the Pressure Sensors I . . . 38

4 Propeller Wake-Wing Interactions: The Second Experiment Results 41
- 4.1 Validation of the Pressure Sensors II . . . 42
- 4.2 Investigation of Row-wise Discrepancies in Microphone Response . . . 43
  - 4.2.1 p_{rms} Characteristics and Discrepancies . . . 44
  - 4.2.2 Influence of LSB and Spectral Trends Across Microphone Rows . . . 45
- 4.3 CASE09 (Nacelle ONLY, $0°\alpha$) and CASE04 (Nacelle ONLY, $6°\alpha$) . . . 48

4.4 CASE06 ($0.8J$, $30°\beta$ and $0°\alpha$) . . . 51
4.4.1 Suction Side . . . 51
4.4.2 Pressure Side . . . 55
4.5 Positive and Negative Thrust Cases at $J = 1.8$ . . . 56
4.5.1 Suction Side . . . 56
4.5.2 Slipstream-LSB Interaction Within the Propeller Slipstream . . . 61
4.5.3 Slipstream-LSB Interaction Beyond the Propeller Slipstream . . . 64

5 Conclusions and Recommendations **69**

6 Limitations of the Study **72**

References **74**

A Appendix **79**
A.1 Control and DAQ Interfaces . . . 79
A.2 TUD-XPROP (Ø406.4 mm): Propeller Performance . . . 81
A.3 Calibrated Results of the 18 Microphones . . . 81
A.4 CASE B Plots . . . 82
A.5 Pressure Sensors Validation . . . 83
A.6 Second Experiment Results . . . 84
A.7 The High Frequency Harmonics . . . 87
A.8 Blockage Correction Tables . . . 88

Nomenclature

List of Abbreviations

Abbreviation	Definition
AoA	Angle of Attack
AR	Aspect Ratio
BL	Boundary Layer
BNC	Bayonet Neill-Concelman
BPF	Blade Passage Frequency
DAQ	Data Acquisition
DFT	Discrete Fourier Transform
FFT	Fast Fourier Transform
FPGA	Field Programmable Gate Array
IU	Inboard-Up
LBL	Laminar Boundary Layer
LE	Leading-edge
LSB	Laminar Separation Bubble
LSL	Low Speed Laboratory
OU	Outboard-Up
NACA	National Advisory Committee for Aeronautics
PC	Personal Computer
PCB	Printed Circuit Board
PLA	Phase-locked Averaging
PSD	Power Spectral Density
PIV	Particle Image Velocimetry
PP	Pusher-Propeller
RANS	Reynolds-averaged Navier-Stokes
RMS	Root Mean Square
RPM	Revolutions per Minute
RPS	Revolutions per Second
SLT	Small Low-Turbulence
SPL	Sound Pressure Level
TBL	Turbulent Boundary Layer
TDMS	Technical Data Management Streaming
TE	Trailing-Edge
TP	Tractor-Propeller
UV	Ultra Violet
WT	Wind Tunnel

List of Symbols

Symbol	Definition	Unit
α	Angle of Attack	$[°]$
β	Blade Pitch Angle	$[°]$
γ	Propeller Inflow Angle	$[°]$
η	Efficiency	$[-]$
μ	Dynamic Viscosity	$[kgm^{-1}s^{-1}]$
ϕ	Phase Angle	$[°]$
ρ	Density	$[kgm^{-3}]$
τ	Non-Dimensional Time	$[-]$
τ_1	Tunnel/Model Factor	$[-]$
$\emptyset$	Diameter	$[mm]$
κ_1	Body Shape Factor	$[-]$
B/H	Breadth-to-Height Ratio	$[-]$
c	Chord	$[mm]$
C_f	Coefficient of Skin Friction	$[-]$
C_L	Coefficient of Lift	$[-]$
C_p	Coefficient of Pressure	$[-]$
C_p'	Unsteady Coefficient of Pressure	$[-]$
C_P	Coefficient of Power (referenced to n)	$[-]$
C_T	Coefficient of Thrust (referenced to n)	$[-]$
Dia_{prop}	Diameter of Propeller	$[mm]$
G	Microphone Gain	$[-]$
J	Advance Ratio	$[-]$
L/D	Lift-to-Drag Ratio	$[-]$
L'	Lift per unit Span	$[Nm^{-1}]$
M	Mach Number	$[-]$
n	Rotational Speed of Propeller	$[s^{-1}]$
N_B	Number of Blades	$[-]$
p	Pressure	$[Pa]$
p_∞	Freestream Pressure	$[Pa]$
p_i	Instantaneous Pressure	$[Pa]$
P_C	Coefficient of Power (referenced to q_∞)	$[-]$
p_{rms}	Root Mean Square of Pressure	$[Pa]$
q_∞	Freestream Dynamic Pressure	$[Pa]$
R	Propeller Radius	$[mm]$
Re	Reynolds Number	$[-]$
s	Raw Mic Signal	$[Pa]$
St	Strouhal Number	$[-]$
St_C	Strouhal Number at Chord	$[-]$
T	Time Period	$[s]$
T_C	Coefficient of Thrust (referenced to q_∞)	$[-]$
t/c	Thickness-to-Chord Ratio	$[-]$
t_{TE}	Thickness at Trailing Edge	$[mm]$
U_∞	Freestream Velocity	$[ms^{-1}]$
V_∞	Freestream Velocity	$[ms^{-1}]$
V_{eff}	Effective Velocity	$[ms^{-1}]$

List of Figures

1.1 Lift and drag values for different spanwise locations of the propeller **[6]**. . . . 5
1.2 Shed vorticity at the blade trailing-edge and the vortex system of the propeller slipstream **[17]**. . 6
1.3 (a) Spanwise shear for power-absorbing case (J = 1.0, α_{wing} = 5°), (b) Spanwise shear for power-output case (J = 0.36, α_{wing} = 10°) **[4]**. . . . 6
1.4 Propeller-slipstream tube **[22]**. . . . 7
1.5 (a) Illustration of the slipstream disturbance on the airfoil **[12]**. (b) One complete blade passage cycle **[23]**. . . . 8
1.6 PLA at microphones located along the convecting tip vortex for (a) Advancing side, and (b) Retreating side **[20]**. . . . 9
1.7 Power spectral density for transducer 6, near the region of tip-vortex impingement **[24]**. . . . 9
1.8 (a) Transducer 3. (b) Transducer 10. PSD for transducers 3 and 10 placed farther away from the tip-vortex impingement region **[24]**. . . . 10
1.9 The velocity triangles corresponding to the airfoil section corresponding to the (a) propulsive (positive thrust) regime, (b) braking (negative thrust) regime, and (c) regenerative (negative thrust and torque) regime **[25] [26]**. . . . 11
1.10 Adapted from **[26]**. Flow visualisation using C_f and shear lines (RANS) at J = 0.8 and T_C = 0.09. 11
1.11 Velocity triangle and blade forces in the regenerative regime at equal α for (a) low β, low J, and (b) high β, high J **[25].** . . . 12
1.12 Distribution of blade loading in terms of thrust and power coefficients for the isolated propeller case (based on RANS simulations) **[26]**. . . . 13
1.13 Coefficients of power and thrust versus advance ratio for an isolated propeller (RANS and XROTOR) **[26]**. . . . 13
1.14 Radial distribution of axial and tangential velocity **[25]**. . . . 14
1.15 Thesis Outline. . . . 16

2.1 The device and its components: (a) BMP390 Pressure sensor and Knowles SPW0690LM4H-1 Microphone, (b) the device. . . . 19
2.2 (a) M-Tunnel, (b) M-Tunnel test section. . . . 20
2.3 NACA $63_3 - 018$ airfoil with axis reference from the TE **[36][37]**. . . . 21
2.4 (a) Airfoil model without the removable TE, (b) Extendable span parts. . . . 21
2.5 (a) Full layout of the device, (b) Illustration of the layout of the device when wrapped around the LE of the airfoil model (suction side view). The illustration is not to scale; sensor dimensions and coordinates are exaggerated for clarity. However, the relative ordering and arrangement of the microphones and pressure sensors accurately reflect the physical configuration. Circles represent the microphones and squares represent the pressure sensors, with their respective channel numbers annotated. . . . 22
2.6 (a) CASE B setup, (b) CASE B masked model. . . . 23
2.7 SLT test section. . . . 25

2.8 (a) Isometric view (nacelle-only configuration) of the propeller rig and downstream airfoil model. Other components of the test section are omitted for clarity. (b) Technical drawing of the TUD XPROP-S propeller (Ø203.2 mm) **[39]**. (c) Technical drawing of the rotatable sideplate used for α control. . . . 26
2.9 (a) View of the test section with the nacelle and airfoil model installed. The propeller is not mounted in this configuration, illustrating the nacelle-only case. (b) Clamping mechanism of the propeller rig showing the horizontally mounted sting and the X-beams used to vary the vertical position for spanwise sampling. . . . 27
2.10 Illustration of the device layout when wrapped around the LE of the airfoil model (suction side view). The illustration is not to scale; sensor dimensions and coordinates are exaggerated for clarity. However, the relative ordering and arrangement of the microphones and pressure sensors accurately reflect the physical configuration. Circles represent the microphones and squares represent the pressure sensors, with their respective channel numbers annotated. The propeller shown is for illustrative purposes only and does not represent the geometry or specifications of the TUD XPROP-S. . . . 27
2.11 Blade chord and pitch distributions of the TUD XPROP-S: (a) $30°\beta$ **[38]**, (b) $45°\beta$ **[39]**. (c) Photographs of the three TUD XPROP-S propellers used in the study. Results are presented only for the two configurations relevant to this work. . . . 28
2.12 Oil-Flow visualisation setup. . . . 29
2.13 Identification of propeller revolutions based on the rising edges from Sync54 channel data. . . . 31
2.14 The conventions for the retreating and advancing blade sides with respect to the airfoil model. Positive values of y/R (spanwise locations on the airfoil normalised by propeller radius) correspond to the retreating blade side of the propeller, while negative values correspond to the advancing blade side for the suction side, and vice versa for the pressure side. The arrows denote the direction of propeller rotation as viewed from the TE of the airfoil model. . . . 32

3.1 PSD of the signal from Microphone 0 and the corresponding fundamental frequency and the third harmonic. . . . 35
3.2 Time-domain analysis of Microphone 1 for the known tone of 500 Hz at 90.10 ms for 10 ms. . . . 36
3.3 SPL of the signals from the first four microphones on the device after applying the respective gain values. . . . 37
3.4 PSD of Mic 7 for CASE B at $V_\infty = 20\,\mathrm{m/s}$. . . . 38
3.5 C_p distribution for NACA $63_3 - 018$ at $\alpha = 6°$ and $V_\infty = 20$m/s. . . . 39
3.6 Illustration of the device mounted on the airfoil model. The circles represent the microphones, while the squares depict the pressure sensors. This figure highlights the protrusion of the pressure sensors from the surface. The protrusion height has been intentionally exaggerated for visual clarity. This figure is for illustrative purposes only and not drawn to scale. . . . 39

4.1 (a) Suction side. (b) Pressure side. Illustration of the device layout when wrapped around the LE of the airfoil model (counter-clockwise propeller rotation). The illustration is not to scale; sensor dimensions and coordinates are exaggerated for clarity. However, the relative ordering and arrangement of the microphones and pressure sensors accurately reflect the physical configuration. Circles represent the microphones and squares represent the pressure sensors, with their respective channel numbers annotated. The chordwise coordinates of the microphones and pressure sensors on the suction and pressure sides differ in the actual setup. This schematic is intended solely as a simplified representation of the actual setup. The propeller shown is for illustrative purposes only and does not represent the geometry or specifications of the TUD XPROP-S. The direction of counter-clockwise rotation of the propeller is annotated with arrows, as viewed from the respective sides. . . . 42
4.2 The placement of the Kapton tape on the device as viewed from the pressure side of the airfoil model. . . . 42

4.3 Comparision of C_p-Distribution between XFOIL predictions, pressure taps data and device measurements for CASE12 (Nacelle only, 9° α). The dashed black line represents the XFOIL solution. and the blue line corresponds to the pressure taps data. Black circles indicate the data from the pressure sensors of the flexible PCB device. The data is plotted against the normalised chordwise position. For clarity: SES (Sensor Embedded Sleeve) in the figure legend denotes the flexible PCB device (referred to simply as the device.) . . . 43
4.4 Oil-flow visualization for CASE04 (suction side). The red rectangle indicates the region used for p_{rms} analysis. The black circle and the white circle denote the location corresponding to the PSD measurements for the upper row mic. The white circle particularly corresponds to a location in the region influenced by the nacelle wake. . . . 44
4.5 RMS of unsteady pressure fluctuations for CASE04 (suction side). The annotated point denotes the location corresponding to the PSD measurements of the upper and middle row of microphones. 44
4.6 p_{rms} plot of the three rows of microphones for CASE04 suction side. The results correspond to the region highlighted in the oil-flow image across different spanwise positions and at $x/c = 0.370$. The upper and mid mics used for the PSD analysis are annotated here. The shaded overlapping regions (Regions A and B) extend between their respective coloured dashed lines. For Region C, the overlap is defined by the left dashed line of Region B (purple) and the right dashed line of Region A (green), as seen in the figure. . . . 45
4.7 Illustration of the laminar separation bubble **[47]**. . . . 45
4.8 (a) Mic 8 ($y/R = 0.55$), (b) Mic 9 ($y/R = 0.59$). PSD at $x/c = 0.370$ for CASE04 (suction side). The PSD x-axis is expressed in terms of the chord-based Strouhal number St_C. . . . 46
4.9 (a) Spectra of the velocity fluctuations in the streamwise direction. (b) Spectra of the surface pressure fluctuations **[47]**. . . . 46
4.10 PSD for microphone Mic 8 ($y/R = 0.078$) at $x/c = 0.370$ for CASE04 (Suction side). The PSD x-axis is expressed in terms of the chord-based Strouhal number St_C. This spanwise position is located in the region influenced by the nacelle wake and can be referenced in Fig. **4.4** and Fig. **4.5**. 47
4.11 p_{rms} plot of the three rows of microphones for CASE04 suction side. The results correspond to the region highlighted in the oil-flow image across different spanwise positions and at $x/c = 0.620$. The shaded overlapping regions (Regions A and B) extend between their respective coloured dashed lines. For Region C, the overlap is defined by the left dashed line of Region B (purple) and the right dashed line of Region A (green), as seen in the figure. The scale is adjusted for visible comparison with Fig. **4.6**. **Note:** Although the figure title mentions "Upgoing," this plot includes both upgoing (retreating) and downgoing (advancing) sides for the suction surface. 47
4.12 (a) CASE09 (nacelle only case at 0°α), (b) CASE04 (nacelle only case at 6°α). Oil-flow visualization for CASE09 and CASE04 (suction side). The red rectangle indicates the region used for p_{rms} analysis. . . . 48
4.13 RMS of unsteady pressure fluctuations for CASE09 and CASE04 (suction side) for the upper row of microphones. . . . 49
4.14 PSD for (a) Mic 6 (LBL), (b) Mic 8 (LBL) and (c) Mic 10 (separated shear layer) at $y/R = 0.91$ for CASE09 (Suction side). The PSD is expressed as a function of the chord-based Strouhal number St_C. . . . 50
4.15 PSD for (a) Mic 6 (LBL), (b) Mic 8 (separated shear layer) and (c) Mic 10 (TBL) at $y/R = 0.91$ for CASE04 (Suction side). The PSD is expressed as a function of the chord-based Strouhal number St_C. . . . 50
4.16 (a) RMS of the microphone data on the suction side (upper row of mic data). The points annotated with white circles correspond to the position that would be used for the phase-locked averaging. (b) Oil-flow visualisation for CASE06 suction side. The red rectangle indicates the region spanned by the upper row of microphones. Although the upper row is shown, the y/R axis values correspond to the middle row of microphones (and beyond), as the propeller's spanwise locations were referenced to the mid row. A fixed offset was applied to account for the spanwise separation between rows on the device. . . . 52
4.17 Wing-inflow modification due to the propeller for conventional configuration with inboard-up rotation **[53]**. . . . 52

4.18 Spanwise distribution of surface pressure coefficient (C_p) on the suction side of the airfoil model for CASE06 ($J = 0.8$, $30°\beta$, $0°\alpha$) and CASE09 (nacelle-only, $0°\alpha$). The results are shown for three chordwise pressure sensor locations ($x/c = 0.165$, 0.370, and 0.620). Each pressure sensor is denoted as 'P' followed by its sensor number. 53
4.19 Phase-averaged waveforms on the suction side retreating side for Mic 6 at different spanwise positions. The dashed line corresponds to a point outside the propeller slipstream. 54
4.20 PSD of the upper row of microphones on the suction side retreating blade side. (a) Outside the slipstream. (b) At the tip vortex trace. (c) Inboard blade wake region. 54
4.21 (a) p_{rms} of the microphone data on the pressure side advancing blade side (upper row of mic data). The 2 points annotated with white circles corresponds to the position that would be used for the PSD analysis. b) Oil-flow visualisation for CASE06 pressure side. The red rectangle indicates the region spanned by the upper row of microphones. Although the upper row is shown, the y/R axis values correspond to the middle row of microphones (and beyond), as the propeller's spanwise locations were referenced to the mid row. A fixed offset was applied to account for the spanwise separation between rows on the device. 55
4.22 PSD of the 2 annotated points for Mic 4 from the p_{rms} plot for the pressure side advancing blade side. (a) At the tip vortex trace. (b) At a spanwise location outside the slipstream, corresponding to a region of high p_{rms} values. 56
4.23 (a) p_{rms} of the microphone data on the suction side (upper row of mic data) for CASE03 and CASE02. The annotated point corresponds to the position that would be used for the PSD. (b) Oil-flow visualisation for CASE03 suction side. The red rectangle indicates the region spanned by the upper row of microphones. Although the upper row is shown, the y/R axis values correspond to the middle row of microphones (and beyond), as the propeller's spanwise locations were referenced to the mid row. A fixed offset was applied to account for the spanwise separation between rows on the device. 57
4.24 (a) Illustration of the device layout wrapped around the LE of the airfoil model. The highlighted region indicates the microphones used for PLA contour analysis. The sensor markers are exaggerated for clarity and do not reflect actual dimensions or precise geometry. Circular symbols represent microphones, and square symbols represent pressure sensors, with annotated channel numbers. The propeller depicted here is for illustration purposes only and does not represent the geometry or specifications of the TUD XPROP-S. (b,c) PLA contour for microphones 6, 7 and 14 at $x/c =$ 0.165 on the suction side retreating blade side for (b) CASE08, and (c) CASE03. 58
4.25 Phase-averaged waveforms on the suction side for CASE08 and CASE07 at spanwise positions corresponding to the minimum C_p' values observed along the tip vortex trace. 59
4.26 The PSD corresponding to the mic and position of the low-pressure region of the trace of the tip vortex for the suction side retreating blade side for (a) CASE02 and (b) CASE03. The location corresponding to the lowest C_p' from the PLA is used for the PSD. 60
4.27 Spanwise distribution of surface pressure coefficient (C_p) on the suction side of the airfoil model for CASE02 ($J = 1.8$, $30°\beta$, $6°\alpha$) and CASE04 (nacelle-only, $6°\alpha$). The results are shown for three chordwise pressure sensor locations ($x/c = 0.165$, 0.370, and 0.620). Each pressure sensor is denoted as 'P' followed by its sensor number. 60
4.28 Phase-averaged waveform on the suction side retreating blade sides for the two negative thrust cases at Mic 6. The spanwise location corresponding to the lowest C_p' value, identified by evaluating PLA results across multiple spanwise positions, is selected. 61
4.29 Phase-averaged waveform on the suction side retreating blade sides for CASE07 for the chordwise mics at $y/R = 0.91$. 62
4.30 (a) p_{rms} of the microphone data on the suction side (upper row of mic data). Annotated points correspond to the region of LSB influence on retreating and advancing sides. (b) Oil-flow visualisation for CASE08 suction side. The red rectangle indicates the region spanned by the upper row of microphones for the p_{rms} plot. Although the upper row is shown, the y/R axis values correspond to the middle row of microphones (and beyond), as the propeller's spanwise locations were referenced to the mid row. A fixed offset was applied to account for the spanwise distance between rows on the device. 63
4.31 p_{rms} of the microphone data on the suction side (upper row of mic data) for CASE03 and CASE02. Annotated points correspond to the region of LSB influence on the corresponding regions for both cases. 63

4.32 RMS of the microphone data on the retreating (upper row of mic data) blade side for the suction side of the airfoil. The subplots correspond to CASE03, CASE02, and CASE04, respectively. The points highlighted with white circles indicate the locations used for the PSD analyses. . . . 64
4.33 PSD of the microphone data on the retreating (upper row of mic data) blade side for the suction side of the airfoil. The subplots correspond to CASE02, CASE03, and CASE04, respectively. Mic 8 ($x/c = 0.370$) at a spanwise position of $y/R = 1.38$ is used for this analysis. 65
4.34 p_{rms} of the microphone data on the retreating (upper row of mic data) blade side for the suction side of the airfoil. The subplots correspond to CASE01 and CASE04, respectively. The annotated points indicate the locations used for the PSD analyses. 66
4.35 (a) CASE01, (b) CASE04. PSD of the microphone data on the retreating (upper row of mics data) blade side for the suction side of the airfoil. The subplots correspond to CASE01 and CASE04, respectively. Mic 8 ($x/c = 0.370$) at a spanwise position of $y/R = 1.38$ is used for this analysis. The annotated point in CASE04 indicates the frequency of the most dominant disturbance in the separated shear layer. In CASE01, the annotated peak marks the closest RPS harmonic to this frequency, indicating a possible tonal excitation. 67

A.1 (a) M-Tunnel Data interface window, (b) M-Tunnel Control interface window 79
A.2 (a) SLT Data interface window, (b) SLT Control interface window 79
A.3 Motor Control interface window used during the second experiment. 80
A.4 SES DAQ interface. 80
A.5 Performance data for TUD-XPROP (Ø406.4 mm) propeller. 81
A.6 SPL of all 18 microphones. 81
A.7 Power spectral density (PSD) of Mic 7 for CASE B at two freestream velocities. 82
A.8 Normalised running mean for pressure tap 5. 83
A.9 Comparison of C_p distribution over the suction side of the NACA $63_3 - 018$ airfoil. The plot includes data from the pressure taps, predictions from XFOIL, and measurements from the embedded pressure sensors in the device. The results show the discrepancy in the measured data for the pressure sensors of the device with respect to the pressure taps and XFOIL data. For clarity: SES (Sensor Embedded Sleeve) in the figure legend denotes the flexible PCB device (referred to simply as the device). 83
A.10 Oil-flow visualisation for CASE01 ($0.8J$, $30°\beta$, $6°\alpha$) pressure side. See Fig. **4.1** for the propeller rotation direction and conventions. 84
A.11 Phase-averaged waveforms on the pressure side advancing blade side for Mics 4, 2 and 0 at different spanwise positions across the path of the tip vortex trace as seen in Fig. **4.16**. 84
A.12 Spanwise distribution of surface pressure coefficient (C_p) on the suction side of the airfoil model for CASE02 ($J = 1.8$, $30°\beta$, $6°\alpha$) and CASE03 ($J = 1.8$, $45°\beta$, $6°\alpha$). The results are shown for three chordwise pressure sensor locations ($x/c = 0.165$, 0.370, and 0.620). Each pressure sensor is denoted as 'P' followed by its sensor number. 85
A.13 The PSD corresponding to the mic and position of the low-pressure region of the trace of the tip vortex for the suction side retreating blade side for CASE08 and CASE03. The location corresponding to the lowest C_p' from the PLA is used for the PSD. 85
A.14 The PSD corresponding to the mic and position of the low-pressure region of the trace of the tip vortex for the suction side retreating blade side for (a) CASE07 and (b) CASE02. The location corresponding to the lowest C_p' from the PLA is used for the PSD. 85
A.15 CASE06 ($0.8J$, $30°\beta$, $0°\alpha$): (a) Running mean of Mic 6 over non-dimensional time τ. (b) Absolute value of the first derivative of the running mean with respect to τ, used to quantify the rate of convergence. The corresponding PLA can be referred to from Fig. **4.19**. The scale has been adjusted for clarity. 86
A.16 CASE07 ($1.8J$, $30°\beta$, $0°\alpha$): (a) Running mean of Mic 6 over non-dimensional time τ. (b) Absolute value of the first derivative of the running mean with respect to τ, used to quantify the rate of convergence. The corresponding PLA can be referred to from Fig. **4.28**. The scale has been adjusted for clarity. 86
A.17 CASE02 ($1.8J$, $30°\beta$, $6°\alpha$): (a) Running mean of Mic 6 over non-dimensional time τ. (b) Absolute value of the first derivative of the running mean with respect to τ, used to quantify the rate of convergence. The corresponding PLA can be referred to from Fig. **4.28**. The scale has been adjusted for clarity. 86

A.18 PSD corresponding to Mic 6 at $y/R = 0.79$ for CASE09, CASE07 and CASE08. The first subplot highlights the first two harmonics of the fundamental frequency, the second subplot annotates the fourth harmonic, and the third subplot displays the second, third and fourth harmonics. 87
A.19 PSD corresponding to Mics 6, 8 and 10 at $y/R = 0.91$ for CASE04. The first subplot highlights the first two harmonics of the fundamental frequency, the second subplot annotates the third and fourth harmonics, and the third subplot displays the fourth harmonic. 88
A.20 Values of τ_1 for various tunnel shapes and configurations **[35]**. 88
A.21 Values of κ_1 for various base profiles **[35]**. 89

(This page has intentionally been left blank.)

1

Introduction

Amidst advancements in high bypass ratio turbofan engines, renewed interest in propeller-powered aircraft calls for further investigation, particularly for regional and short-haul operations, driven not only by their potential for enhanced aerodynamic and propulsive efficiency, but also by recent developments in electric and distributed electric propulsion systems [1] [2]. Propellers offer the advantage of high propulsive efficiency, approximately 10-30% higher than that of high-bypass ratio turbofans, along with reduced structural loads and drag compared to ducted engines. These features make them attractive for future fuel-efficient and environmentally sustainable aircraft designs. However, they are plagued with challenges related to noise emissions, lower speed limits and complex unsteady flow interactions with nearby surfaces [1] [3].

One key area of focus is understanding the aerodynamic interactions between rotating propeller blades and adjacent airframe components such as the wing, tail, and fuselage. Quantification of these interaction effects and the unsteady effects due to propeller integration requires further investigation. These interactions vary significantly depending on the propeller's placement. Propeller configurations are generally categorised into two primary types based on their location: tractor-propeller (TP) and pusher-propeller (PP) configurations. In a TP configuration, the propeller is mounted ahead of the wing or fuselage and generates thrust by accelerating airflow rearward from its front-mounted position. This setup causes the slipstream to interact with downstream components such as the wing, tail, or nacelle. In contrast, a PP configuration positions the propeller behind the lifting surface, where it generates thrust and pushes the aircraft forward. This arrangement allows the slipstream to impinge directly on the airfoil, often without interference from upstream structures.

Furthermore, the renewed interest in propellers aligns well with sustainability goals in the civil aviation sector. As a result, understanding the environmental impact of propeller-driven aircraft has become an increasingly important area of research and responsibility. Concepts related to regenerative braking and the negative thrust regime aim to harness the full potential of propellers in the pursuit of sustainable aviation.

The current experimental campaign investigates a PP configuration, where the propeller is positioned upstream of an airfoil test model at a distance of approximately one propeller diameter. The study focuses on propeller wake–wing interactions across positive and negative thrust regimes, using a novel measurement device to quantify unsteady pressure fluctuations. The device is a flexible PCB embedded with microphones and pressure sensors. Therefore, a discussion on the comparison between TP and PP configurations, along with the slipstream effects across different thrust regimes, is crucial. The subsequent sections discuss these slipstream-induced phenomena in detail, including comparisons between TP and PP setups and the characteristics of the negative thrust regime.

This chapter introduces the key physical phenomena that govern propeller-induced unsteady flows and establishes the motivation for the present experimental investigation. **Section 1.1** compares tractor and pusher configurations, highlighting how propeller placement influences interactions with nearby aerodynamic surfaces. **Section 1.2** outlines the unsteady flow features generated by a rotating propeller, including slipstream structure and vortex dynamics. **Section 1.3** focuses on the negative thrust regime, where reversed loading conditions on the propeller blades produce distinct slipstream characteristics under braking and regenerative operations. **Section 1.4** reviews the limitations of existing studies and measurement techniques, and presents the motivation for using a novel surface-mounted device to measure the unsteady surface pressure fluctuations on a downstream airfoil model immersed in the propeller slipstream.

After reviewing the relevant literature and identifying the associated limitations, **Section 1.5** presents the research aim and outlines the approach adopted in this study. Finally, **Section 1.6** presents the outline and structure of the report.

1.1 Comparison of Tractor and Pusher Propeller Configurations

Propeller placement has a significant influence on the nature of aerodynamic interactions with downstream surfaces. In a tractor configuration, the propeller is positioned upstream of the wing or fuselage, resulting in its slipstream interacting with structural elements before reaching the lifting surface. In contrast, a pusher configuration places the propeller aft of the wing or fuselage, allowing the slipstream to impinge directly on downstream bodies, such as the horizontal tail. Therefore, the pusher configuration presents a promising setup for the present experimental campaign, which seeks to isolate[1] and quantify slipstream-induced effects on the surface of a downstream airfoil model.

R. T. Johnston and J. P. Sullivan (1990) **[4]** investigated the asymmetric effects due to the presence of a downstream wing in a TP configuration. The flow undergoes a spanwise shearing effect, and this occurs in opposite directions on both sides of the wing. A plausible reason for this effect is the interaction of the wing with the rotational and axial components of the slipstream. Furthermore, this increases in magnitude along the chord. A maximum intensity is reached at the trailing-edge (TE). At the junction of the wing TE and the slipstream boundary, formation of strong vortices is observed due to the high spanwise pressure gradient at the TE slipstream-freestream interface.

More recently, Y. Furusawa and K. Kitamura (2020) **[5]** investigated the downstream effects of a TP configuration, highlighting the influence of slipstream interaction with the downstream wing surface. Their study revealed a linear increase in the lift coefficient (C_L) with the angle of attack (α), attributed to the suppression of flow separation on the downstream wing. This interaction also resulted in higher thrust coefficient values compared to a propeller-only[2] case. Notably, an upstream effect was also observed, where the presence of the wing increased the thrust coefficient relative to the isolated propeller case. The axial velocity plays a crucial role in thrust augmentation. However, when the tangential velocity component is redirected into the axial component, it is observed that the pressure difference between the upstream region of the propeller and the region behind it increases, thereby further augmenting the thrust. The downstream wing in a TP configuration also induces a decrease in the rotational velocity in the slipstream. The upwash induced by the wing can lead to changes in the helix angle of the propeller slipstream, and this can lead to a decrease in rotational velocity of the propeller slipstream **[6]**. An increase in the axial velocity at the wing is observed when the distance between the wing and the propeller is increased.

On the other hand, for a PP, an upstream effect was observed, wherein the thrust coefficient yielded higher values compared to the isolated propeller case and the TP case **[5]**. However, the azimuthal fluctuation was dominant in this case. This was due to the unsteady interaction between the velocity-deficit boundary layer (BL) behind the upstream wing and the propeller. For the PP, at a higher α, a separation vortex formed in the upper region of the upstream wing.

According to S. Farokhi (1989) **[7]**, the primary sources of unsteadiness for a subsonic PP are: α, the sideslip angle, wake interaction with upstream surfaces, turbulence, and engine exhausts. In particular, when a jet exhaust

[1] By isolating, it is meant that the sensitivity of upstream effects is intentionally minimised in the current setup. This is due to both experimental limitations and the specific focus of the study, which does not aim to account for changes in propeller loading due to the presence of a downstream body.

[2] Propeller-only case refers to the case without a nearby adjacent wing.

is present upstream, the propeller blades can intersect the exhaust wake twice per rotation, significantly affecting blade performance [8]. However, such jet–propeller interactions are beyond the scope of the present study.

Under unsteady conditions, pronounced peaks are observed at specific blade azimuthal positions, indicating strong phase-dependent pressure fluctuations. Time-averaged results confirm the previous finding that the thrust coefficient in the PP configuration is higher than that of both the TP and isolated propeller cases. Notably, a localised effect on the advance ratio (J) at every 180° caused a distinct localised peak in the thrust coefficient values [5]. This phenomenon is attributed to the blade periodically passing through the velocity-deficit region behind the upstream wing. However, the trend appeared to be comparatively smeared at higher α.

As mentioned earlier, the propeller-slipstream interactions with a downstream/upstream surface lead to varying aerodynamic effects. For the PP case, F. M. Catalano (2004) [9] observed that the propeller inflow significantly influences the upstream wing. It can delay both the onset of boundary layer transition and flow separation, resulting in changes to the lift and drag characteristics. These inflow effects are sensitive to the relative distance between the upstream wing and the downstream propeller [10]. Due to the delay in transition, a larger portion of the wing surface remains laminar, resulting in reduced skin friction drag. Moreover, due to the increase in the suction on the upper region of the wing, an increment in C_L values was also observed. The vertical position of the propeller with respect to the wing chord line influences the gain in suction on the upper wing surface. When the propeller is positioned higher than the wing and close to the TE, the effective incidence and camber are increased, leading to higher suction and C_L values [9] [11]. At higher α, this lift enhancement becomes more pronounced. This is an important result, as the distance between the airfoil model and the propeller in the current study is chosen to minimise upstream sensitivity, ensuring that the measured pressure fluctuations primarily reflect slipstream effects rather than mutual interference.

However, the PP configuration is also associated with increased pressure drag [10]. Although transition and turbulent separation are delayed, the flow becomes more susceptible to laminar separation. Key factors affecting the shift in the transition point include the axial distance between the propeller and the wing TE, and the vertical offset from the wing chord line, with the former playing a more dominant role due to the influence of the propeller's inflow [9]. These effects are further influenced by the α.

In contrast, the TP promotes the onset of transition, and the effect varies with respect to the number of blades (N_B). This results in the flow alternating between laminar and turbulent states (see Fig. 1.5), often occurring at the blade passage frequency (BPF) [4] [12]. R. M. Howard et al. (1985) [13] concluded that this intermittent state of turbulence is due to the viscous wake of the propeller blade. Additionally, as the laminar stability reduces, the cyclic length of this alternating state increases. As the speed changes, the pressure gradients also change, thereby affecting the stability of the laminar flow. For instance, when the speed is high, a favourable pressure gradient is expected. This will lead to an increase in the laminar stability. This increases the resistance of the laminar boundary layer (LBL) to transition to a turbulent state.

T. Sinnige et al. (2016) [14] conducted experiments to investigate installation effects in a PP configuration under angular inflow conditions. They found that the dominant pylon–propeller interaction in the PP configuration arises from the momentum deficit in the pylon wake. A non-zero α causes unsteady and periodic loads on the blade. Additionally, the pylon also induces a cyclic perturbation on the propeller blades. Impulsive changes to the α due to the pylon-wake also lead to an impulsive change in the blade lift [14]. This further affects the thrust generated by the propeller as the pylon tip vortex induces variations in the sectional α of the propeller blade. Local fluctuations in the sectional J of the blades are also observed.

These slipstream effects extend beyond the immediate wing interaction. In a PP configuration, downstream components such as the horizontal tail are also influenced by the altered flowfield. For instance, interaction with the downstream horizontal tail can lead to an increase in both the downwash angle and the local dynamic pressure, which in turn induces a nose-up pitching moment on the aircraft [15]. Under power-on conditions, especially during high thrust operation and at lower freestream velocities V_{inf}, these effects become more pronounced. The increase in dynamic pressure at the horizontal tail is also dependent on the distance between the propeller and the downstream tail. An increase in dynamic pressure implies a higher local airflow velocity, which directly impacts the aerodynamic performance and control effectiveness of the horizontal tail.

To better understand such downstream effects on control surfaces, H. Benyamen et al. (2020) [16] conducted flight tests on a modified twin-boom PP aircraft to evaluate a redesigned tail intended to mitigate the adverse effects of propeller slipstream immersion. Their findings revealed significant spanwise variation in the dynamic

pressure ratio across the horizontal tail. The variation in dynamic pressure across the horizontal tail leads to a shift in its aerodynamic centre, which can subsequently affect the aircraft's stability and control.

Varying the spanwise location of the propeller can also influence aerodynamic performance. L. Veldhuis (2004) **[6]** suggested that this effect may be attributed to the swirl induced by an inboard-mounted (IU) propeller, which reduces the influence of the wingtip vortex. This further leads to an increase in the effective aspect ratio of the wing. Hence, the L/D is increased due to a reduction in drag and an increment in the lift values **[4]**. This is shown in Fig. 1.1. However, the magnitude of this effect is often negligible for practical spanwise propeller positions. Additionally, the vertical positioning of the propeller relative to the wing has been shown to impact both lift generation and propulsive efficiency. To fully evaluate the benefits of these changes, a holistic investigation of the integration effects is required.

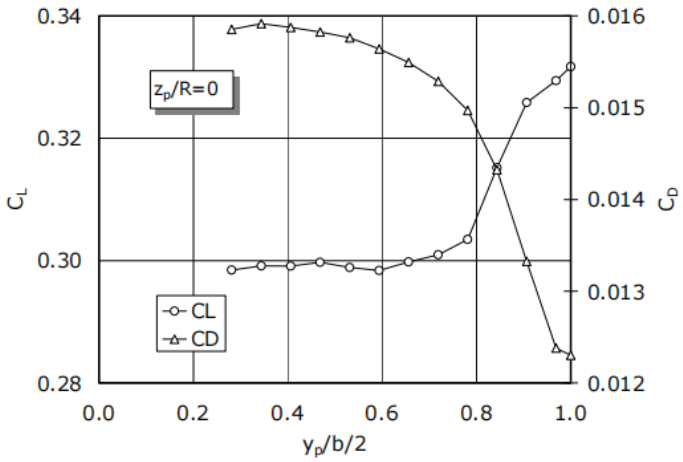

Figure 1.1: Lift and drag values for different spanwise locations of the propeller **[6]**.

Despite extensive research on the upstream effects of the PP configuration, studies focusing on the effects on downstream bodies remain comparatively limited. This is a critical gap, and the present experimental campaign specifically aims to quantify how the propeller slipstream affects unsteady surface pressure fluctuations on a downstream airfoil model.

The primary objective is to analyse the data from the microphones and pressure sensors placed at multiple chordwise and spanwise locations on the downstream airfoil model, in both positive and negative thrust conditions. These measurements will help in quantifying the spatial and phase-resolved temporal variations in pressure fluctuations induced by the propeller wake while minimising sensitivity to upstream variations in propeller loading. This is achieved by placing the airfoil one propeller diameter downstream, thereby isolating the slipstream–airfoil interaction. The detailed setup and the corresponding methodology are discussed in Chapter 2.

1.2 Propeller Slipstream-Induced Effects

Since the current study focuses on propeller slipstream–airfoil interactions, it is essential to discuss the key elements of the slipstream. Propellers are an assembly of rotating airfoils, with each blade characterised by its boundary layer effects, which influence the characteristics of the slipstream and induce unsteady interactions with downstream bodies.

The slipstream is characterised by three-dimensional unsteady effects. The helical path traced by the slipstream results from the vorticity shed along the TE of the propeller blades. This is further influenced by the axial and swirl components, which together lead to the characteristic helical structure of the propeller slipstream. This is illustrated in Fig. 1.2. Upon impinging on a downstream surface, the propeller slipstream induces unsteady surface pressure fluctuations and alters the aerodynamic loading of the downstream body. The turbulent wake also interacts with the downstream boundary layer, leading to additional unsteady effects.

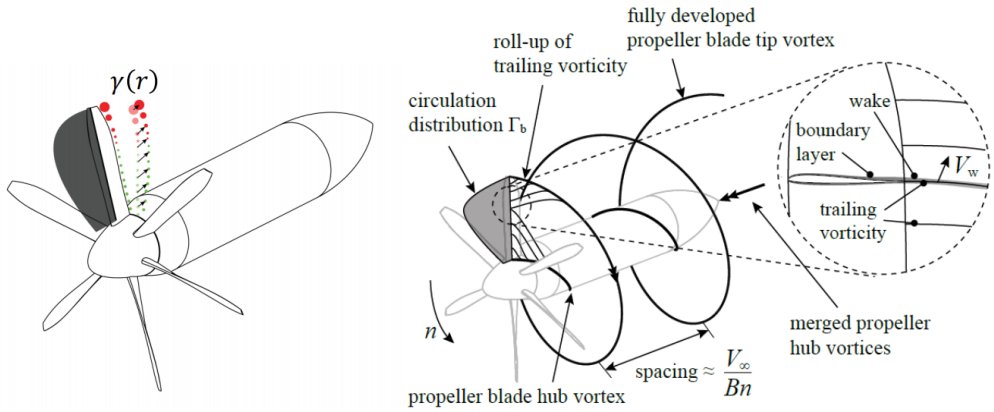

Figure 1.2: Shed vorticity at the blade trailing-edge and the vortex system of the propeller slipstream [17].

R. T. Johnston and J. P. Sullivan (1992) [18] conducted experiments on the unsteady effects in the propeller slipstream. Smoke visualisation was used to trace the tip vortex, revealing several notable results. At the leading edge (LE) of the wing downstream of the TP, a spanwise deformation of the tip vortex was observed. This was caused by the inviscid interaction occurring at the impingement location at the LE. The deformation continued until the viscous effects at the wing LE sheared the vortex filament in the spanwise direction. The induced chordwise and spanwise displacements occurred in opposite directions on the upper and lower surfaces of the wing [4]. A reduction in pressure fluctuations along the chord was also noted, attributed to the breakdown of coherent vortex structures due to increased interaction with the wing boundary layer. Additionally, depending on the direction of propeller rotation, the tip vortex was seen to stretch or thicken asymmetrically on both sides of the wing [19].

These interactions were shown to be sensitive to the propeller's operating condition. The trend for both the power-absorbing and power-output cases is illustrated in Fig. 1.3. It can be observed from Fig. 1.3 that the spanwise shear on the upper surface is directed outward, particularly on the upwash side for the power-absorbing case, whereas for the power-output case, it is outward below the wing. The horizontal space, in each image below, corresponds to the wing surface.

This is a significant observation, as the contrasting shear patterns in the two thrust regimes suggest that, with sufficient chordwise resolution, the impingement of the tip vortex and its associated shearing near the LE can be investigated to better understand the resulting surface pressure fluctuations in both power-absorbing and power-output conditions.

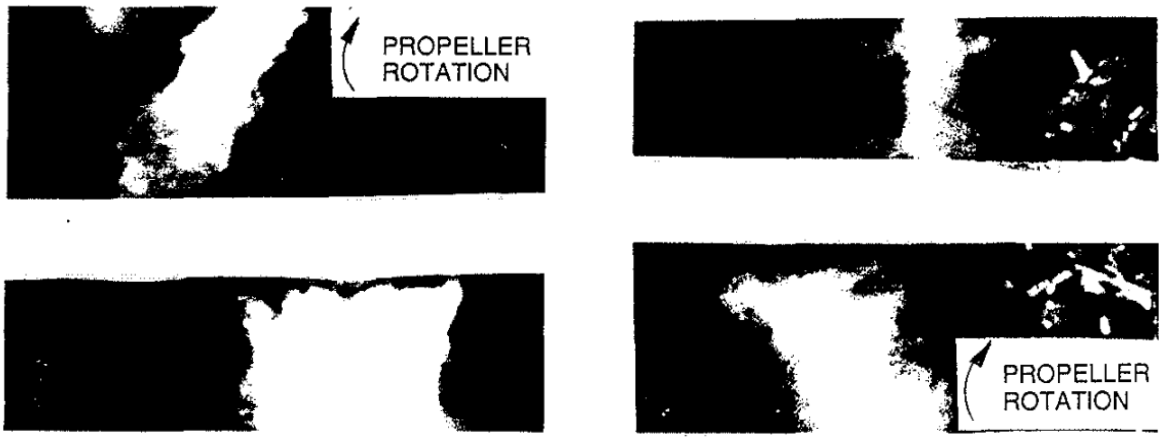

Figure 1.3: (a) Spanwise shear for power-absorbing case ($J = 1.0$, $\alpha_{wing} = 5°$), (b) Spanwise shear for power-output case ($J = 0.36$, $\alpha_{wing} = 10°$) [4].

To quantify this spanwise deformation induced by the propeller-slipstream impingement on the LE of the pylon, Particle Image Velocimetry (PIV) was conducted by T. Sinnige et al. (2018) **[20]** at three vertical positions. Phase-locked measurements were obtained to investigate the characteristics of the blade wake and the tip vortices. At the pylon LE, localised displacements were observed to occur independently of the gradual spanwise variation in the tip vortex trajectory along the pylon chord. This spanwise variation results from differences in spanwise lift across the pylon. It was also observed that the maximum amplitude of pressure fluctuations occurs near the LE region. As discussed earlier, this was due to tip vortex impingement. The amplitude then decreases in the chordwise direction, which can be attributed to viscous interactions between the vortex core and the wing BL **[20]**.

Additionally, the propeller slipstream also affects the transition on a downstream wing, as previously discussed in Section 1.1. H. Aminaei et al. (2018) **[21]** investigated a TP configuration to predict the transition behaviour over the wing. The authors observed that due to the slipstream of a TP, the location of the transition point shifted upstream near the LE. An increase in the α shifted the point even further upstream. Additionally, an increase in propeller rotational speed resulted in a larger region dominated by a turbulent boundary layer (TBL). The authors also examined the influence of TP-induced upwash on the downstream wing, wherein a reduction in upper surface pressure and an increase in lower surface pressure were observed. An opposite trend was observed in the propeller downwash for the region. In the upwash region, an increase in the local α and ${V_{eff}}^3$ leads to an increase in the C_L in that region. In contrast, in the downwash region, a reduction in the wing's local α was observed. This led to a downstream shift of the transition point toward the TE. Thus, the authors concluded that the downwash delays the transition in those regions **[21]**.

This finding is particularly relevant to the present study, which is conducted at low Reynolds numbers (Re), where the formation of a laminar separation bubble (LSB) is more likely to occur. At high J, based on the upwash and downwash from the rotating blades, the slipstream is expected to either promote or delay the onset of transition in different spanwise regions.

An image of the propeller-slipstream tube and the vortex system is shown in Fig. 1.4.

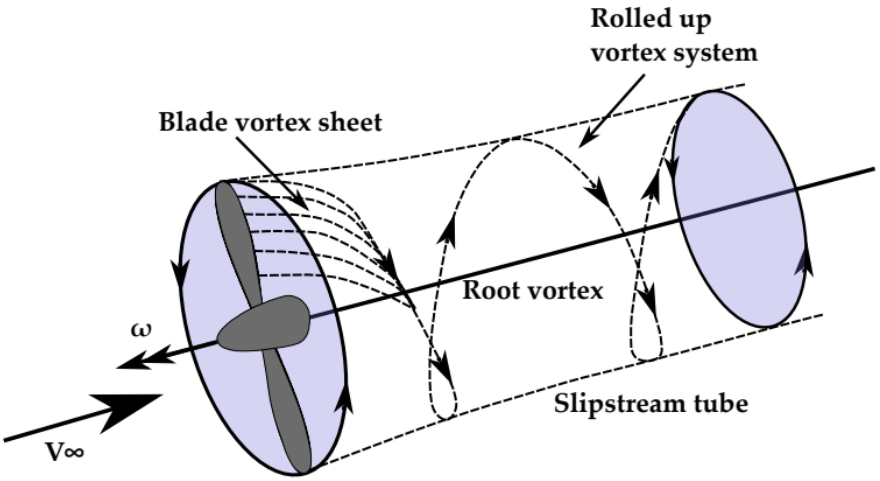

Figure 1.4: Propeller-slipstream tube **[22]**.

The important properties of the vortex formation pertaining to the current study are as follows:

1. The vorticity roll-up process in the near-field: understanding the near-field vorticity roll-up is essential to analyse the wake-induced effects on nearby surfaces. This is driven by the difference in velocity and pressure gradients created by blade motion, and this further leads to the formation of tip vortices. An upstream effect is also dominant based on the distance between nearby bodies. This upstream effect leads to changes in the blade loadin,g which further influences the blade passage effects **[22]**.

[3] $V_{\text{eff}} = \sqrt{V_{\text{ax}}^2 + V_{\text{rot}}^2}$

2. Tip-vortex: An increase in the freestream velocity will lead to an increase in the vortex spacing, whereas an increase in the N_B will lead to a decrease in the vortex spacing. Smaller tip-vortex spacing will result in a denser helical wake. This can lead to an increase in interference effects in the current study, particularly with the downstream airfoil. The pitch of the helix system is defined by J, wherein a low J corresponds to a condensed wake with the flow structures convecting slowly away from the propeller. A high J leads to a stretched wake, with the flow structures convecting rapidly away from the propeller.
3. Time-varying shaft loads: In this case, typically, an increment in the N_B can lead to a reduction in the amplitude of unsteady loads. This is primarily because of the interference between the blade signals.
4. Low static pressure inside vortex cores: Due to conservation of angular momentum (fluid rotating faster near the core), the pressure is low, and this is responsible for suction effects. These low-pressure regions can intensify the interaction effects with nearby surfaces.
5. Inside the propeller-slipstream, the flow gradients are highly complex but tend to smooth out over distance, leading to more uniform flow in the far-field. In the current study, microphones positioned at different chordwise locations can be instrumental in quantifying this effect. Additionally, the effects of the propeller slipstream extend beyond the slipstream edge. This will be analysed for the relevant test cases.

For a given condition, if the propeller geometry, blade setting, and operating condition are fixed, then the propeller-wing interference is primarily dependent on the α and the influence of the wing on the flow around the propeller **[6]**. This is particularly for a TP configuration[4].

At an α of $0°$, the propeller is axisymmetric. However, the scenario changes at a non-zero α. There are three primary consequences of this effect:

1. Unlike the constant blade loading for the $0°\alpha$ case; a non-zero α leads to periodic variation of blade loading. This is due to the net difference in the positive and negative perturbation in α and the inflow V_{eff} seen by the advancing and the retreating blades (depending on the direction of propeller rotation) respectively **[6]**. The corresponding unsteady aerodynamics also cause a phase lag.
2. Modification of propeller loads: Due to the net effect of the perturbations seen by the advancing and retreating blades, there is a net increase in time-averaged thrust, normal force and side force. The propeller loads are also affected by the J. At low values of J, the propeller blade sections are more susceptible to separation due to a high positive value of α at the blade sections.
3. Time-varying shaft loads: In this case, typically, an increment in the number of blades N_B can lead to a reduction in the amplitude of unsteady loads. This is primarily because of the interference between the blade signals. The N_B also influences the cyclic transition between laminar and turbulent flows occurring between successive blade passages. This cyclic process of the boundary layer alternating between an LBL and TBL is illustrated in Fig. **1.5 (a)**.

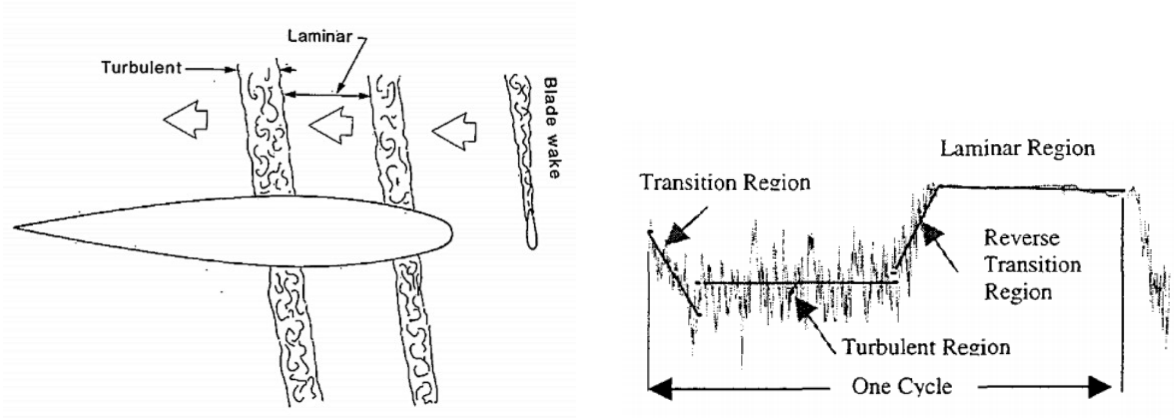

Figure 1.5: (a) Illustration of the slipstream disturbance on the airfoil **[12]**. (b) One complete blade passage cycle **[23]**.

[4]The current study focuses on the downstream effects of a PP configuration. However, due to the nature of the considered experimental setup, certain parallels can be drawn between the two configurations.

The cyclic behaviour of the BL, switching between laminar and turbulent states, is a related effect for the time-dependent case. S. J. Miley et al. (1988) **[12]** analysed the unsteady velocity profiles and the characteristics of these alternating states and concluded that the turbulent transitional state exhibited features resembling those of a relaminarizing flow, while the laminar flow showed traits similar to those of external turbulence. However, utilising a multi-blade propeller set-up can eliminate this alternating scenario due to the wake interaction of multiple blades **[9]**. A complete blade passage cycle is depicted in Fig. 1.5 **(b)**.

The unsteady aerodynamic phenomena are not only relevant from a loading perspective but also have direct implications for surface pressure fluctuations and noise generation on nearby surfaces. In their investigation of TP configurations, T. Sinnige et al. (2018) **[20]** identified the tip vortex as the dominant source of pressure fluctuations on the pylon. For time-dependent effects, a periodic pressure response was observed. This periodic nature is illustrated in Fig. 1.6 where phase-locked averaging was performed at microphones located along the convecting tip vortex. A chordwise decay of coherent structures is visible from the figure. In case of a PP configuration, the unsteady interactions can lead to the unwanted generation of noise. The noise levels in PP configurations are typically higher than those in TP configurations due to the non-uniformities in the inflow **[20]**.

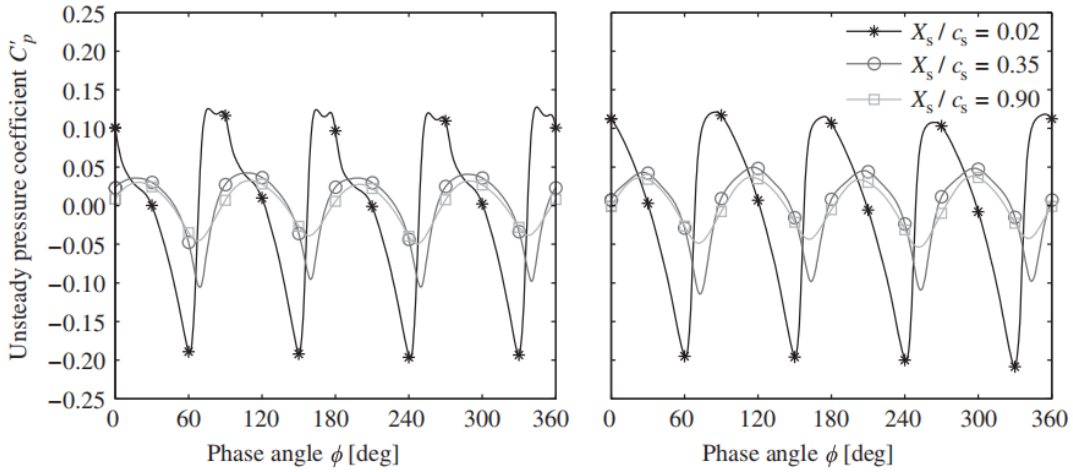

Figure 1.6: PLA at microphones located along the convecting tip vortex for (a) Advancing side, and (b) Retreating side **[20]**.

Structure-borne noise was previously investigated by S. Ljunggren et al. (1988) **[24]** using a four-bladed propeller. The power spectral density (PSD) results also showed the tip-vortex to be the dominant source with peaks at the blade passage frequency (BPF) and its harmonics. The harmonics obtained at the transducers placed farther away from the tip-vortex impingement regions showed lower PSD levels, hereby highlighting the dominance of the tip-vortex with respect to structure-borne noise. The PSD levels for transducers near the wing region where the tip-vortex impinges, and the transducers away from the tip-vortex impingement regions, are shown in Fig. 1.7 and Fig. 1.8.

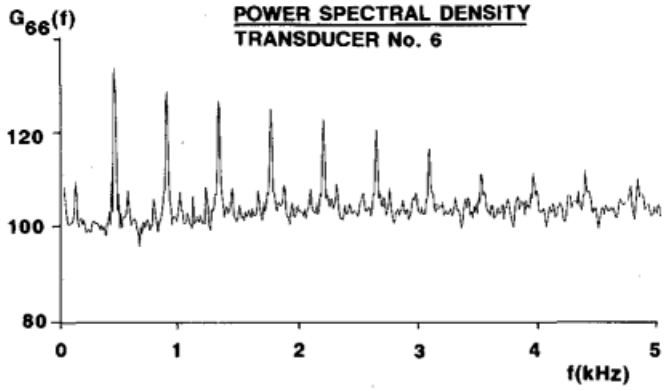

Figure 1.7: Power spectral density for transducer 6, near the region of tip-vortex impingement **[24]**.

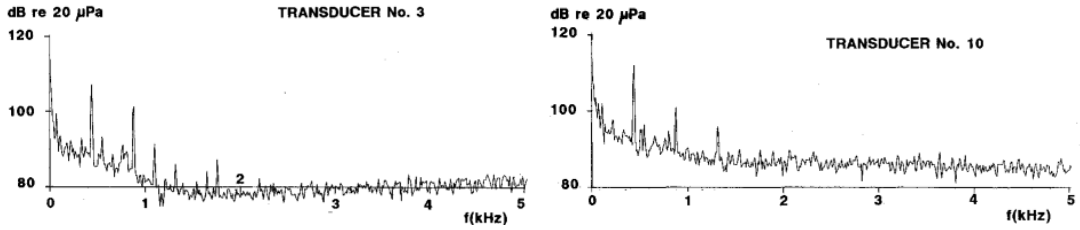

Figure 1.8: (a) Transducer 3. (b) Transducer 10. PSD for transducers 3 and 10 placed farther away from the tip-vortex impingement region [24].

While prior studies have successfully described the general physics of propeller-induced flow structures, they have relied predominantly on flow visualisation techniques (e.g., PIV, Schlieren) or flow field measurements away from the surface, with limited studies focusing on the unsteady surface pressure fluctuations. These methods provide valuable insight into vortex behaviour and wake dynamics, but do not directly quantify the unsteady surface pressure fluctuations experienced by downstream bodies. To bridge this gap, a novel flexible PCB-based measurement device embedded with microphones and pressure sensors is used to capture time-resolved surface pressure fluctuations across the airfoil under both positive and negative thrust regimes.

Moreover, recent studies on the negative thrust regimes for unducted propellers have been limited to isolated propellers or computational analyses involving the aeroacoustics of such propellers. Experimental investigations involving direct pressure measurements on downstream aerodynamic surfaces under negative thrust conditions remain limited. The current work also aims to bridge this gap.

Despite these limitations, it remains essential to examine the physical characteristics of the propeller slipstream under negative thrust conditions, particularly the flow behaviour at the propeller itself, as it directly influences the structure of the slipstream and its subsequent interaction with downstream surfaces. These aspects are discussed in the following section.

1.3 Propellers in Negative Thrust Regime

PIV measurements of the propeller slipstream under zero and non-zero thrust conditions, conducted by E. W. M. Roosenboom et al. (2012) [1] revealed distinct differences in flow behaviour. Under non-zero thrust, the slipstream becomes highly concentrated and well-defined due to the significant axial momentum imparted by the propeller blades. In contrast, the zero-thrust condition is dominated by rotation-induced swirl, resulting in a primarily tangential flow component with minimal axial acceleration. Notably, in the zero-thrust case, tip vortices were observed to lead the slipstream, whereas under thrust-producing conditions, these vortices energise the slipstream and play a major role in generating unsteady surface pressure fluctuations.

While these observations describe the behaviour in zero and positive thrust regimes, the slipstream characteristics change considerably under negative thrust conditions, which are relevant during descent, braking, or power regeneration. In such cases, the propeller operates against the incoming flow, resulting in different wake properties and tip vortex behaviour.

A propeller operates in negative thrust mode (or power-absorbing mode) during landing. In this mode, the propeller blades are adjusted to push air forward instead of rearward, generating a force that helps to decelerate the aircraft. This is particularly useful for safety and efficiency, as it shortens the landing distance and reduces the strain on the brakes. Beyond their application in landing and braking, propellers operating in the negative thrust regime can also function as regenerative propellers. This contributes to the goals of sustainable aviation by reducing noise emissions and energy consumption. Braking refers to the operating condition in which the propeller produces negative thrust. However, to operate in the regenerative or energy-harvesting[5] regime, the propeller must also generate negative torque. This is achieved by adjusting the blade α to negative values, which reorients the lift vector in the opposite direction. This is illustrated in Fig. 1.9 for the three regimes. This can also be achieved by increasing the J, which is done by decreasing the propeller RPM while maintaining a constant V_∞. The resulting high J condition leads to a negative α at the blade sections. This is the approach used in the current experimental campaign.

[5]These two terms will be used interchangeably in future references.

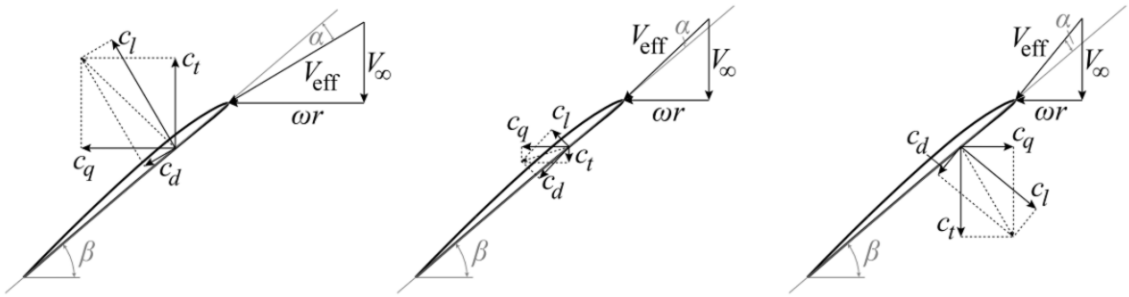

Figure 1.9: The velocity triangles corresponding to the airfoil section corresponding to the (a) propulsive (positive thrust) regime, (b) braking (negative thrust) regime, and (c) regenerative (negative thrust and torque) regime [25] [26].

However, before investigating the slipstream interactions related to power regeneration, it is crucial to first discuss the aerodynamic behaviour of the propeller in this regime. Operating in negative thrust places the propeller in an off-design condition, which gives rise to complex unsteady flow phenomena. These can degrade aerodynamic performance and may pose safety risks if not adequately quantified. Therefore, a detailed discussion of the propeller in this regime is essential.

J. Goyal et al. (2021) [27] investigated an isolated propeller test case at positive and negative thrust regimes at $0°\alpha$. An important rotational effect observed in Fig. 1.10 is the outward movement of separated flow along the blade span. When the flow begins to separate, centrifugal forces act on the fluid, causing it to be pushed radially outward along the rotating blade. This movement redirects the low-energy fluid near the root toward the tip. As a result, a Coriolis force is generated, which contributes to a favourable pressure gradient. This phenomenon contributes to the Himmelskamp effect, which helps delay the onset of stall. Improved stall characteristics, combined with the favourable pressure gradient, result in an increase in C_L values compared to non-rotating blades [27]. In Fig. 1.10, on the suction side near the TE, the flow pattern shows signs of the Himmelskamp effect, where separated or near-separated flow is displaced toward the outboard blade tips. This behaviour is more pronounced in the negative thrust regime due to the larger extent of stalled flow, hereby also affecting the slipstream. However, it is essential to note that this effect is not exclusive to the negative thrust condition.

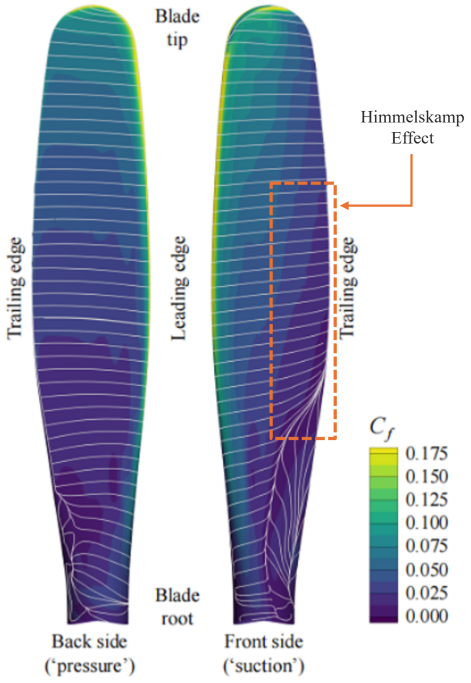

Figure 1.10: Adapted from [26]. Flow visualisation using C_f and shear lines (RANS) at $J = 0.8$ and $T_C = 0.09$.

The onset and extent of such flow separation and thrust generation are strongly influenced by the propeller blade's geometric and operational parameters, particularly the blade pitch angle (β) and the J. For a fixed value of J, a higher β is required to achieve peak propulsive efficiency. Conversely, at the same J, reducing β leads to a progressive decrease in thrust, eventually resulting in negative thrust. This occurs because variations in β directly alter the sectional α along the blade. Reducing the β results in a linear reduction in both the T_C and P_C until the propeller transitions into the energy-harvesting regime **[27]**. This is an important result, as in the current campaign, certain tests are performed at a fixed J with different values of β to achieve both positive and negative thrust. Additionally, due to the positive camber of propellers designed for the propulsive regime, a negative α is required to operate in the regenerative regime.

R. Nederlof et al. (2025) **[25]** investigated propellers operating at various β in both positive and negative thrust regimes. The C_T vs. J curves showed a noticeable horizontal shift towards higher J values as β increased. As illustrated in Fig. 1.11, at lower β, the negative lift vector aligns with the direction of negative thrust. This results in an extended braking regime over a broader range of J, as a more significant change in blade inflow angle is required to produce negative torque. In contrast, at higher β, the negative lift vector becomes aligned with the negative torque vector. As a result, a comparatively minor variation in J is sufficient to cause a transition from the braking regime to the regenerative regime. However, it is essential to note that highly cambered propellers, optimised for the propulsive regime, require larger negative α at the blade sections to operate in the regenerative regime. This often leads to flow separation over portions of the blade, thereby reducing energy-harvesting efficiency[6]. In contrast, operating at a lower blade β condition can lead to comparatively higher energy-harvesting efficiency at lower values of J. This is one of the key reasons why variable pitch propellers are preferred in most applications, as they allow for optimal performance across both propulsive and regenerative regimes by adjusting the blade pitch to match the desired operating condition.

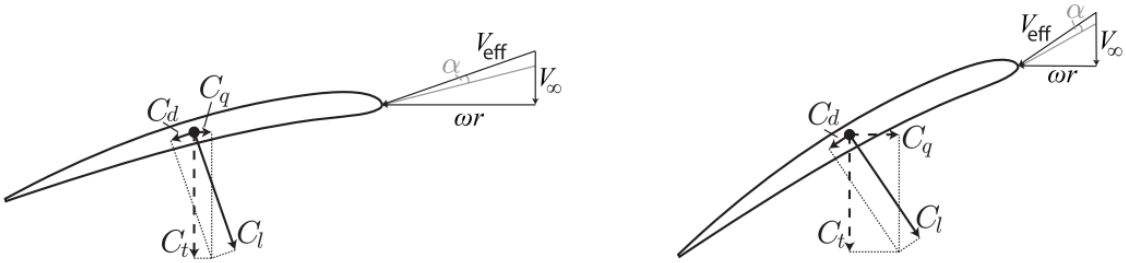

Figure 1.11: Velocity triangle and blade forces in the regenerative regime at equal α for (a) low β, low J, and (b) high β, high J **[25]**.

These variations in blade loading across different values of β and J conditions not only influence thrust and torque generation but also have a direct impact on the slipstream. Observations from studies on isolated propellers provide essential insights into these effects, as changes in blade loading modify the slipstream, which in turn governs the downstream interactions with surfaces such as wings or tails. For instance, an isolated propeller operating in the positive thrust regime typically exhibits higher outboard loading, resulting in stronger tonal noise characteristics near the blade tips. In contrast, under negative thrust conditions, the outboard loading is significantly reduced, leading to lower tonal noise levels in the same region. This reduction is attributed to the fact that the blade tips are not heavily loaded in the negative thrust regime and can also exhibit stall **[25]** **[26]**. The corresponding result, obtained from RANS data, is presented in Fig. 1.12. It is important to note that in an installed configuration, a downstream wing can induce upstream effects that modify the propeller loading. The magnitude of this effect depends on the axial distance between the propeller and the wing, with the sensitivity decreasing as the separation distance increases.

[6] Energy-harvesting efficiency refers to the fraction of available power (from negative torque) that can be extracted by the system. This is different from turbine efficiency, which is related to the extracted power based on the negative thrust. Therefore, in an extended braking regime, turbine efficiency can appear higher even if less power is actually extracted.

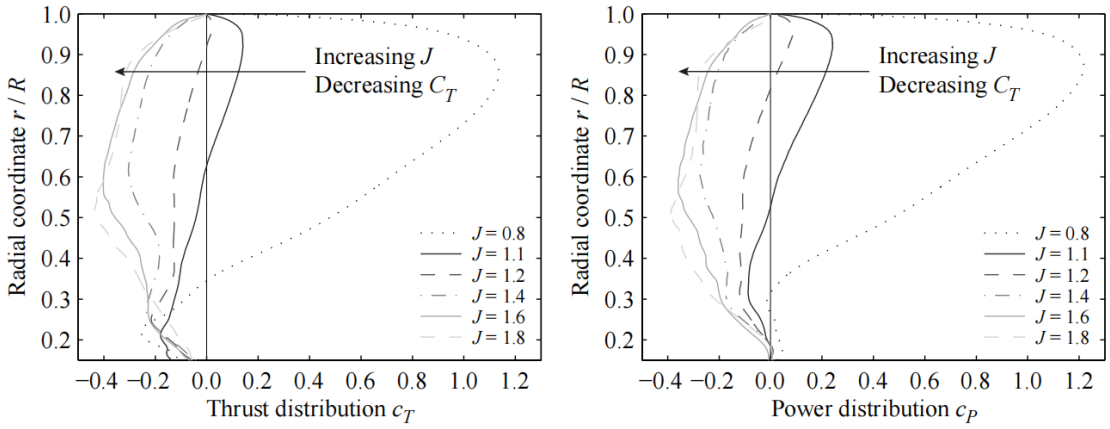

Figure 1.12: Distribution of blade loading in terms of thrust and power coefficients for the isolated propeller case (based on RANS simulations) **[26]**.

T. Sinnige et al. (2019) **[26]** conducted RANS and XROTOR-based simulations **[28]** on wing-tip mounted TP in the negative thrust regime. The results[7] for C_T and C_P, and T_C are shown in Fig. **1.13**. It can be observed that as the J increases, both the thrust and power coefficients decrease. However, negative values of C_P occur at higher J than negative C_T. This is because in the zero or slightly negative thrust regime (braking regime), the lift vector remains positive. As J increases further, the lift vector reverses direction, resulting in negative C_P values, marking the transition into the regenerative regime. This behaviour is illustrated in Fig. **1.9**. The findings illustrated in Fig. **1.13** are consistent with experimental results reported by R. Nederlof et al. (2025) **[25]**. However, it is essential to note that, in the study by T. Sinnige et al. (2019) **[26]**, the propeller was neither designed nor optimised for operation in the negative thrust regime. As a result, when operated under off-design conditions, a significant portion of the blades is susceptible to stall, resulting in reduced energy harvesting efficiency. This limitation not only affects the propeller's isolated performance but also influences the downstream aerodynamic interactions with the wing. For a more representative understanding of regenerative effects, future investigations would benefit from comparing cases with higher energy-harvesting efficiency, rather than contrasting mismatched operating conditions[8].

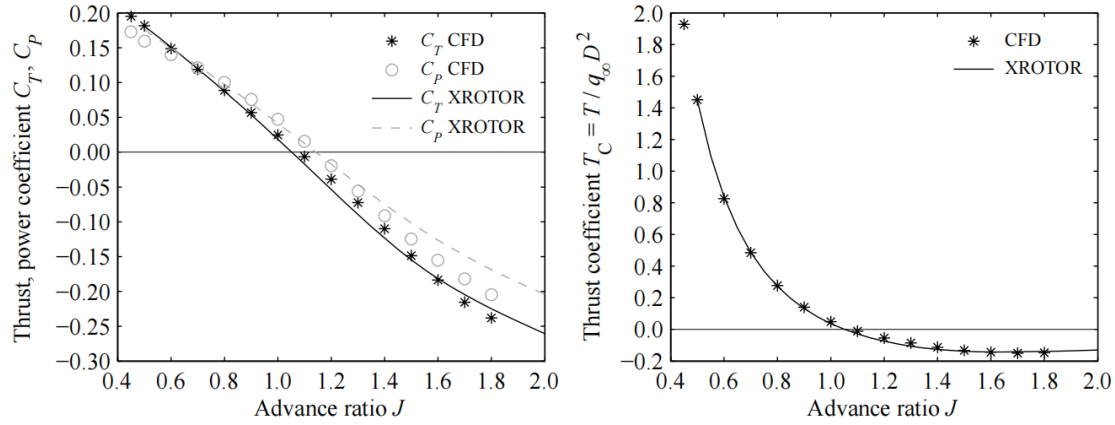

Figure 1.13: Coefficients of power and thrust versus advance ratio for an isolated propeller (RANS and XROTOR) **[26]**.

Understanding the aforementioned performance trends is essential, as changes in propeller operating conditions, particularly in the regenerative regime, alter the velocity field experienced by downstream aerodynamic surfaces, such as the airfoil model used in the current campaign. Experimental data from the TUD XPROP-3 ($15°\beta$) **[29]**

[7] C_T and C_P are used for the isolated propeller case and are referenced to the rotational speed n, while T_C is used for installed configurations and is referenced to the freestream dynamic pressure q_∞.

[8] The design and fabrication of a propeller optimised specifically for efficient operation in the negative thrust regime was considered beyond the scope of the current study.

is shown in Fig. 1.14 and it illustrates this behaviour. A reversal in the direction of swirl for the regenerative case is observed as compared to the propulsive case. This is due to the negative torque vector.

This swirl reversal has detrimental effects on downstream bodies, along with the reduced dynamic pressure (q_∞) in the negative thrust regime. The q_∞ is expected to be reduced within the slipstream as compared to regions outside it, resulting in lower lift generation. Additionally, the trends at the retreating and advancing blades are now reversed due to the reversal of swirl. The beneficial swirl effect is typically observed on the retreating blade side in propulsive operation. However, in the regenerative regime, this benefit shifts to the advancing blade side, while the retreating side is plagued by reduced local V_{eff} and local α effects. Furthermore, the intensity of the resulting tip vortex is influenced by the distance between the downstream wing and the upstream propeller.

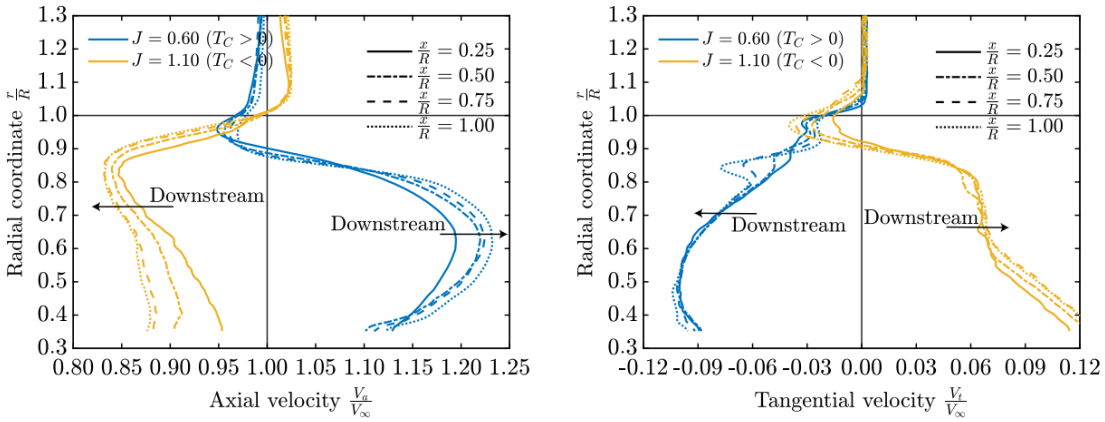

Figure 1.14: Radial distribution of axial and tangential velocity [25].

In the present study, the airfoil model is placed at one propeller diameter distance downstream to isolate the effect of the propeller-induced flow on a downstream airfoil surface. Significant unsteady loading is observed due to interactions with the slipstream vortex structures. This occurs in both the power-output and power-absorbing conditions. This is because thrust is generated at the wing even at $0°\alpha$. This occurs when the Kutta–Joukowski force tilts forward due to the combined effect of axial and swirl components in the V_{eff}. As noted by R. T. Johnston and J. P. Sullivan (1993) [18], the sectional lift per unit span (L') can increase or decrease depending on whether the blade segment is in the retreating or advancing phase.

During the power-absorbing (negative thrust) phase, the propeller tip vortex approaches the wing LE and undergoes visible deformation, particularly on the rotation-up side, as studied by [18][4]. This resembles an image vortex effect — a phenomenon that occurs when a vortex filament nears a solid boundary, inducing a mirrored vortex to satisfy the no-penetration/impermeability condition at the surface. To satisfy this boundary condition, an image vortex is mathematically induced on the opposite side of the boundary, mirroring the real vortex's strength and direction. This ensures that the boundary conditions are met by the resulting flow field. Physically, the real vortex is "pushed" due to the induced velocity created by the vortex filament. This causes the deformation based on the flow conditions. Another plausible reason for the spanwise shear is the spanwise circulation effect of the wing. Eventually, the severed vortex filament attempts to reconnect at the TE.

Despite these insights into vortex behaviour under negative thrust conditions and the distinct differences observed in blade loading and slipstream characteristics, studies that examine the unsteady interaction of the slipstream with a downstream body in this regime remain limited. Furthermore, a majority of these studies concern unsteady force measurements, with a notable lack of research on surface pressure fluctuations on lifting bodies immersed in the slipstream under negative thrust conditions. The present study addresses this gap by employing a flexible PCB-based measurement device equipped with embedded microphones and pressure sensors to quantify unsteady surface pressure fluctuations across the airfoil under both positive and negative thrust conditions. Furthermore, the study is conducted on two different α values to account for the change in aerodynamic loading of the airfoil and its subsequent effects.

1.4 Gaps and Motivation

Propeller–wing interactions have been extensively studied in the conventional propulsive regime, with a focus on wake impingement effects, noise characteristics, and unsteady velocity fluctuations. However, with the growing interest in regenerative operations and hybrid propulsion systems, it becomes increasingly important to understand the nature and the effects of these interactions in negative thrust conditions.

While time-averaged studies in the negative thrust regime exist, there is a lack of experimental work involving the quantification of unsteady surface pressure fluctuations on downstream bodies, as most of these studies focus on unsteady force measurements. Key phenomena, such as the effects of swirl reversal on surface pressure fluctuations and tip vortex impingement and convection on downstream bodies, are not well documented.

Furthermore, within the scope of PP configuration studies, most research has primarily focused on the upstream effects, particularly the influence on the wing BL. In contrast, investigations into the downstream effects remain comparatively limited. This may partly be due to the relative rarity of modern aircraft configurations where a PP operates near a downstream horizontal tail, such as in Cessna Skymaster models, making it less common as a subject for aerodynamic analysis. In the current study, a distance of one Dia_{prop} is maintained between the propeller and the airfoil to isolate the interaction effects on the wing, while minimising upstream influence on the propeller loading induced by the airfoil.

Moreover, operating in the negative thrust regime places the propeller in an off-design condition, which can lead to safety concerns and degraded aerodynamic performance. Therefore, a detailed aerodynamic investigation is essential, not only to understand the associated unsteady flow effects but also for designing quieter and more efficient propellers. Such propellers should be capable of achieving high energy-harvesting efficiency during regenerative operation without compromising propulsive efficiency during normal operations. Hence, a study into the effects observed in the negative thrust regime is essential.

An additional key objective of the current study is the validation of a novel measurement device: a flexible PCB embedded with microphones and pressure sensors. This off-the-shelf product offers significant potential and is financially and experimentally advantageous. Initially developed for in-flight testing on the Cessna Skymaster N4207X flying testbed, wind tunnel tests at low Re will extend its utility while verifying its fidelity and reliability.

1.5 Research Aim and Objectives

To address the gaps identified in the previous sections, specifically, the limited research on downstream effects in PP configurations, limited experiments on unsteady surface pressure fluctuations on bodies immersed in a propeller slipstream in the negative thrust regime, along with the validation of the novel measurement device, this study formulates two primary research questions:

1. How can the novel measurement device be experimentally validated, and how effectively can it quantify unsteady surface pressure fluctuations on a downstream wing under the influence of a propeller wake?
2. How do unsteady pressure fluctuations vary across the surface of a downstream wing[9] in a pusher-propeller configuration under positive and negative thrust conditions?

To address the first question, the microphones and pressure sensors on the device will first be validated. Following this, wind tunnel experiments will be conducted on an airfoil model immersed in the slipstream of an upstream pusher propeller. The data will be validated through comparison against known baseline conditions at low Re (e.g., nacelle-only cases). Additionally, the reliability of the device will also be assessed by comparing key trends in pressure fluctuation metrics (e.g., p_{rms}, Cp', spectral content) with existing literature. This will demonstrate the capability of the device to resolve unsteady surface pressure fluctuations with sufficient fidelity.

To address the second question, the experiments will be extended to multiple test conditions, covering both positive and negative thrust regimes. The device will be used to measure data from the microphones and pressure sensors at various spanwise positions on both suction and pressure sides of the airfoil. By comparing the spatial distribution and amplitudes of the pressure fluctuations, insights into the impact of different thrust conditions will be obtained. The pusher-propeller configuration is selected to ensure that the propeller slipstream impinges on the downstream airfoil model without being influenced by upstream disturbances, such as interactions with the

[9] An airfoil model is used in the current study.

nacelle or support sting. In contrast, a tractor configuration would cause the slipstream to first interact with the nacelle and sting before reaching the airfoil, introducing additional flow distortions. Additionally, positioning the airfoil at a distance of one propeller diameter downstream of the propeller minimises aerodynamic coupling between the airfoil and the propeller. This reduces upstream influence from the airfoil on the propeller loading, which could otherwise alter the slipstream characteristics and, in turn, affect the surface pressure fluctuations measured on the airfoil. Maintaining this separation ensures that the measured fluctuations are primarily due to the imposed slipstream, rather than feedback effects from changes in propeller loading.

1.6 Thesis Outline

The thesis is divided into two major parts: Experiment I and Experiment II, with Chapter 2 serving as the common methodology chapter for both experiments. The complete structure of the thesis, consisting of six chapters, is illustrated in Fig. 1.15.

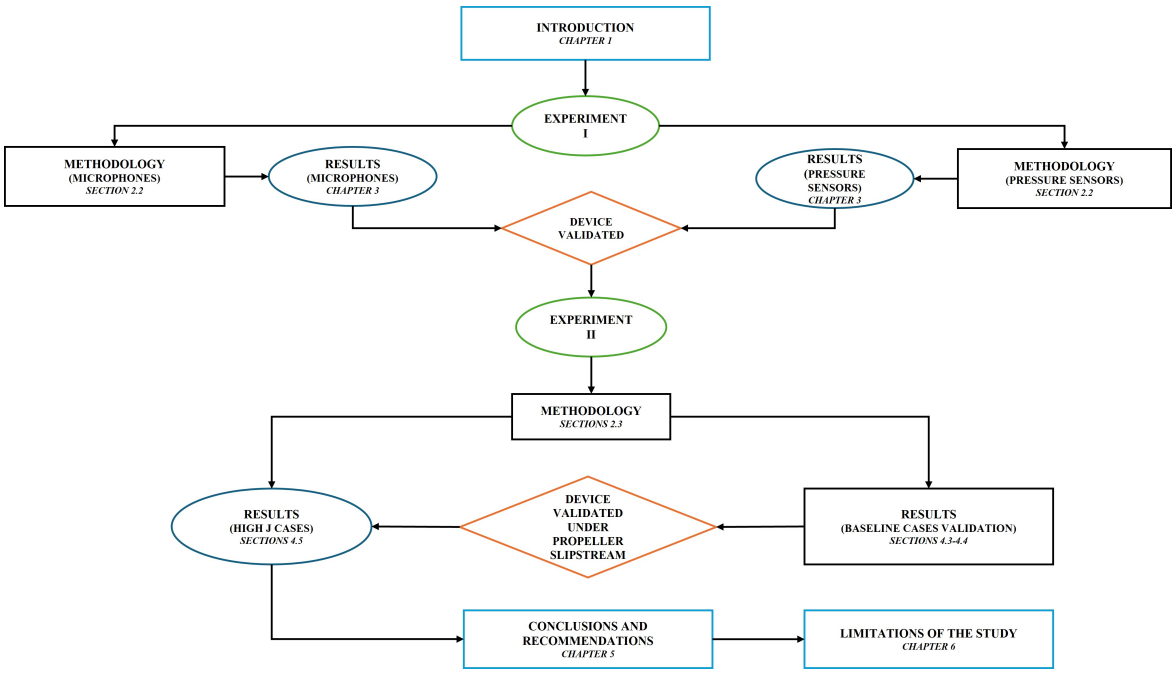

Figure 1.15: Thesis Outline.

The study begins with Chapter 1, which introduces the research context, objectives, and background literature. Experiment I involves validating the device microphones and pressure sensors. The methodology for these measurements is described in Section 2.2, while the corresponding results are presented in Chapter 3. Upon successful validation, the device is deemed suitable for further investigations.

Following this, Experiment II focuses on characterising the unsteady surface pressure fluctuations on an airfoil immersed in the propeller slipstream. The methodology specific to this phase is detailed in Section 2.3, and the corresponding results are presented in Sections 4.3–4.5 of Chapter 4. The baseline cases, including the nacelle-only configuration and low J conditions discussed in Sections 4.3 and 4.4, serve to validate the data measured by the device in the propeller slipstream. Once validation under the propeller slipstream is successful, analysis proceeds to the measurements for high J cases in Section 4.5.

The concluding discussion and interpretation of the key findings are presented in Chapter 5, while Chapter 6 outlines the study's limitations.

2

Methodology

This chapter outlines the methodology followed during the experimental campaign. **Section 2.1** aims to describe the measurement device and the components. **Section 2.2** provides an overview of the test cases, describes the wind tunnel facility and associated blockage correction, and outlines the experimental setup used to validate the device. **Section 2.3** proceeds with the nomenclature of the test cases conducted during the second experiment, followed by a description of the wind tunnel facility and the motivation for applying the required boundary corrections. It concludes with an overview of the experimental setup used to quantify propeller wake–wing interactions, along with the data processing methods.

2.1 The Measurement Device: Sensor-Embedded Flexible PCB

This section provides an overview of the novel measurement device, a flexible PCB embedded with microphones and pressure sensors. It was initially developed to investigate propeller-wing interactions using the Cessna Skymaster N4207X flying testbed. It is a flexible PCB embedded with 54 microphones and 18 pressure sensors. A prototype of this device is used in the current campaign for wind tunnel tests at low Re. Henceforth, further references to this prototype used in this campaign will just be referred to as the device. The subsequent paragraphs will provide a detailed description of the device's design and components.

The device is equipped with 18 microphones and 6 pressure sensors, with dimensions 350 x 150 mm. The pressure sensors are Bosch BMP390 absolute pressure sensors with a range of 300-1250 hPa and an absolute and relative accuracy of $\pm$ 50 Pa and $\pm$ 3 Pa, respectively. The dimensions of these sensors are 2 x 2 x 0.75 mm. More details on the specifications can be found in BMP390's data sheet **[30]**. The device is equipped with 18 Knowles SPW0690LM4H-1 microphones **[31]**. The entire device is not flexible since sensors require a rigid base. A fully flexible base can cause sensor detachment. The rigid part is 0.6 mm thick. The flexible part is Kapton-based and is designed to wrap around the LE of an airfoil. However, due to limitations in flexibility and the fixed arrangement of the sensors, repositioning the device to multiple streamwise positions is challenging. It is connected to an FPGA, which can be connected to a DAQ hardware via an Ethernet cable. Additionally, the FPGA is equipped to receive an encoder signal via a BNC port on channel Sync54. This encoder signal is provided by the propeller motor control system in the form of a square wave based on each propeller rotation through a dedicated BNC connection. The sampling frequency is 1.11 MHz. Further technical details regarding the components' design and operation can be found in Dutch Patent NL 2036392 B1 **[32]**. The device and the components are shown in Fig. **2.1**.

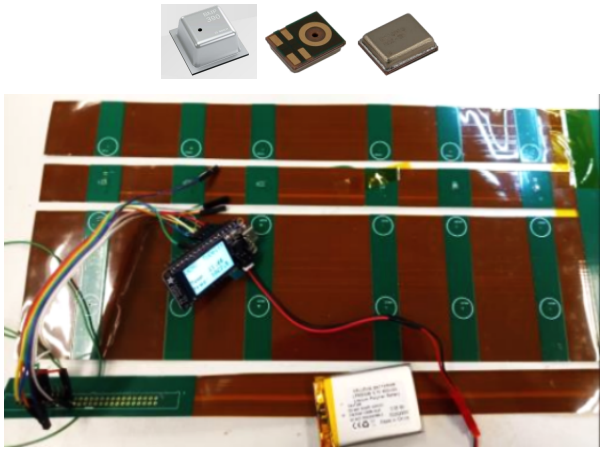

Figure 2.1: The device and its components: (a) BMP390 Pressure sensor and Knowles SPW0690LM4H-1 Microphone, (b) the device.

2.2 Validation of the Device: The First Experiment

This section provides detailed insights into the initial phase of the campaign, which aims to validate the novel measurement device. This is an important step, as validating the device is crucial to ensure it can be used in further experiments. The subsequent sections will provide an overview of the test cases and describe the experimental setup for the validation test cases.

2.2.1 Overview of the Test Cases

The validation test cases are described below:

- Microphone validation-
  - CASE A - A tone of known frequency is played over the microphones to check the response. This is a preliminary test performed outside the wind tunnel test section. Following this test, the microphones are calibrated.
  - CASE B - The device is wrapped around a NACA $63_3 - 018$ airfoil model with a cylinder (Ø19.05 mm) placed at a distance of 267 mm upstream. This test is performed in the wind tunnel test section at different velocities.
- Pressure sensor validation- The device is wrapped around the NACA $63_3 - 018$ airfoil, and the test is performed in the wind tunnel test section at different velocities. The data is compared with data obtained from the Pressure Transducers and XFOIL **[33]**.

2.2.2 Wind Tunnel Facility

The experiment is conducted in the M-Tunnel, located in the Low-Speed Wind Tunnel Laboratory of Delft University of Technology, the Netherlands. This wind tunnel is a model tunnel with the capability of being used as an open-jet or a closed wind tunnel. It is a low-turbulence tunnel with a test section measuring 400 mm x 400 mm, and a maximum velocity of 35 m/s and 50 m/s for the open and closed configurations, respectively **[34]**. The current experiment is conducted in an open-jet configuration. The M-tunnel and the M-Tunnel test section are shown in Fig. 2.2.

The desired freestream velocity (V_∞) is achieved by adjusting the fan RPM through the M-Tunnel control interface windows. Both interface windows can be referred to from Appendix Fig. A.1.

Figure 2.2: (a) M-Tunnel, (b) M-Tunnel test section.

2.2.3 Blockage Correction

The walls of the wind tunnel serve as physical constraints that affect and alter the flowfield around the test model. Therefore, corrections are required to ensure that the flowfield around the model is as close as possible to the freestream flow. However, achieving an exact match with freestream conditions remains challenging due to the inherent limitations of the test environment.

A test model, an airfoil in the current study, placed inside a test section, constricts the tunnel inflow and induces an increase in the local flow velocity over the test model. This alters the flow in comparison to the freestream, depending on the model's size relative to the tunnel size, as well as its placement within the tunnel. Therefore, it is essential to account for this flow modification and implement corrective measures for the measured quantities. This effect is called the "solid blockage". The solid blockage of the airfoil is estimated using methods described by J. G. Herriot (1947) **[35]**. J. G. Herriot states, "Any wing profile can be represented by a suitable distribution of sources and sinks along the chord. It follows that the total induced velocity due to the wing images is obtained by summing over this distribution" **[35]**. The solid blockage corrections necessary to account for the flow modification caused by the test model are performed in this study.

The solid blockage for the airfoil (considered as a three-dimensional wing) is given by Eq. 2.1. κ_1 is the body shape factor that depends on the shape of the base profile, while τ_1 is the tunnel/model factor that depends on the tunnel shape and wing-span-to-tunnel-breadth-ratio **[35]**. In the current study, a NACA $63_3 - 018$ airfoil is used, resulting in a t/c ratio of 0.18. t/c is important to estimate the κ_1. V_{model} refers to the volume of the model and C refers to the tunnel cross-sectional area.

$$\epsilon_{sb,w} = \frac{\kappa_1 \tau_1 V_{model}}{C^{\frac{3}{2}}} \tag{2.1}$$

The values of κ_1 and τ_1 can be found from the historical database. The respective tables are shown in Fig. A.20 and Fig. A.21 in Appendix A.8. The values of these constants are: $\kappa_1 = 1.047$, $\tau_1 = 0.916$, $V_{model} = 0.00179\ m^3$ and $C = 0.16\ m^2$. Hence from Eq. 2.1 $\epsilon_{sb,w} = 0.02682$. These corrections[1] are then applied to q_∞ and V_∞ as per Eq. 2.2 and Eq. 2.3,

$$q_\infty = q_{uncorrected}(1 + \epsilon_{sb,w})^2 \tag{2.2}$$

$$V_\infty = V_{uncorrected}(1 + \epsilon_{sb,w}) \tag{2.3}$$

Since the current setup does not include a force balance, corrections related to aerodynamic forces and the α[2] are omitted.

[1] Given the relatively small influence of blockage effects on the local flow velocity for the present configurations, the corrected velocity has not been used.

[2] Corrections concerning the α are a function of the aerodynamic forces.

2.2.4 Experimental Setup and Test Model

The airfoil used in this campaign is a 200 mm-chord NACA $63_3 - 018$. The span is 400 mm with two available 200 mm span extensions. It is a symmetric airfoil with $t/c = 0.18$ at x = -0.661c with t_{TE} = 0.00075c. This was manufactured at Delft University of Technology as an assembly of three solid modular aluminium structures [36]. The airfoil profile annotated with the location of the zigzag trip and the axis orientations is shown in Fig. 2.3.

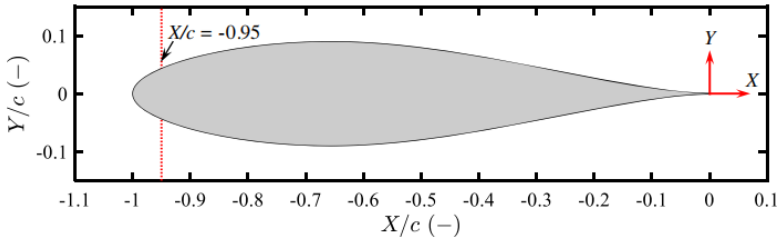

Figure 2.3: NACA $63_3 - 018$ airfoil with axis reference from the TE [36][37].

The airfoil is modular and equipped with a removable TE. As shown in Fig. 2.3, the model is tripped using a zigzag tape placed at -0.95c from the TE on both the upper and lower surfaces. The model is made of aluminium and has a total of 27 pressure taps distributed chord-wise on both surfaces. More details on the distribution of the pressure taps can be found in [36]. The data from these pressure taps will be used to validate the pressure data obtained from the device. The different parts of the model are shown in Fig. 2.4.

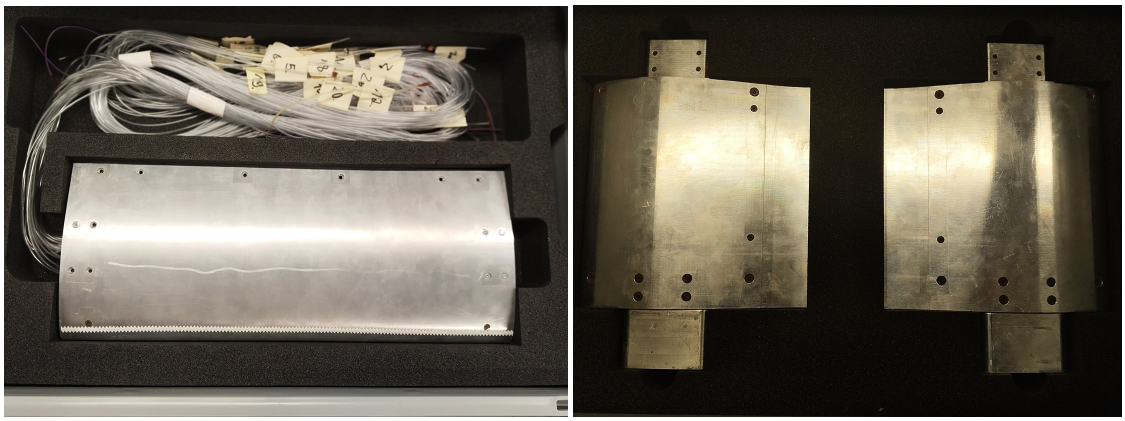

Figure 2.4: (a) Airfoil model without the removable TE, (b) Extendable span parts.

Before proceeding with the test cases, it is essential to understand the layout of the microphones and pressure sensors on the device. Furthermore, a coordinate system specific to each test case is crucial to avoid ambiguity and confusion. The layout of the microphones and pressure sensors on the device remains fixed and is not subject to change throughout this campaign. However, the coordinates of different microphones and pressure sensors vary depending on the test case. Two different configurations are shown in Fig. 2.5: the full layout of the device and its configuration when wrapped around the airfoil.

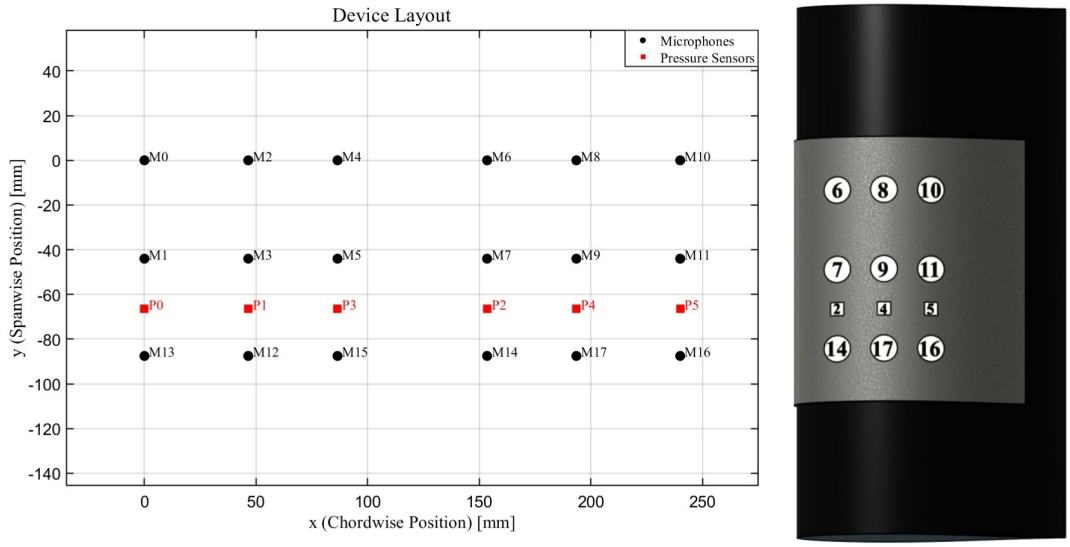

Figure 2.5: (a) Full layout of the device, (b) Illustration of the layout of the device when wrapped around the LE of the airfoil model (suction side view). The illustration is not to scale; sensor dimensions and coordinates are exaggerated for clarity. However, the relative ordering and arrangement of the microphones and pressure sensors accurately reflect the physical configuration. Circles represent the microphones and squares represent the pressure sensors, with their respective channel numbers annotated.

CASE A: Known Tone Excitation

To test the microphones of the device, the device is placed outside the wind tunnel, and a tone with a known frequency is played near the first row of microphones, namely Mic 0, Mic 1 and Mic 13 (the microphone channels are annotated from 0 to 17) from a smartphone. This is a preliminary test to verify that the response from the microphones is within acceptable limits, allowing for further validation and calibration of the microphone. The microphones are calibrated using a GRAS pistonphone at a frequency of 1 kHz and an SPL of 114 dB.

The layout and coordinates[3] of the microphones and pressure sensors are shown in Fig. 2.5.

CASE B: Vortex Shedding Response from Upstream Cylinder

The device is wrapped around the model, and tests are conducted at different wind tunnel speeds. A cylinder (Ø19.05 mm) is placed 267 mm upstream of the model. The goal of this configuration is to investigate the vortex shedding effect induced on the wing by the upstream cylinder. The test is conducted at multiple different inflow velocities. The shedding frequency obtained from this test plays a key role in verifying the Strouhal number (St) associated with flow past a circular cylinder. An illustration depicting the layout of the device when wrapped around the LE of the model is shown in Fig. 2.5. The results will be discussed in further sections.

Since the model is made of aluminium, it had to be masked with black tape to ensure that there is no electrical interference between the model and the device once it is wrapped around it. The setup is shown in Fig. 2.6.

[3]The coordinates will change based on the reference system, particularly when wrapped around the airfoil. This coordinate system is specific to this experiment. The layout of the device, however, remains constant.

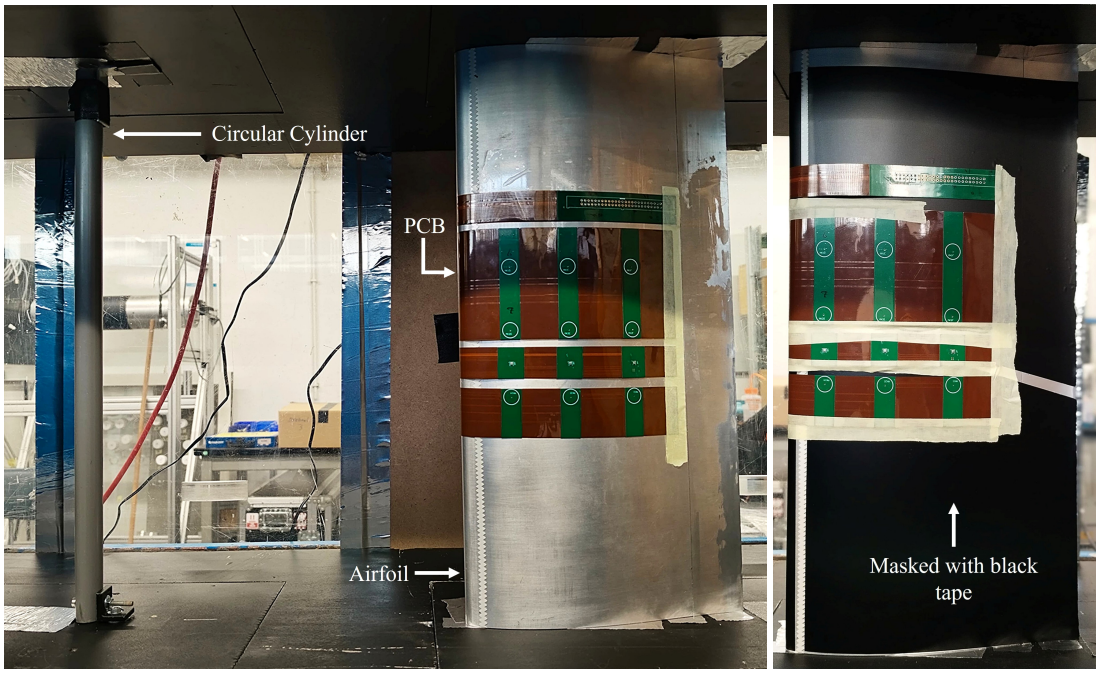

Figure 2.6: (a) CASE B setup, (b) CASE B masked model.

Data from the Pressure Taps

To validate the data from the pressure sensors, it must be compared with data from conventional measurements. Hence, the data obtained from the device pressure sensors is compared with the data obtained from the pressure scanner. There are 15 pressure taps on the suction side and 12 on the pressure side **[36]**. Although the airfoil is inherently symmetric, the side with more taps is designated as the suction side.

The pressure taps from the airfoil are connected to two separate modules- $\pm$ 600 Pa and $\pm$ 10 in H_2O (2490.889 Pa), each with a designated calibration $.csv$ file that can be accessed via the DAQ interface. These modules convert the physical air pressure into corresponding electrical voltages. The outputs are then fed into the DAQ system, which digitises the signals and transmits them to the PC for acquisition and processing. The final output is pressure, expressed in pascals (Pa). Both high-speed data and averaged data are stored.

The pressure taps are connected to the input ports on the modules. Meanwhile, another set of input ports is left unconnected, allowing the module to reference ambient atmospheric pressure. As a result, the modules effectively measure differential pressure, which is the difference between the local surface pressure and the ambient atmospheric pressure.

Tests are carried out at various wind tunnel speeds of 5 m/s, 10 m/s, 15 m/s, and 20 m/s, and at a non-zero α. The C_p-Distribution is plotted for all cases. The C_p is calculated according to Eq. 2.4, where p is the pressure measured at the airfoil surface via the surface pressure taps, p_∞ is the ambient pressure and q_∞ is the dynamic pressure. The C_P-Distribution is compared with XFOIL results at similar flow conditions (tripped at $0.05c$ from LE) to check if the data is within acceptable limits for validating the device pressure sensor measurements.

$$C_p = \frac{p - p_\infty}{q_\infty} \tag{2.4}$$

During these pressure measurements, the airfoil is not masked using the black tape, as the black tape renders the LE trip ineffective due to a thicker surface that interrupts the intended boundary layer transition[4].

[4] A similar effect is observed when the device is wrapped around the airfoil during the microphone validation tests.

2.3 Propeller Wake-Wing Interactions: The Second Experiment

The aim of the second phase of this campaign is to use the device to quantify propeller wake–wing interactions. Although the device has already been validated, it remains crucial to verify whether it produces measurements consistent with those reported in the literature under comparable flow conditions of a propeller slipstream. It is wrapped over the LE of the NACA 63_3-018 airfoil model with the model placed downstream of a propeller. The propeller is mounted upstream using a sting in a pusher configuration. The resulting unsteady surface pressure fluctuations on the airfoil, induced by the propeller slipstream, are analysed. The following sections describe the test cases and the experimental setup associated with the second experimental campaign.

2.3.1 Overview of the Test Cases

The tests carried out during this campaign are mentioned below [5].

- CASE01 ($0.8J$[6], $30°\beta$, $6N_B$[7] and $6°\alpha$) | Counter-clockwise propeller rotation
- CASE02[8] ($1.8J$, $30°\beta$, $6N_B$ and $6°$ α) | Counter-clockwise propeller rotation
- CASE03 ($1.8J$, $45°\beta$, $6N_B$ and $6°\alpha$) | Counter-clockwise propeller rotation
- CASE04 (Nacelle ONLY, $6°\alpha$)
- CASE05 ($1.8J$, $53°\beta$, $3N_B$ and $6°\alpha$) | Clockwise propeller rotation
- CASE06 ($0.8J$, $30°\beta$, $6N_B$ and $0°\alpha$) | Counter-clockwise propeller rotation
- CASE07 ($1.8J$, $30°\beta$, $6N_B$ and $0°\alpha$) | Counter-clockwise propeller rotation
- CASE08 ($1.8J$, $45°\beta$, $6N_B$ and $0°\alpha$) | Counter-clockwise propeller rotation
- CASE09 (Nacelle ONLY, $0°\alpha$)
- CASE10 ($1.8J$, $53°\beta$, $3N_B$ and $0°\alpha$) | Clockwise propeller rotation
- CASE11 ($0.8J$, $30°\beta$, $6N_B$ and $9°\alpha$) | Counter-clockwise propeller rotation
- CASE12 (Nacelle ONLY, $9°\alpha$)

Furthermore, the analysis has been divided into three parts:

1. CASE09 and CASE04: Comparing characteristics of the LSB at different α.
2. CASE06: Validation against known trends from literature.
3. Positive and Negative Thrust cases: Comparisons between positive and negative thrust cases at the same J. Test cases at higher J are selected based on performance curves, corresponding to operating conditions associated with peak efficiency (η) in respective positive and negative thrust regimes. Notably, the peak efficiency for both regimes occurs at the same advance ratio of $J = 1.8$, and at an absolute value of thrust coefficient $|C_T| \approx 0.25$ as shown in Fig. A.5.

2.3.2 Wind Tunnel Facility

The second experiment of this campaign is carried out in the Small Low-Turbulence Tunnel (SLT) located in the Low Speed Wind Tunnel Laboratory of Delft University of Technology, Netherlands. It is a low-turbulence tunnel with a test section of 600 x 900 x 1800 mm. The tests are carried out at a constant wind tunnel velocity of 20 m/s. The test section of the SLT, with the propeller rig and the airfoil model installed, is shown in Fig. 2.7.

[5] Several device test cases were conducted during the campaign. This report presents only cases that are relevant to the objective of the study and have reliable data. However, all cases are listed (including discarded ones) to maintain continuity in serial numbering and avoid ambiguity or confusion.

[6] For the present campaign, test cases corresponding to $J = 0.8$ are referred to as low advance ratio cases, while those with $J = 1.8$ are referred to as high advance ratio cases.

[7] All test cases discussed in this report were conducted using propellers with 6 blades (N_B = 6). Therefore, this specification is omitted from further case descriptions for brevity.

[8] CASE02 and CASE07 correspond to negative thrust cases.

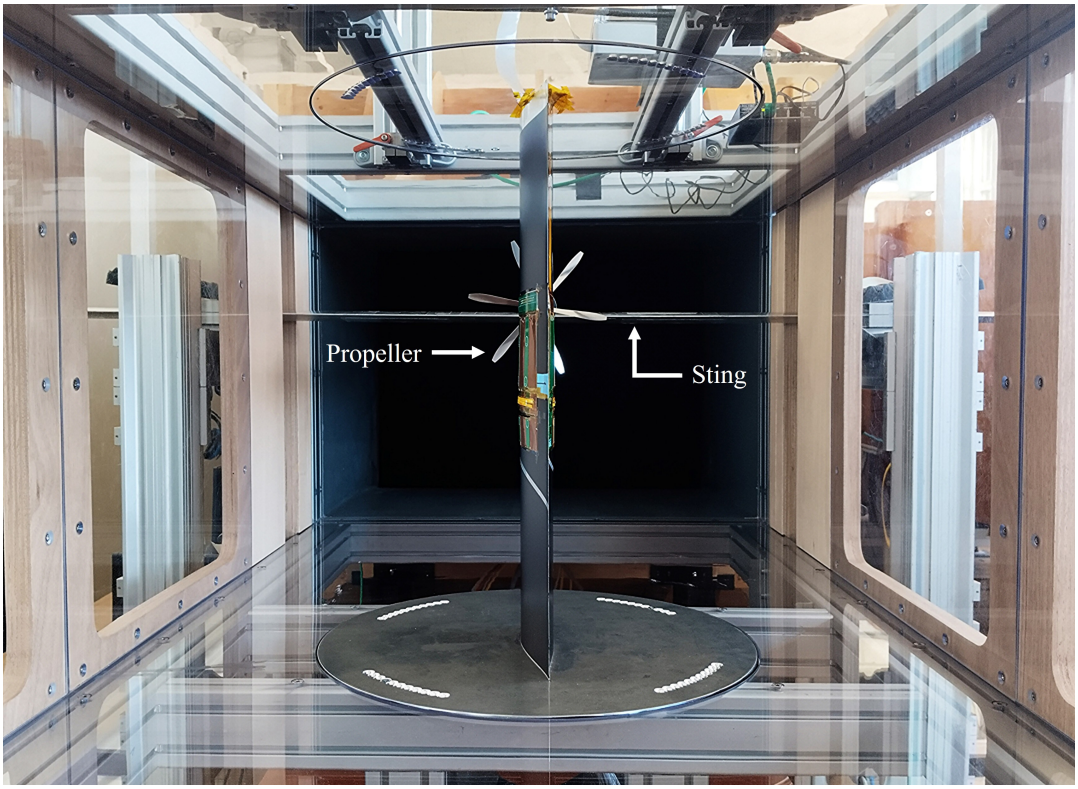

Figure 2.7: SLT test section.

The desired freestream velocity is achieved by adjusting the fan RPM through the SLT-Tunnel control interface. This is similar to the interface used in the M-Tunnel, and is shown in the Appendix Fig. A.2.

2.3.3 Blockage Correction

As discussed earlier in Section 2.2.3, the physical limits of the wind tunnel induce changes in the flowfield around the airfoil model and these changes hinder the exact representation of the freestream condition for the airfoil model [35]. One such effect is the solid blockage that occurs due to the presence of the airfoil. This is calculated using the method discussed in Section 2.2.3.

The corrections[9] are then applied to q_∞ as per Eq. 2.2 with an addition of ϵ_{sting}.

The propeller slipstream also induces changes in the flowfield that need to be accounted for and corrected. These changes are caused due to the additional momentum in the flow. This leads to an inverse blockage effect. Specifically, the velocity increases within the propeller slipstream and decreases outside of it. This reduction in velocity outside the slipstream is influenced by the presence of tunnel walls and does not accurately represent freestream conditions. Consequently, the thrust measured in the tunnel corresponds to a lower freestream velocity than in an unbounded domain. Hence, a correction is required. However, in the present study, this correction is not applied due to the unavailability of a load cell, which prevents direct estimation of the thrust coefficient (T_C). Similarly, correction pertaining to the α[10] is also omitted.

[9] Given the relatively small influence of blockage effects on the local flow velocity for the present configuration, the velocity correction has been omitted.

[10] Corrections concerning the α are a function of the aerodynamic forces.

2.3.4 Experimental Setup and Test Models

The tests are performed at a constant flow wind tunnel velocity of 20 m/s and at two airfoil α- 0° and 6°. To operate at different values of J, the propeller's rotational speed is adjusted accordingly using the motor control interface (see Fig. A.3). This rotational speed is measured using a feedback signal from an encoder mounted on the propeller shaft. The data acquisition interface used for motor control is shown in Fig. A.3. To facilitate variation in airfoil α, the wind tunnel test section is required to be modified accordingly. The airfoil is mounted vertically, and its α is adjusted using rotatable sideplates integrated into the top and bottom walls of the test section. The propeller rig is positioned upstream of the airfoil and integrated into the test section using x-beams. The support sting is clamped horizontally and can be installed across multiple positions in the vertical direction. This enables sampling of data at different spanwise positions of the vertically placed airfoil model. The relative configuration of the propeller rig and airfoil model is illustrated in Fig. 2.8 along with the technical drawings of the propeller-nacelle assembly and the sideplate. Further details on the propeller rig can be referred to from [38].

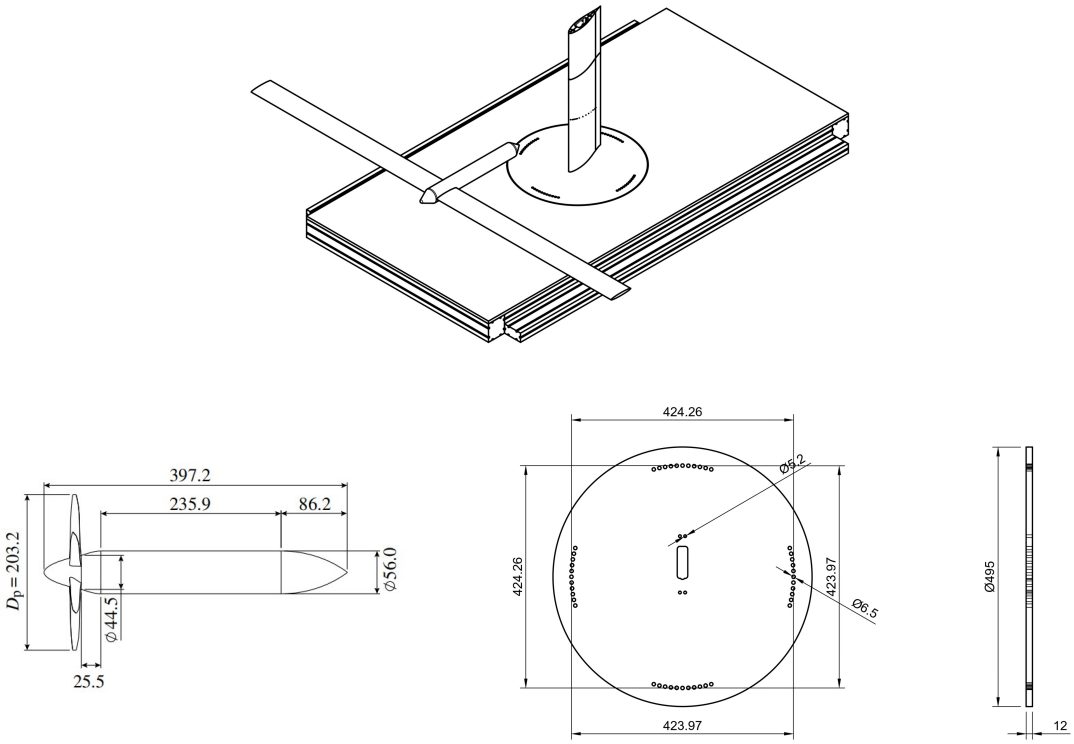

Figure 2.8: (a) Isometric view (nacelle-only configuration) of the propeller rig and downstream airfoil model. Other components of the test section are omitted for clarity. (b) Technical drawing of the TUD XPROP-S propeller (Ø203.2 mm) [39]. (c) Technical drawing of the rotatable sideplate used for α control.

The test section with the propeller rig and airfoil model installed, along with the sting clamping arrangement, is shown in Fig. 2.9. For each test, the propeller clamp is fixed at a specific spanwise location, and measurements are recorded at that position. The clamp is then repositioned to the next spanwise location, and the measurements are repeated. This process is carried out sequentially for all spanwise positions of interest.

The propeller is placed at a distance of one Dia_{prop} away from the airfoil model. This is to ensure a minimum upstream effect of the airfoil on the propeller loading. Since force measurements are unavailable for this setup due to the lack of a load cell, it is not possible to measure or quantify changes in the propeller loading. To address this, the setup is designed to minimise such effects and instead focus on the interactions on the airfoil surface. Furthermore, the airfoil is mounted perpendicular to the sting to reduce wake interference from the sting itself. A significant change to the airfoil model, as compared to the first experiment, is the removal of the transition trip.

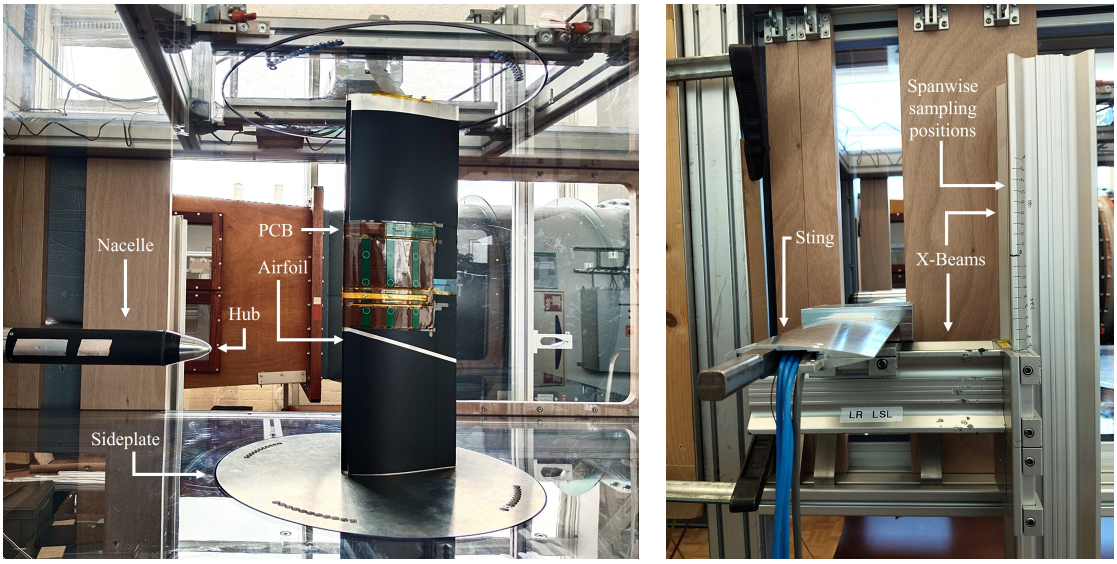

Figure 2.9: (a) View of the test section with the nacelle and airfoil model installed. The propeller is not mounted in this configuration, illustrating the nacelle-only case. (b) Clamping mechanism of the propeller rig showing the horizontally mounted sting and the X-beams used to vary the vertical position for spanwise sampling.

As discussed earlier, it is important to discuss the arrangement of the microphones and pressure sensors on the device. The coordinate system of each microphone and pressure sensor is kept constant for the test cases of this experiment. Figure 2.10 shows the arrangement of the concerned microphones on the device when it is wrapped around the airfoil (suction side).

Figure 2.10: Illustration of the device layout when wrapped around the LE of the airfoil model (suction side view). The illustration is not to scale; sensor dimensions and coordinates are exaggerated for clarity. However, the relative ordering and arrangement of the microphones and pressure sensors accurately reflect the physical configuration. Circles represent the microphones and squares represent the pressure sensors, with their respective channel numbers annotated. The propeller shown is for illustrative purposes only and does not represent the geometry or specifications of the TUD XPROP-S.

It is essential to note that the chordwise coordinates of the device microphones and pressure sensors differ on the suction and pressure sides of the airfoil model.

TUD XPROP-S (Ø203.2 mm): $30°\beta$ **and** $45°\beta$

The performance data for TUD-XPROP-S (Ø203.2 mm) were not available, and a performance study prior to the current work was also not possible; hence, the performance data of TUD-XPROP (Ø406.4 mm) are used as a reference. This is deemed acceptable since TUD-XPROP-S is a half-scaled version of TUD-XPROP [29]. The TUD-XPROP-S used in the current study is a 6-bladed left-handed propeller (counter-clockwise rotation as seen from the TE of the airfoil model) with a radius of 101.6 mm. For this experiment, one 200 mm span extension of the NACA 63_3-018 airfoil is used. The span of the airfoil model for this experiment is 600 mm. The performance data of the TUD XPROP (Ø406.4 mm) can be referred to from Appendix Fig. A.5.

In this experiment, two TUD XPROP-S propellers with different blade pitch angles of $45°\beta$ and $30°\beta$ at 70% of the blade radius are used. These are operated at different values of J to achieve various thrust conditions. The $30°\beta$ when operated at $J = 0.8$, produces a high positive thrust, while at $J = 1.8$ it operates in a negative thrust regime. At $J = 1.8$, the $45°\beta$ propeller generates positive thrust and yields maximum efficiency in this regime, while the $30°\beta$ propeller achieves peak efficiency in the negative thrust regime. The blade chord and pitch distributions of both the TUD XPROP-S $30°\beta$ and $45°\beta$ propellers are shown in Fig. 2.11. alongwith the photographs of the propellers.

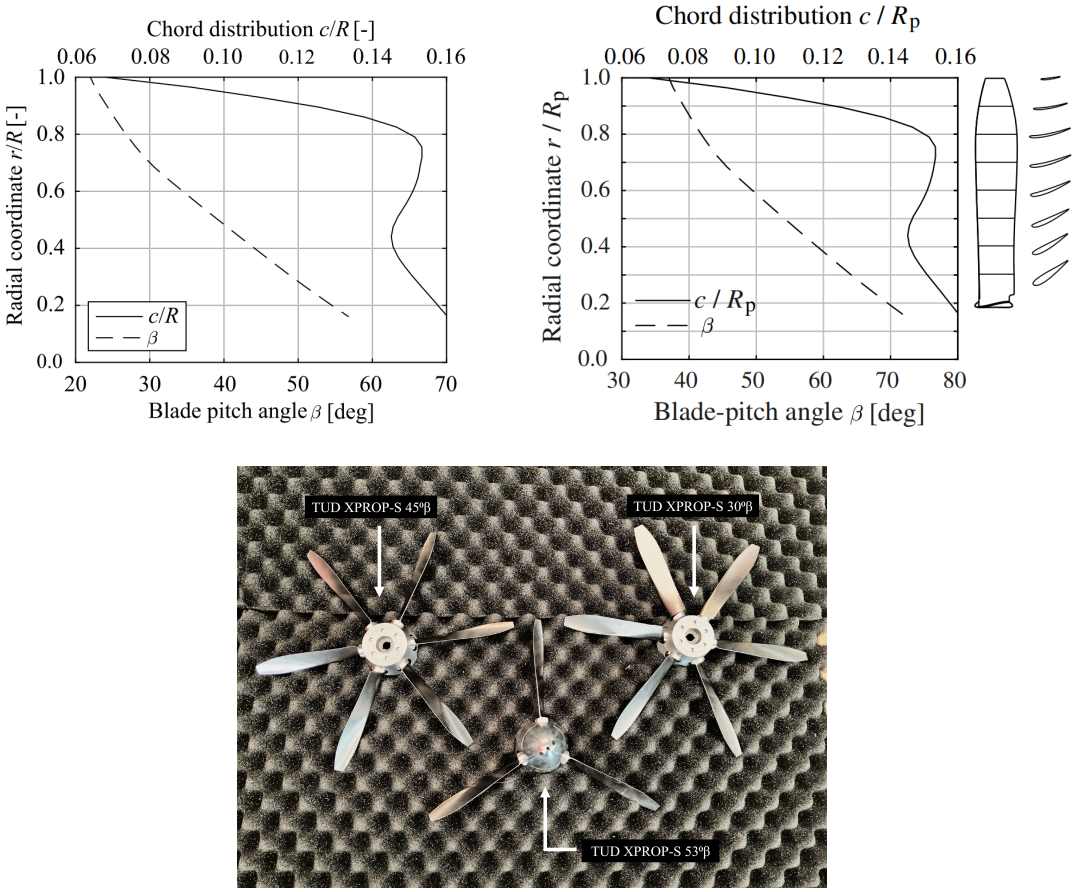

Figure 2.11: Blade chord and pitch distributions of the TUD XPROP-S: (a) $30°\beta$ [38], (b) $45°\beta$ [39]. (c) Photographs of the three TUD XPROP-S propellers used in the study. Results are presented only for the two configurations relevant to this work.

The J is varied by adjusting the RPS of the propellers through the motor control interface, as shown in Appendix Fig. A.3. The RPS values corresponding to $J = 0.8$ and $J = 1.8$ are 123 and 54.7, respectively.

Oil-Flow Visualization

To visualise the surface flow characteristics, the Fluorescent-Oil Film Method is used. As described by Donald L. Loving and S. Katzoff (1959) [40], the surface is coated with a film of fluorescent oil, and shearing in the boundary layer is observed. These changes are qualitative and are detected using ultraviolet (UV) light. A mixture of light paraffin oil and UV-luminescent material is applied on the suction and pressure sides. This procedure is repeated for each test case, with images captured during tunnel operation under UV illumination via a camera. After each run, the oil mixture is reapplied to ensure consistent coverage. It is important to note that the vertical orientation of the airfoil model introduces significant gravitational effects on the oil flow. Therefore, care must be taken to distinguish actual flow phenomena from artefacts induced by gravity. Images of the setup are shown in Fig. 2.12.

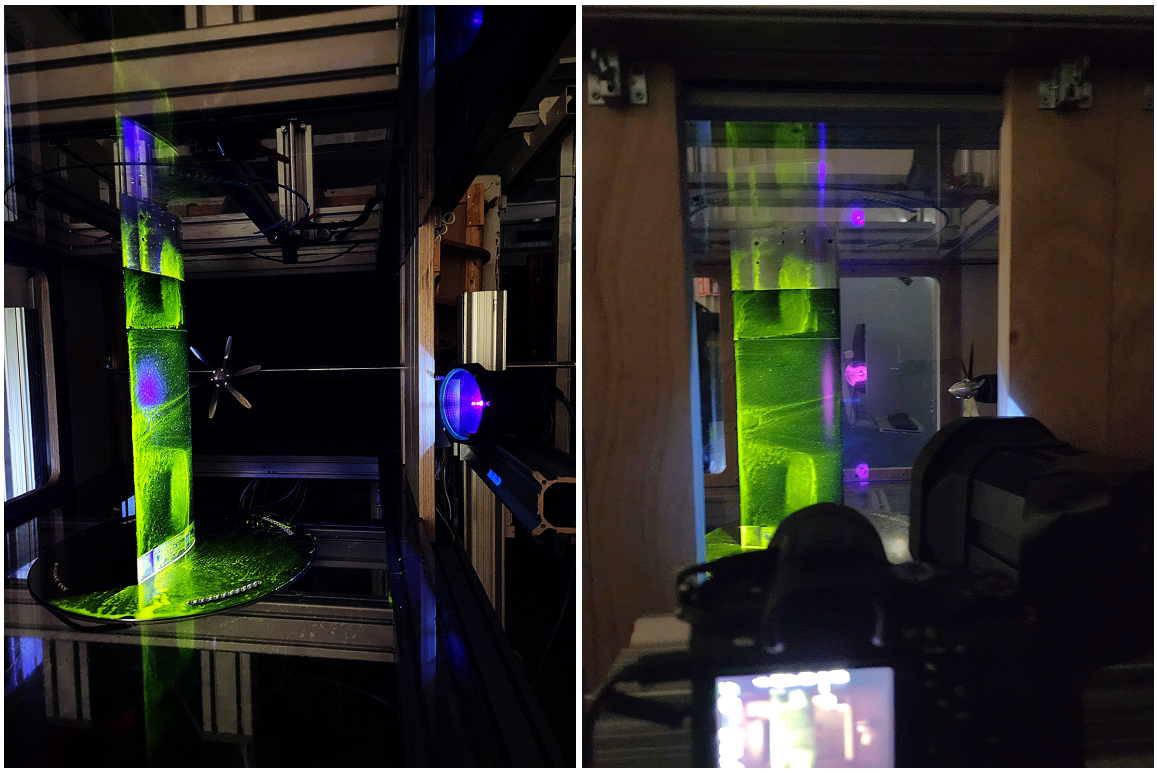

Figure 2.12: Oil-Flow visualisation setup.

2.4 Data Processing

The steps to analyse the data from the microphones are outlined and discussed in the subsequent paragraphs. The primary focus is on computing the Power Spectral Density (PSD), Root Mean Square of pressure fluctuations (p_{rms}) and the Phase-Locked Averaging (PLA) to quantify the unsteady pressure fluctuations across different test conditions. The aim of this discussion is to highlight the significance of specific techniques employed in this study.

2.4.1 Power Spectral Density (PSD)

To analyse the time-domain signal obtained from the microphones of the device, it is essential to understand the frequency content. This is done by transforming the signal into the frequency domain. The microphones detect the related air pressure corresponding to the sum of multiple frequencies. And hence, to analyse these frequencies, a transformation is required. This is similar to breaking down or deconstructing an already prepared dish into its individual ingredients, either to identify the source of a distinct flavour or to understand the overall composition of the recipe.

In the frequency domain, different spectra can be analysed based on the study's goal. Hence, it is important to consider what the study aims to achieve. In the current study, the goal is to analyse how power in the signal is

distributed across each frequency band and identify the corresponding physical flow phenomena, such as vortex shedding, boundary layer instabilities, and blade passage effects. Hence, the PSD is an important tool for this purpose.

For a stationary function $f(t)$, the PSD ($S_{11}(\omega)$) is given by the Fourier transform of the autocorrelation function [41]. It is given by Eq. 2.5 and Eq. 2.6, where $R_{11}(\tau)$ is the autocorrelation function in the time domain.

$$\overline{|f_1(t)|^2} = \int_{-\infty}^{\infty} S_{11}(\omega)\, d\omega \tag{2.5}$$

$$S_{11}(\omega) = \int_{-\infty}^{\infty} R_{11}(\tau)\, e^{-i\omega\tau}\, d\tau \tag{2.6}$$

To enable spectral energy distribution over finite sampled data, the Discrete Fourier Transform (DFT) is used along with appropriate normalisation based on the number of samples and sampling frequency. It can be computed using Eq. 2.7, where F_s is the sampling frequency, N is the number of samples, k refers to the specific discrete frequency bins and $X(k)$ is the coefficient of the double-sided DFT.

$$\text{PSD}(k) = \frac{1}{F_s N} |X(k)|^2 \tag{2.7}$$

Here, N is the normalisation factor to account for the length of the time signal, ensuring that the energy per sample is correctly distributed across frequencies. F_s converts the frequency bin spacing to Hz. This is for the discrete domain. PSD is expressed in Pa^2/Hz.

The DFT can be expressed by Eq. 2.8. Here, x_n can be thought of as a matrix consisting of the discrete time data, and it is multiplied with a matrix consisting of complex numbers corresponding to the sine (imaginary) and cosine (real) of a certain frequency for k_n where $n = 0$ to $N - 1$.

$$X[k] = \sum_{n=0}^{N-1} x_n \cdot e^{-i\frac{2\pi}{N}k_n} \tag{2.8}$$

Computing the DFT of a discrete-time signal is important for analysing its frequency content, and its significance can be understood through Parseval's theorem, which relates the total energy in the time domain to that in the frequency domain. It can be inferred that summing the spectral power across frequencies is equal to summing the power at each sample in the time domain. However, computing the DFT for large datasets is computationally expensive. Hence, to address this issue, Fast Fourier Transform (FFT) is used. The FFT is mathematically equivalent to the DFT, but it is a more efficient method for computing the DFT.

In the current study, the Welch's method is used to compute the PSD. This method is advantageous due to its ability to reduce variance in the PSD estimate by averaging modified periodograms from overlapping windowed segments, as compared to the previously discussed method. However, while Welch's method provides a smoother estimate, especially for stochastic or noisy signals, it does so at the cost of reduced frequency resolution due to the segmentation process. The initial step involves dividing the signal into overlapping segments and applying a window function (such as Hanning) to each segment to reduce spectral leakage. Then, the FFT is computed for each windowed segment, and the corresponding PSD is obtained. Finally, the PSDs from all segments are averaged. The Welch's method is still consistent with Parseval's theorem when averaging over multiple segments.

The aforementioned steps are implemented using MATLAB's pwelch function [42]. A Hanning window with 50% overlapping is used. A Hanning window is useful in reducing spectral leakage, while overlapping ensures that the attenuated signal for one window is not lost and is accounted for in the next segment. Spectral leakage is the smearing of spectral content across frequencies, which occurs when computing the FFT of a non-periodic signal segment.

During microphone calibration, Sound Pressure Level (SPL) is used as a metric to verify that the output of the SPL from the pistonphone is observed in the recorded signal. SPL quantifies the pressure fluctuations of a sound wave relative to a reference pressure (20 μPa in air).

2.4.2 Root Mean Square of Pressure Fluctuations (p_{rms})

To quantify the unsteady pressure fluctuations measured by the device microphones, the RMS of the pressure signal at each individual microphone is computed. It captures the amplitude of pressure fluctuations for a particular microphone over time. In the flow downstream of a propeller, strong pressure oscillations are observed, and the p_{rms} helps quantify the amplitude of these oscillations. It is given by Eq. 2.9.

$$p_{\text{rms}} = \sqrt{\frac{1}{N}\sum_{i=1}^{N} p_i^2} \tag{2.9}$$

Here, p_i represents the instantaneous pressure at time step i, as measured by the device's microphones, and N denotes the total number of samples.

However, it is important to note that the p_{rms} only indicates the absolute magnitude of the fluctuations. Therefore, additional post-processing steps are necessary to identify regions influenced by the convecting tip vortex trace across the airfoil.

2.4.3 Phase-Locked Averaging (PLA)

To isolate the periodic unsteady pressure fluctuations induced by the propeller, the PLA is applied to the data from the microphones. By averaging pressure fluctuations at the same phase angle over multiple revolutions of the propeller, periodic effects caused by the blade passage can be quantified while averaging out the random effects. With the help of the encoder placed in the propeller shaft, a one-per-revolution trigger signal is obtained. The microphone data is measured synchronously with this trigger signal. The encoder signal is a square wave that is stored in channel Sync54. A rising edge in the encoder signal marked the start of each revolution, which is used to segment the pressure data into individual revolutions. The subsequent paragraphs provide a detailed discussion of this topic.

The measurement data is stored in a TDMS file, which includes signals from 18 microphone channels, 6 static pressure sensors, and temperature readings. Additionally, the Sync54 channel in the TDMS file contains the encoder signal sampled synchronously with the microphone data. The data in the Sync54 channel consists of a square wave signal, alternating between 0 and 1. A change from 0 to 1 (rising edge) marks the start of a propeller revolution. The next rising edge marks the end of that revolution and simultaneously the start of the next. Therefore, each complete revolution is defined between two successive rising edges. A change from 1 to 0 is the falling edge preceding the subsequent rising edge. This process is illustrated in Fig. 2.13. The sample indices corresponding to the rising edges are used to segment the microphone data into individual revolutions.

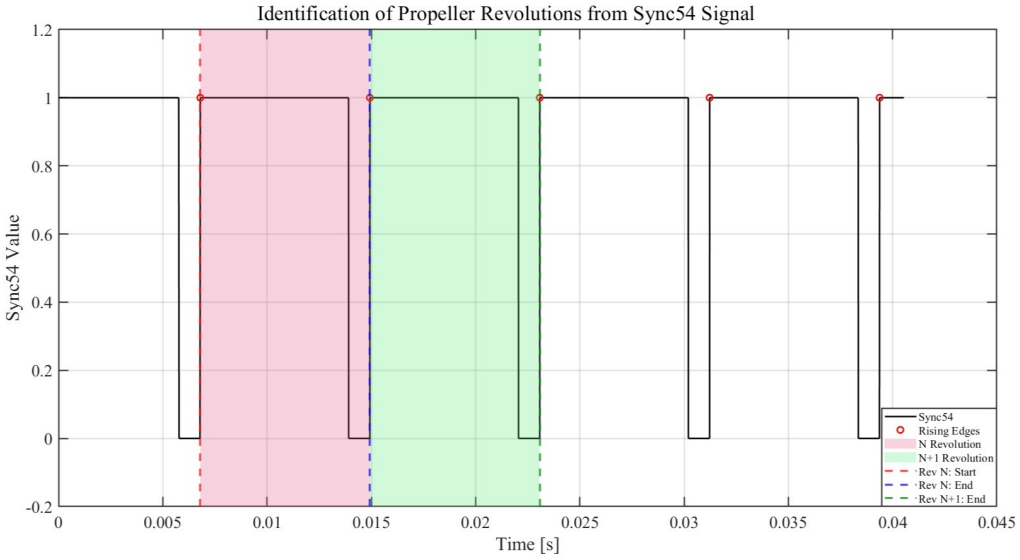

Figure 2.13: Identification of propeller revolutions based on the rising edges from Sync54 channel data.

Before averaging, it is essential to ensure that the revolutions are of equal length. To achieve this, each revolution is divided into 360 phase bins. The subsequent averaging process averages out random, non-periodic fluctuations while preserving pressure features that are synchronised with the propeller's rotation, such as vortex impingements or wake interactions. The blade phase angle serves as a temporal coordinate system to analyse the blade passage phenomena. However, the raw microphone data for each revolution does not inherently contain exactly 360 samples. Therefore, interpolation is performed to resample the pressure signal from each revolution to exactly 360 uniformly spaced phase bins. This ensures that all revolutions are consistently represented from $\phi = 0°$ to $\phi = 359°$.

Once this interpolation is complete, the phase-aligned data from multiple revolutions can be averaged bin by bin to obtain the PLA signal. This process averages out random, non-periodic fluctuations while preserving pressure features that are synchronised with the propeller's rotation, such as vortex impingements or wake interactions. The resulting p'_{PLA} values are then used to compute the phase-locked unsteady pressure coefficient, C'_p, as shown in Eq. 2.10.

$$C'_p(\phi) = \frac{p'_{\text{PLA}}(\phi)}{q_\infty} \tag{2.10}$$

The conventions for the retreating and advancing blade sides with respect to the airfoil model are shown in Fig. 2.14.

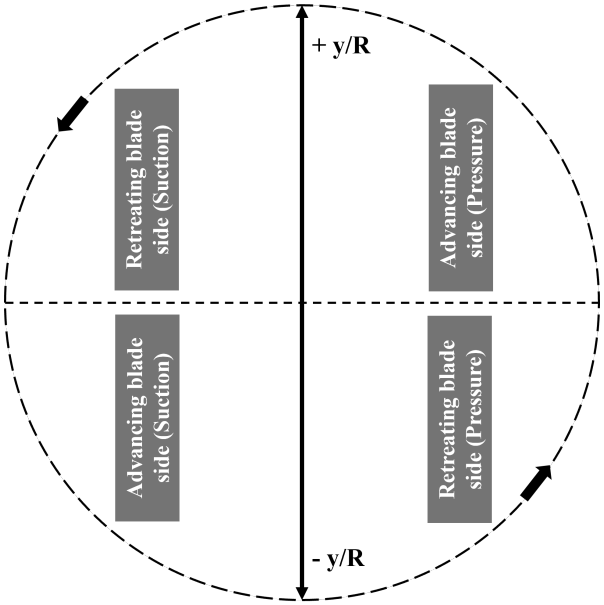

Figure 2.14: The conventions for the retreating and advancing blade sides with respect to the airfoil model. Positive values of y/R (spanwise locations on the airfoil normalised by propeller radius) correspond to the retreating blade side of the propeller, while negative values correspond to the advancing blade side for the suction side, and vice versa for the pressure side. The arrows denote the direction of propeller rotation as viewed from the TE of the airfoil model.

3

Validation of the Device: The First Experiment Results

This chapter presents the results from the first experiment, which focuses on validating the findings obtained with a flexible PCB embedded with microphones and pressure sensors. The validation was conducted under multiple conditions, including known tone excitation (3.1.1) and flow in the wake of an upstream cylinder (3.1.3) to test the response of the microphones. This was followed by the calibration of the microphones with a GRAS pistonphone (3.1.2). Additionally, static pressure measurements (3.2) from the device were compared with XFOIL predictions to assess the accuracy of the pressure sensor readings. These tests are crucial for verifying the device's suitability for more complex aerodynamic investigations that involve propeller slipstream-induced interaction effects.

3.1 Validation of the Microphones

3.1.1 CASE A: Known Tone Excitation

A known tone of 500 Hz is passed through a smartphone placed near the first rows of microphones, with the device positioned outside the wind tunnel. The PSD is plotted to verify the frequency content and the dominant frequency of the recorded tone, ensuring that the microphone array correctly captured the 500 Hz signal. This preliminary yet essential test is followed by microphone calibration, which is carried out to determine the appropriate gain corrections to be applied.

The PSD plot for Microphone 0 (according to the layout illustrated in Fig. 2.5) is shown in Fig. 3.1. Microphone 0 is selected since the source of the tone is closest to the first row of mics.

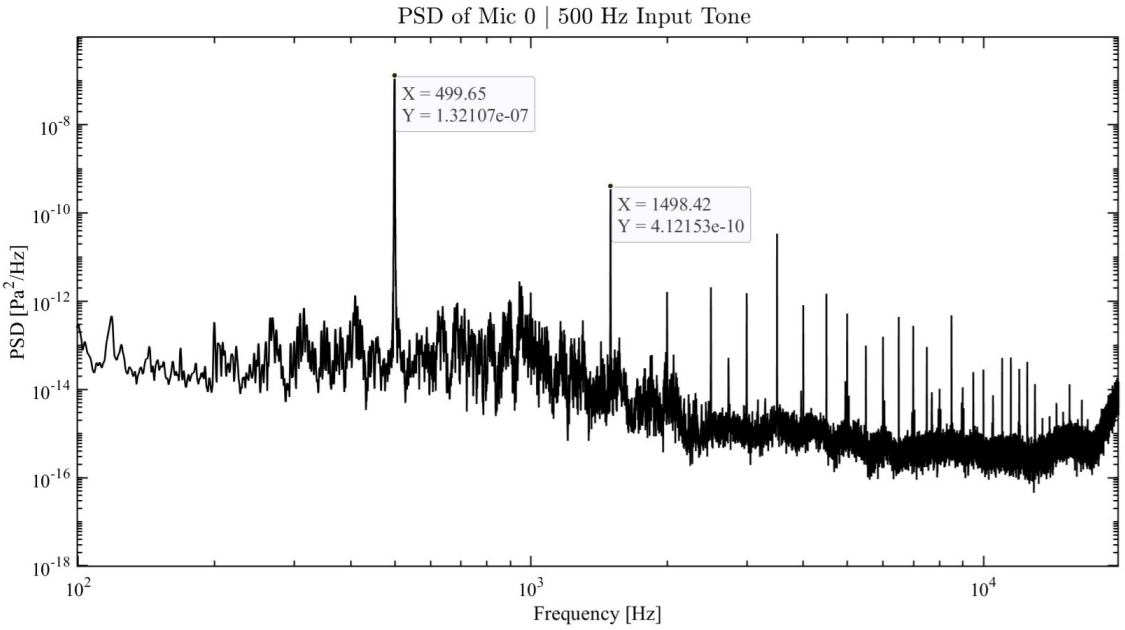

Figure 3.1: PSD of the signal from Microphone 0 and the corresponding fundamental frequency and the third harmonic.

From the PSD plot, it can be observed that the most energetic peak occurs at 499.649 Hz, which closely matches the source tone of 500 Hz. The second most energetic peak corresponds to the third harmonic of the fundamental frequency. Selecting a 500 Hz tone is deemed helpful in checking whether the microphones are measuring simultaneously. This is because, from the PSD results, the wavelength of the third harmonic is comparable to the physical spacing between the first and last microphones (Mic 0 and Mic 10) in the array. The layout can be referred to from Fig. 2.5. The wavelength of the 499.649 Hz tone can be calculated using Eq. 3.1.

$$\lambda_1 = \frac{c}{f_1} \approx 686.4\,\text{mm} \tag{3.1}$$

Similarly, the value of $\lambda_3 \approx 228.9$ mm. Now, considering the third harmonic, the travelling wave is detected by the six in-line microphones. Assuming a constant propagation speed c and a planar wavefront, the measured time delay between microphones 0 and 10 can be used to estimate the distance the wave has travelled. This estimated distance should correspond to the known physical spacing between the microphones. The agreement between these values serves as a validation that the microphones are accurately capturing the wave propagation.

The value of λ_3 is close to the distance between Microphone 0 and Microphone 10 as seen in 2.5, which is 240 mm. These microphones are in the same chord-wise column; hence, a cross-correlation is performed to verify whether the time lag corresponds to a physical distance comparable to the actual distance between the two microphones. The cross-correlation yielded a value for the distance of approximately 201 mm, which is in good agreement with the known spacing between Mic 0 and Mic 10.

This is followed by a time-domain analysis to verify the time period of the sine wave signal played through a smartphone. For the 500 Hz tone used, the expected time period is approximately 2 ms. The time period (T) is given by Eq. 3.2.

$$T = \frac{1}{f_1} \approx 2.0014\,\text{ms} \tag{3.2}$$

The time-domain plot for Microphone 1 is shown in Fig. 3.2. The signal is unfiltered and exhibits noise, as the test is conducted outside the wind tunnel and in a lab environment that is not acoustically treated. Additional tests conducted at other known frequencies, such as 1000 Hz and 1500 Hz, also produced distinct peaks at the respective frequencies, which supports the reliability of this preliminary validation.

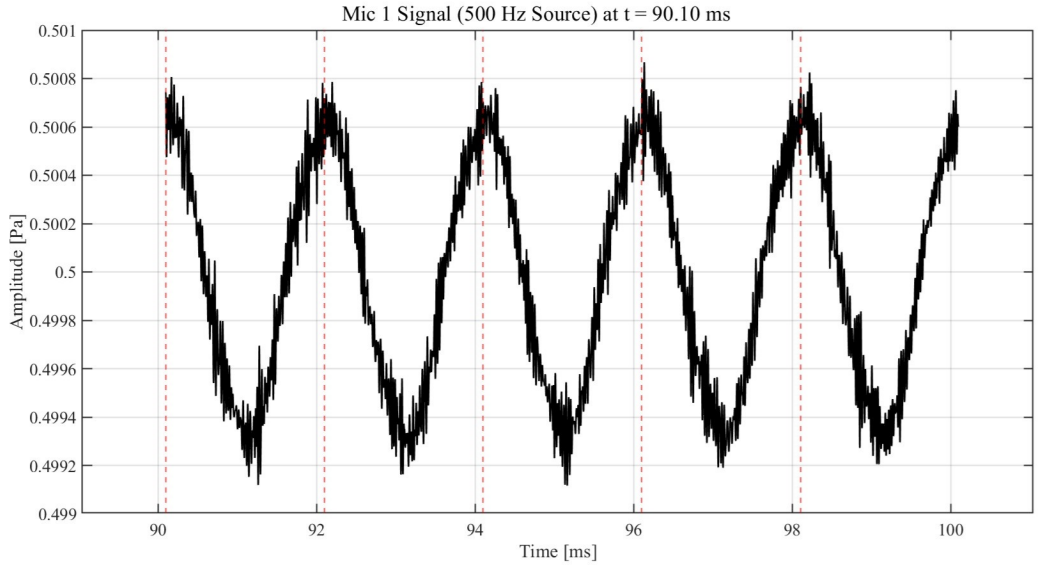

Figure 3.2: Time-domain analysis of Microphone 1 for the known tone of 500 Hz at 90.10 ms for 10 ms.

3.1.2 Calibration of the Microphones

The microphones are calibrated using a GRAS piston-phone at 1 kHz and an SPL of 114 dB. The SPL is given by Eq. 3.3, where p_{ref} is 20 μPa (in air).

$$\text{SPL} = 20 \log_{10} \left(\frac{p_{\text{rms}}}{p_{\text{ref}}} \right) \tag{3.3}$$

From the above equation, the expected p_{rms} is computed. Each microphone's output is compared to this expected value, and a gain factor is applied to each microphone signal accordingly. Let the raw signal output of the microphone be denoted as s, and the corrected pressure be:

$$p = G \cdot s \tag{3.4}$$

where G is the gain factor. The gain is determined such that the microphone output matches the expected pressure:

$$G = \frac{p_{\text{rms,expected}}}{s_{\text{rms,measured}}} \tag{3.5}$$

This gain, G, is then applied to all subsequent recordings for that microphone to ensure a consistent response from all microphones.

The PSD is then plotted to assess whether the microphones exhibited a consistent frequency response. The plot for the first four microphones is shown in Fig. 3.3.

All microphones, except for Mic 14, display a consistent frequency response. A combined plot for all microphones can be referred to in Fig. A.6 of the Appendix. Hence, the gain data are suitable for further data processing.

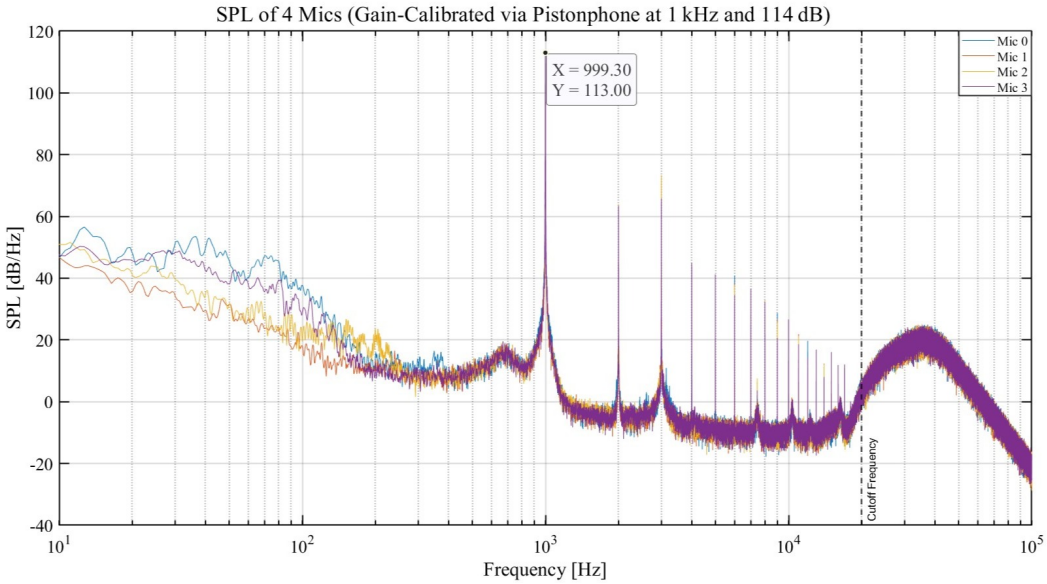

Figure 3.3: SPL of the signals from the first four microphones on the device after applying the respective gain values.

3.1.3 CASE B: Vortex Shedding Response from Upstream Cylinder

In this case, a cylinder is placed upstream of the model as shown in Fig. 2.6. The device is tested for multiple inflow velocities of 5 m/s, 10 m/s, 15 m/s and 20 m/s to verify if the Strouhal number obtained from the measured data corresponds to an acceptable value as compared to the expected Strouhal number (St) for a circular cylinder, which is 0.2 **[43] [44]**.

St can be defined as "the ratio of inertial forces due to the local acceleration of the flow to the inertial forces due to the convective acceleration" **[45]**, and is instrumental in studying the characteristics of vortex shedding due to bluff bodies and other oscillating flow mechanisms. It is given by Eq. 3.6.

$$St = \frac{fD}{U_\infty} \tag{3.6}$$

Here, D is the diameter of the cylinder (19.05 mm) and f is the shedding frequency that can be obtained from the PSD of the dataset.

The PSD of the test case for V_∞ = 20 m/s at Mic 7 is shown in Fig. 3.4. The microphone layout can be referred to from Fig. 2.5. The offset data (wind tunnel off) is subtracted from the raw data, and the gain is multiplied for each microphone channel.

The real flow behind a circular cylinder is governed by the Reynolds number Re. At very low Reynolds number (Re < 40), the flow is in the Stokes (creeping) regime. As the Reynolds number increases beyond $Re \approx 40$, a periodic vortex street known as the von Kármán vortex street forms. At higher Reynolds numbers (10^3 - 10^5), the wake becomes increasingly turbulent **[46]**.

The Re (with respect to the cylinder diameter) in the current experiment for V_∞ of 20 m/s is approximately 2.5 x 10^4 in the sub-critical Re range, where the value of St remains nearly constant at around 0.2 for flow over a circular cylinder **[43]**. In this subcritical regime, the wake is characterised by the formation of a von Kármán vortex street accompanied by the growth of three-dimensional instabilities and breakdown to turbulence. The unsteady wake results from the separation of the boundary layer on either side of the cylinder, leading to the alternate shedding of vortices at a frequency that depends on the flow velocity and cylinder geometry.

A distinct tonal peak in the PSD is observed, corresponding to this vortex shedding frequency. From Fig. 3.4 the shedding frequency for V_∞ = 20 m/s is 210.392 Hz. From this value, the St can be determined using Eq. 3.6. Hence, $St_{20} \approx 0.2003$. This value is in agreement with the reported value of 0.2 in the literature in the range of Re of 5 x 10^2 - 5 x 10^5 **[43] [44]**. Here, Re is given by Eq. 3.7, where D is the diameter of the cylinder.

$$\mathrm{Re} = \frac{\rho_\infty V_\infty D}{\mu_\infty} \tag{3.7}$$

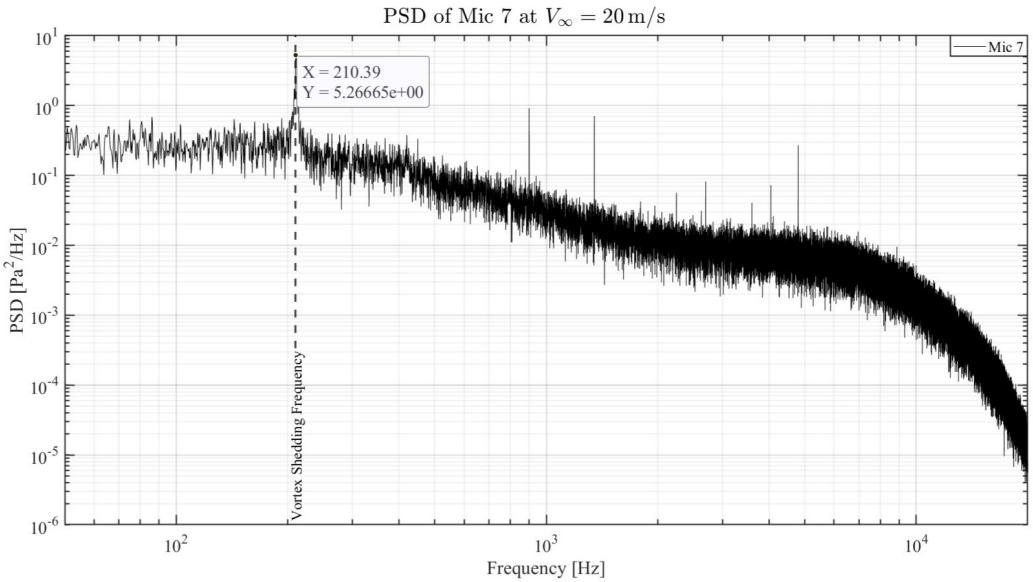

Figure 3.4: PSD of Mic 7 for CASE B at $V_\infty = 20\,\mathrm{m/s}$.

As expected, the shedding frequency exhibits a linear dependence on the V_∞, consistent with the literature **[43]**. This is observed across measurements at velocities of 5 m/s, 10 m/s, 15 m/s and 20 m/s, which yield the corresponding vortex shedding frequencies of 52.12 Hz, 106.65 Hz, 160.90 Hz and 210.392 Hz, respectively.

Additionally, for V_∞ = 5 m/s, 10 m/s and 15 m/s, the $St \approx 0.1986$, 0.2031 and 0.2043 respectively. The plots for the same can be referred to from Section A.4 of the Appendix. The data can be further filtered to reduce noise; however, for this particular test of calculating the St, it is not a significant concern.

3.2 Validation of the Pressure Sensors I

The data from the device pressure sensors is compared with the data from the pressure taps. This is essential since the pressure data from the device must be verified against data from conventional methods to determine the reliability. Once verified, the pressure data can be independently utilised for different test samples under various conditions. Hence, this section focuses on validating the pressure data obtained from the device.

However, before comparing the device data, it is necessary to validate the pressure tap measurements first. To achieve this, the pressure tap data is compared to results from XFOIL. Additionally, it is essential to determine an appropriate sampling duration to ensure statistical convergence. The normalised running mean of pressure at Tap 5 is evaluated by averaging the signal over time and normalising it with respect to its final mean value. A sampling time of 60 seconds is used for this convergence test, and the results indicate that a sampling time of 30 seconds is sufficient (see Fig. A.8). Therefore, all subsequent pressure tap measurements are taken with a 30-second sampling duration.

This is followed by comparing coefficient of pressure (C_p) graphs for XFOIL and the pressure taps at a non-zero α of 6° and V_∞ = 20 m/s wherein, a trip is included in the XFOIL code at 0.05c (measured from LE) on both upper and lower surfaces. This is shown in Fig. 3.5.

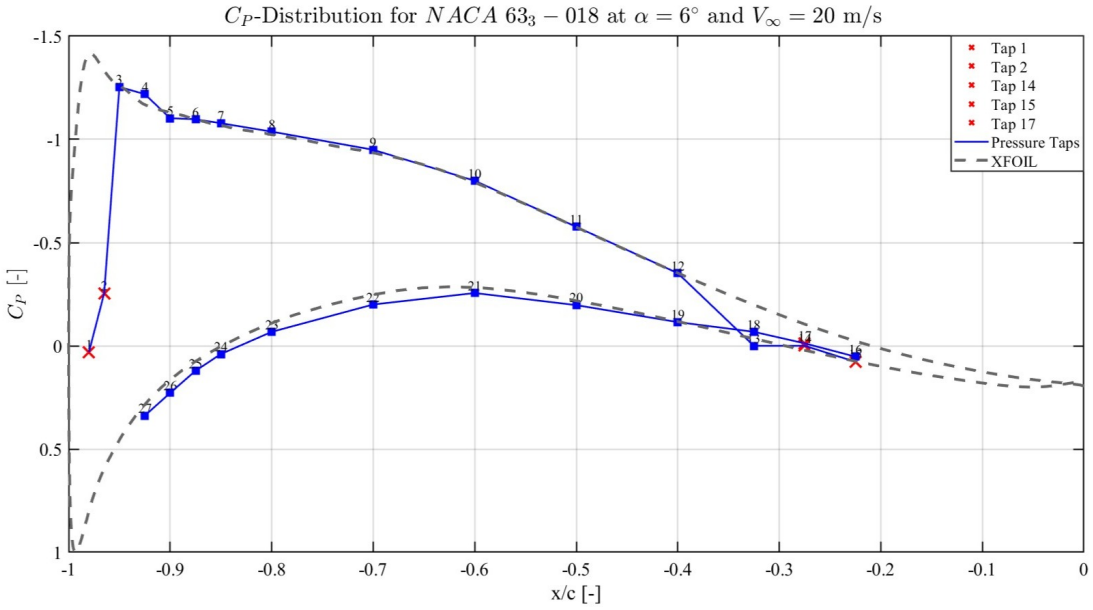

Figure 3.5: C_p distribution for NACA $63_3 - 018$ at $\alpha = 6°$ and $V_\infty = 20$m/s.

The malfunctioning taps are marked in the plot. The process is also repeated for V_∞ values of 5, 10, and 15 m/s, all of which show good agreement with the XFOIL predictions. Since the pressure tap measurements provided reasonable data that closely aligned with the XFOIL results, they are considered the "true values" and used for validating the pressure sensors of the device.

The device is wrapped around the airfoil and placed in the wind tunnel at $\alpha = 5.5°$ and $V_\infty = 20$ m/s at four different positions. However, the pressure sensor measurements do not align with the values from pressure taps and the XFOIL predictions, yielding significant overshoots that indicate higher suction. This discrepancy arises because the pressure sensors protrude from the airfoil surface. Although their height is relatively small (0.75 mm), they still induce localised regions of accelerated flow, leading to artificially high suction values. The discrepancy observed across four different mounting positions of the device on the airfoil model is presented in Fig. A.9 of the Appendix. Fig. 3.6 is an illustration to depict the protrusion of the pressure sensors.

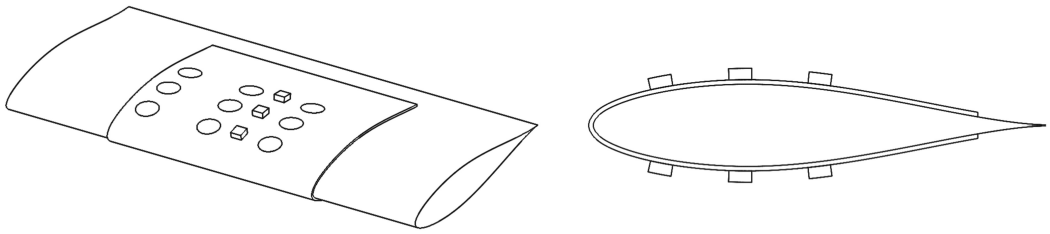

Figure 3.6: Illustration of the device mounted on the airfoil model. The circles represent the microphones, while the squares depict the pressure sensors. This figure highlights the protrusion of the pressure sensors from the surface. The protrusion height has been intentionally exaggerated for visual clarity. This figure is for illustrative purposes only and not drawn to scale.

This is a key finding, as it highlights the need for measures to account for sensor height discontinuities in low Re wind tunnel tests, such as using a sleeve. While the measured pressure values are inaccurate, the overall trend remains consistent. Therefore, corrections are implemented in the second experiment conducted in the Small Low-Turbulence (SLT) wind tunnel. This is described in Section 4.1. All the results of the experiments conducted in the SLT are discussed in Chapter 4.

4

Propeller Wake-Wing Interactions: The Second Experiment Results

This chapter presents and discusses the results obtained from the second phase of the experimental campaign, where the device is mounted on a downstream airfoil model immersed in the slipstream of an upstream pusher propeller. The TUD XPROP-S propeller, operating at a constant wind tunnel speed of 20 m/s, has been used for this study. The rotational axis of the propeller was kept as parallel to the freestream as possible[1]. The objective of this experiment is to characterise the unsteady surface pressure fluctuations induced by the propeller wake under different operating conditions. Comparisons between different cases are drawn based on the p_{rms}, PSD and phase-averaged results.

It is essential to reiterate that the chordwise coordinates (x/c) (measured from the LE of the airfoil test model) of the microphones and the pressure sensors differ on the suction and pressure sides of the airfoil model. These positions are listed in Table 4.1. All results are interpreted with reference to the conventions and coordinate systems outlined in the methodology (see Chapter 2). They are illustrated in Fig. 4.1 for clarity and to avoid confusion.

Table 4.1: Chordwise coordinates (x/c) of the microphones and pressure sensors on the suction and pressure sides of the airfoil model, as measured when the device is wrapped around the leading edge of the model.

Surface	Microphones	Pressure Sensors	Chordwise Location (x/c)
Suction Side	6, 7, 14	2	0.165
	8, 9, 17	4	0.370
	10, 11, 16	5	0.620
Pressure Side	4, 5, 15	3	0.125
	2, 3, 12	1	0.325
	0, 1, 13	0	0.565

Note: In all subsequent references, the three rows of microphones will be referred to as upper, middle, and lower based on the orientation illustrated in Fig. 4.1.

[1] There is a possibility of a misalignment of the rotational axis with the freestream due to a slight droop of the nacelle.

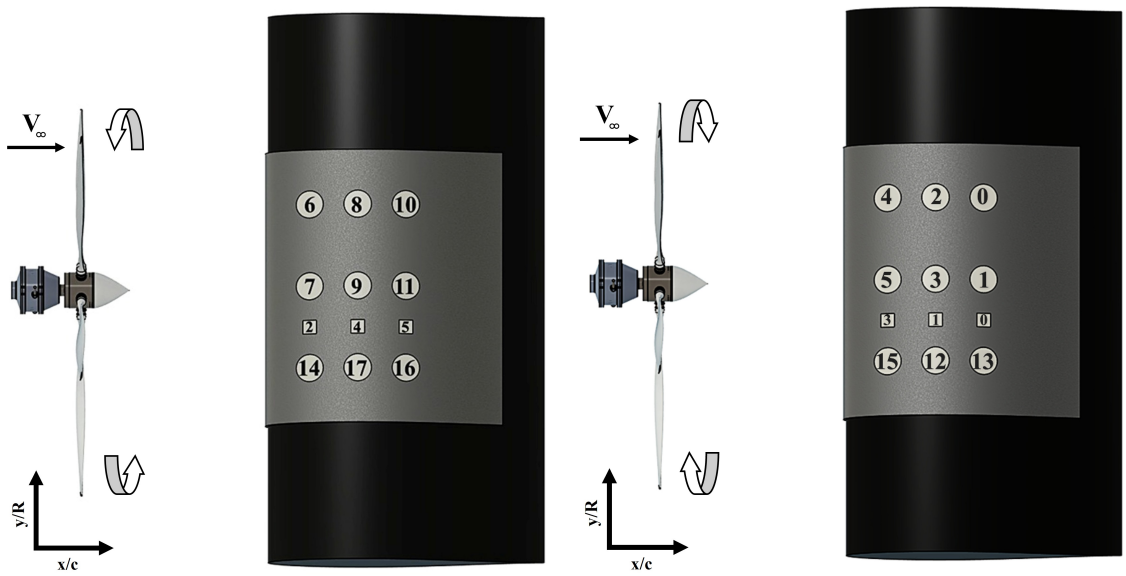

Figure 4.1: (a) Suction side. (b) Pressure side. Illustration of the device layout when wrapped around the LE of the airfoil model (counter-clockwise propeller rotation). The illustration is not to scale; sensor dimensions and coordinates are exaggerated for clarity. However, the relative ordering and arrangement of the microphones and pressure sensors accurately reflect the physical configuration. Circles represent the microphones and squares represent the pressure sensors, with their respective channel numbers annotated. The chordwise coordinates of the microphones and pressure sensors on the suction and pressure sides differ in the actual setup. This schematic is intended solely as a simplified representation of the actual setup. The propeller shown is for illustrative purposes only and does not represent the geometry or specifications of the TUD XPROP-S. The direction of counter-clockwise rotation of the propeller is annotated with arrows, as viewed from the respective sides.

4.1 Validation of the Pressure Sensors II

As discussed earlier in Chapter 3, the pressure sensors protrude out of the device surface, causing local flow acceleration around their housings. This increased the local velocity at the sensor location, resulting in lower C_p values compared to the data from XFOIL and the pressure taps. To address this issue, Kapton tape is used to compensate for the height difference caused by the sensor housing. This solved the issue by reducing the height difference, hence reducing the local flow acceleration at the pressure sensors. The setup can be seen in Fig. 4.2. The height of the tape is approximately the height of the pressure sensor (0.75 mm). It is applied in the streamwise direction and positioned between the middle and lower rows of microphones.

Figure 4.2: The placement of the Kapton tape on the device as viewed from the pressure side of the airfoil model.

The data from the pressure taps for CASE12 (nacelle only case at $9°\alpha$) after the application of the Kapton tape is shown in Fig. 4.3. The agreement between both datasets confirms that the protruding pressure sensors indeed cause the discrepancy (see Fig. A.9) and that the use of Kapton tape effectively mitigates the issue.

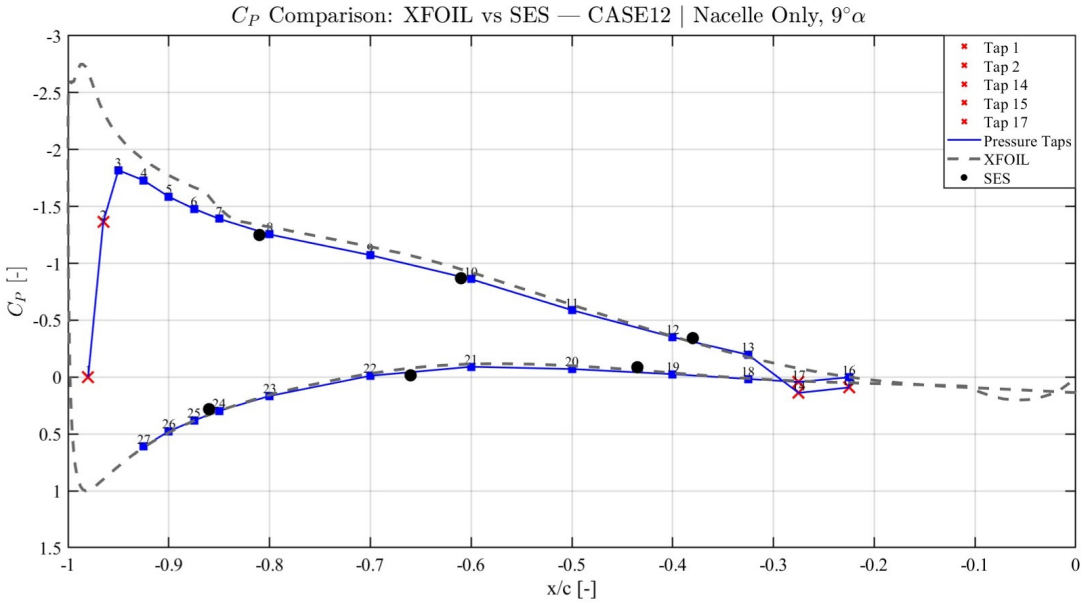

Figure 4.3: Comparision of C_p-Distribution between XFOIL predictions, pressure taps data and device measurements for CASE12 (Nacelle only, $9°$ α). The dashed black line represents the XFOIL solution. and the blue line corresponds to the pressure taps data. Black circles indicate the data from the pressure sensors of the flexible PCB device. The data is plotted against the normalised chordwise position. For clarity: SES (Sensor Embedded Sleeve) in the figure legend denotes the flexible PCB device (referred to simply as the device.)

However, the presence of this tape introduced local surface discontinuities, which influenced the response of the middle and lower rows of microphones. Thus, while it addressed the pressure sensor issue, it also caused discrepancies in the measurements from the nearby microphones, likely due to localised flow disturbances around the protruding sensors. The effects caused by this interaction are discussed in the following section.

4.2 Investigation of Row-wise Discrepancies in Microphone Response

This section discusses the variations in p_{rms} levels between upper, middle and lower microphone rows[2] at identical chordwise and overlapping spanwise locations. A consistent discrepancy is observed in the p_{rms} values measured across the three microphone rows. This discrepancy in the p_{rms} values is more pronounced for the cases with higher J and in the nacelle-only configurations. In particular, for the nacelle-only cases, the upper row consistently exhibited higher p_{rms} levels as compared to the middle and lower rows. This difference between the middle and lower rows is comparatively lower. The calibration of the microphones carried out during the first experiment ensured that this issue is not due to a variation in the response of the different microphones, but rather an issue related to the flow structures convecting over the different microphones. However, this should not be purely from aerodynamic shear or vortex jitter over the entire airfoil surface, as the differences are systematic and consistent with particular rows of microphones. This suggests that the reason could potentially be a change in the flow, particularly near the middle and lower rows of microphones. It is important to note that the nacelle-only cases are used to analyse this discrepancy because the magnitude of the difference between the microphone rows is relatively high, and the flow regime, particularly the laminar separation bubble (LSB), is well-documented in the literature. This makes it a suitable case for validating which microphone row provides the most accurate measurements. Although the highly loaded propeller cases ($J = 0.8$) also exhibited the same discrepancy, the magnitude of the difference between the rows is comparatively lower. The following paragraphs discuss the source of this discrepancy in detail.

[2]This convention of referring to the upper, middle, and lower microphone rows was introduced earlier in the device layout discussion.

4.2.1 p_{rms} Characteristics and Discrepancies

The RMS of unsteady pressure fluctuations for the nacelle only case at 6° α (CASE04) is selected for this analysis. The oil-flow image and the corresponding p_{rms} plots are shown in Fig. 4.4 and Fig. 4.5 respectively. The p_{rms} contour of the upper row accurately represents the region highlighted in the oil-flow image, whereas the middle and lower rows display a lower level of p_{rms} values.

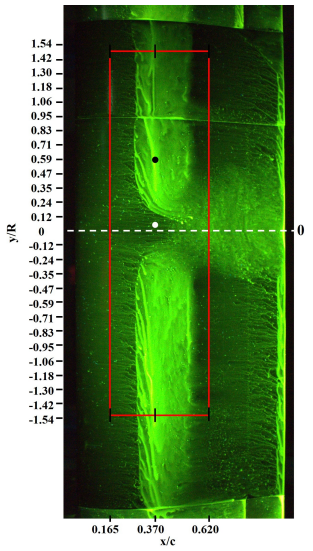

Figure 4.4: Oil-flow visualization for CASE04 (suction side). The red rectangle indicates the region used for p_{rms} analysis. The black circle and the white circle denote the location corresponding to the PSD measurements for the upper row mic. The white circle particularly corresponds to a location in the region influenced by the nacelle wake.

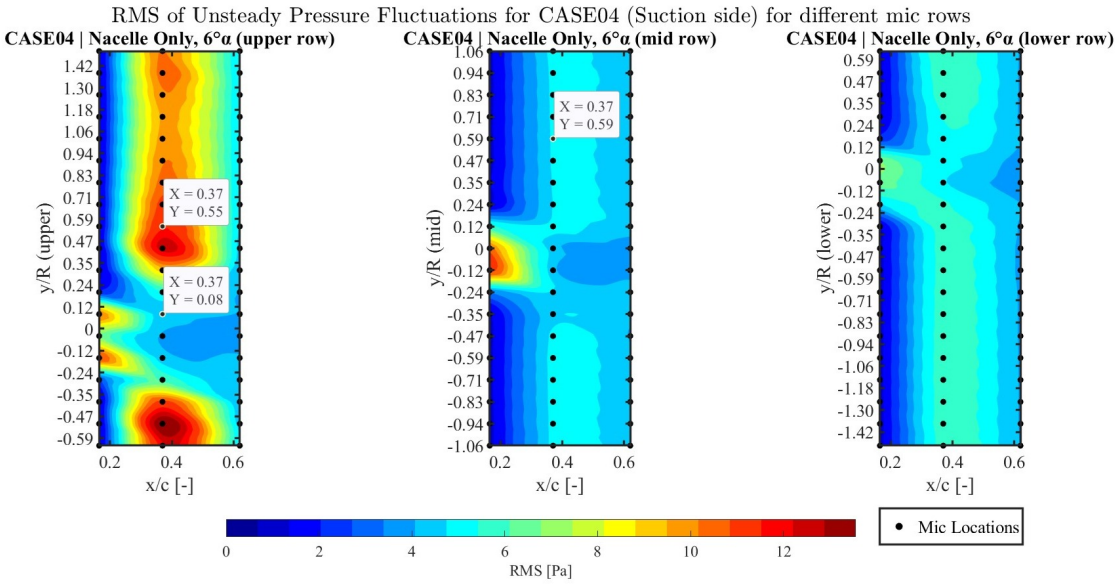

Figure 4.5: RMS of unsteady pressure fluctuations for CASE04 (suction side). The annotated point denotes the location corresponding to the PSD measurements of the upper and middle row of microphones.

There is a consistent discrepancy in the p_{rms} values between the upper row and the middle and lower rows across different cases. The nacelle-only case is used to analyse these differences, as the separated shear layer region of the LSB in this configuration forms near $x/c = 0.370$, and the magnitude of p_{rms} difference between different rows is observable. While the difference in p_{rms} levels is more pronounced between the upper row and the other

two rows, the difference between the mid and lower rows remains comparatively smaller. This behaviour can also be seen in Fig. 4.5. One possible explanation is that the placement of the Kapton tape influences both the mid and lower microphones in a similar manner, leading to comparable levels of disturbances. Furthermore, this chordwise location is particularly useful, as the flow characteristics in this region are well-documented in the literature. This allows the results from the upper row of microphones to be compared against established flow phenomena for validation. The p_{rms} of the different rows and the corresponding overlapping regions are shown in Fig. 4.6. The difference between the middle and upper row is visible from the plot.

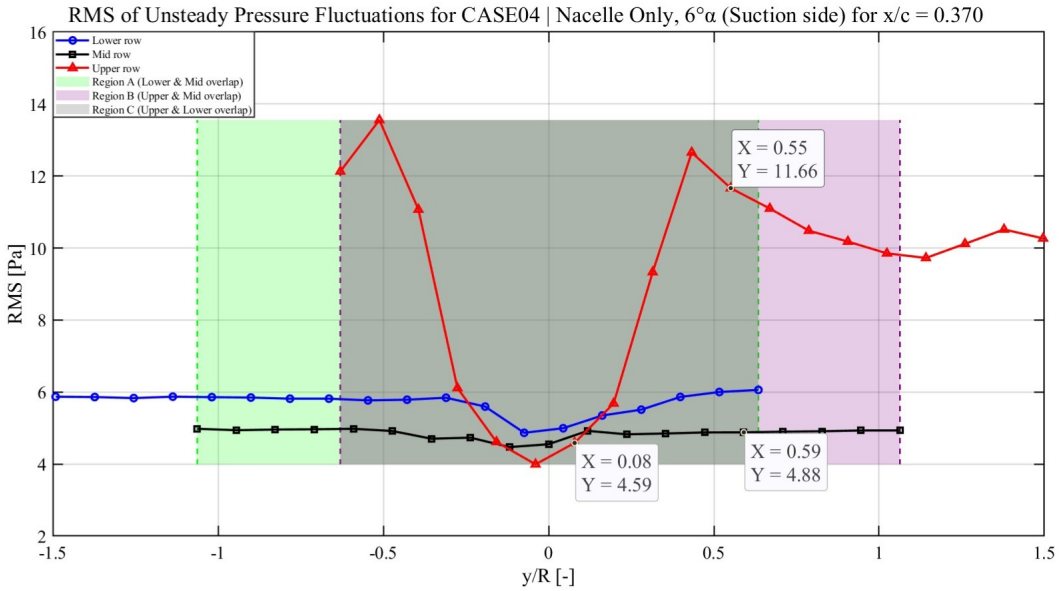

Figure 4.6: p_{rms} plot of the three rows of microphones for CASE04 suction side. The results correspond to the region highlighted in the oil-flow image across different spanwise positions and at $x/c = 0.370$. The upper and mid mics used for the PSD analysis are annotated here. The shaded overlapping regions (Regions A and B) extend between their respective coloured dashed lines. For Region C, the overlap is defined by the left dashed line of Region B (purple) and the right dashed line of Region A (green), as seen in the figure.

4.2.2 Influence of LSB and Spectral Trends Across Microphone Rows

The region of the shear layer of the LSB can be observed in Fig. 4.4. and is also illustrated in Fig. 4.7. This shear layer is unstable, leading to vortices that cause reattachment and transition to a TBL [47]. The unsteady loads associated with the roll-up process and subsequent breakdown into smaller scales correspond to high p_{rms} levels at the shear layer. The reverse flow direction leads to an upstream movement of the small-scale structures, which causes interaction with the shedding vortices. This further leads to the breakdown of the vortices into small-scale structures, leading to a TBL downstream [48]. As the LBL undergoes separation, the region of shear layer is dominated by the Kelvin-Helmholtz instability with a higher growth rate as compared to the other instabilities. K-H instability also leads to the formation of coherent structures in the shear layer [47], [49].

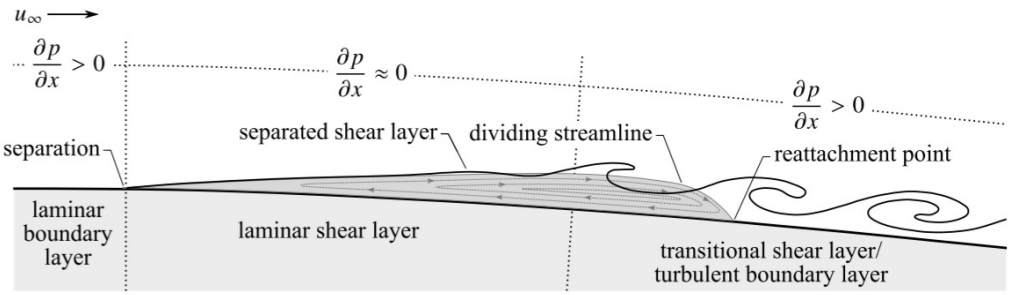

Figure 4.7: Illustration of the laminar separation bubble [47].

J. Kurelek (2021) **[47]** experimented on flow development and forcing techniques for LSBs using a NACA0018 airfoil at Re_C of 125,000 and 4° α. This is comparable to the regime of the current study at Re_C of 267,000 and 6° α. Hence, comparisons are drawn to identify the shear layer and validate the response of the microphone data. This is important to determine whether the results of the upper row of microphones correspond to the expected flow, and also to analyse the response of the middle and lower rows of microphones.

The PSD plot for upper and middle row mics at x/c = 0.370 at nearby spanwise positions is shown in Fig. 4.8. The x-axis is normalised with respect to the Strouhal number at the airfoil chord (St_C). The position of the upper row mic can be referred to from Fig. 4.4.

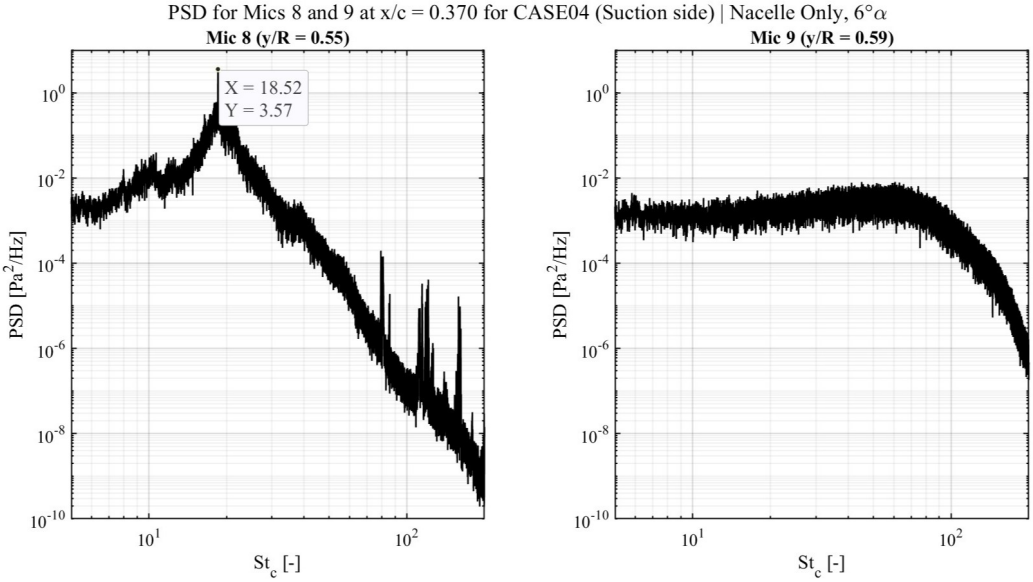

Figure 4.8: (a) Mic 8 ($y/R = 0.55$), (b) Mic 9 ($y/R = 0.59$). PSD at $x/c = 0.370$ for CASE04 (suction side). The PSD x-axis is expressed in terms of the chord-based Strouhal number St_C.

It is observed from Fig. 4.8 that the PSD of 2 different mics at nearby spanwise locations are different. This trend is consistent at all spanwise positions of the suction side case at x/c = 0.370, except for the region under the influence of the nacelle wake, which depicts a turbulent wake.

The upper row mic (see Fig. 4.8 **(a)**) result corresponds to the shear layer spectrum where a peak is observed at a St_C value ≈ 18.5, and this resembles the results obtained in literature **[47]**. The spectra of velocity fluctuations at the shear layer that were measured using a hot-wire and the surface pressure fluctuation measured with a surface-embedded mic array by J. Kurelek are shown in Fig. 4.9. The St_C value for the fundamental frequency is 15.6. The range is comparable to the value of 18.5 obtained in the current study. This fundamental frequency potentially corresponds to K-H instability that dominates the disturbances in the shear layer **[47]**. This leads to the formation of coherent structures in the shear flow transition **[49]**.

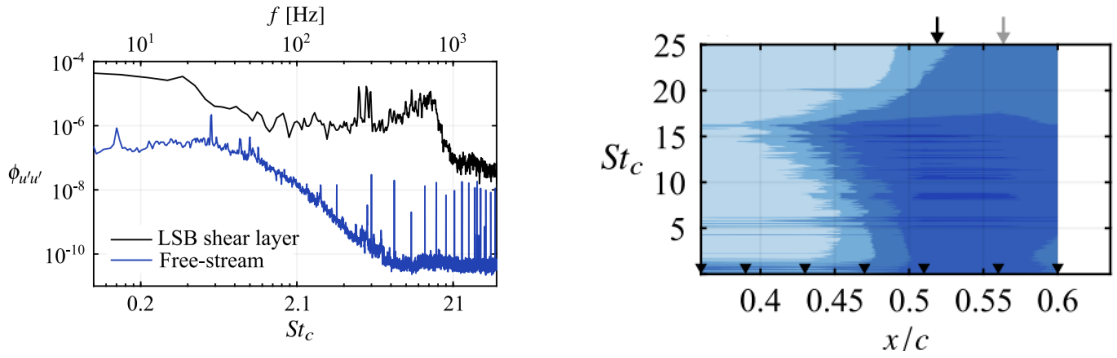

Figure 4.9: (a) Spectra of the velocity fluctuations in the streamwise direction. (b) Spectra of the surface pressure fluctuations **[47]**.

The result from the middle row mic in Fig. 4.8 **(b)**. corresponds to a TBL. This is because the Kapton tape induces an early transition to turbulence in the separation bubble near the middle row of microphones. Additionally, a decrease in the p_{rms} levels is also observed as compared to the upper mic row, as shown in Fig. 4.5. A similar explanation can be made for the lower row of microphones. This spectrum is comparable to the turbulent wake region under the influence of the nacelle wake (see Fig. 4.4.).

To illustrate this, the PSD of Mic 8 (upper row) at $y/R = 0.078$ is shown in Fig. 4.10. This location can also be referred to in the oil-flow image in Fig. 4.4.

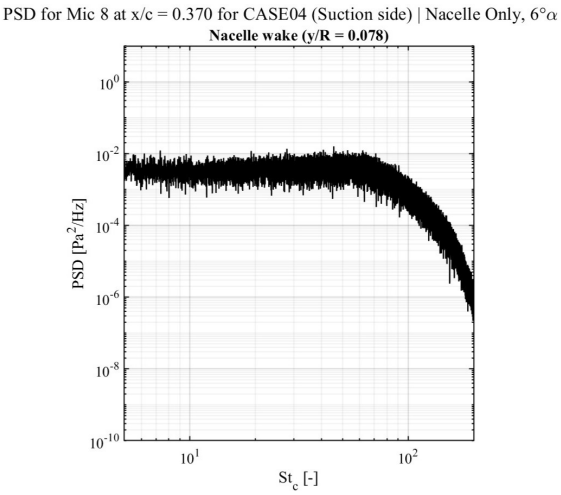

Figure 4.10: PSD for microphone Mic 8 ($y/R = 0.078$) at $x/c = 0.370$ for CASE04 (Suction side). The PSD x-axis is expressed in terms of the chord-based Strouhal number St_C. This spanwise position is located in the region influenced by the nacelle wake and can be referenced in Fig. 4.4 and Fig. 4.5.

In the reattachment region (see Fig. 4.4), the difference between the upper and other rows of microphones decreases as compared to Fig. 4.6. This is shown in Fig. 4.11 where the scale is adjusted for visible comparison with Fig. 4.6. This shows that in regions with lower p_{rms} levels, the difference is negligible. However, at regions with higher p_{rms} levels, such as the LSB influence or inside the propeller slipstream for the propeller-on cases, a significant difference is observed in the response of the three microphone rows.

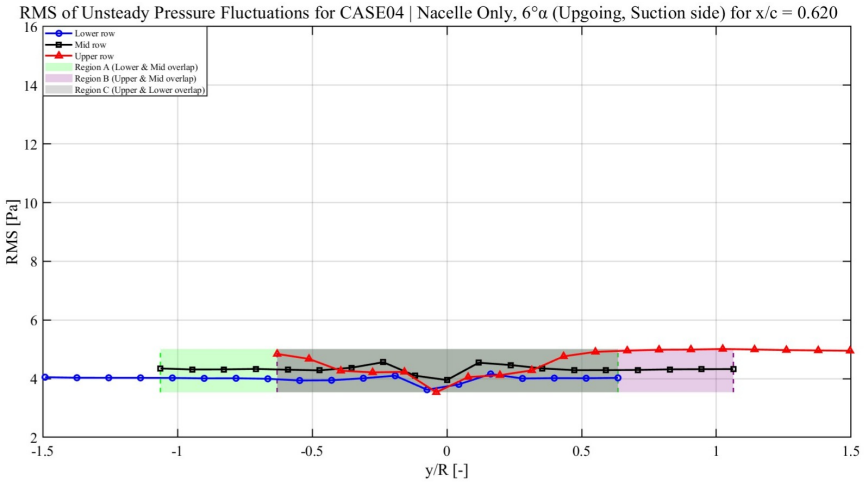

Figure 4.11: p_{rms} plot of the three rows of microphones for CASE04 suction side. The results correspond to the region highlighted in the oil-flow image across different spanwise positions and at $x/c = 0.620$. The shaded overlapping regions (Regions A and B) extend between their respective coloured dashed lines. For Region C, the overlap is defined by the left dashed line of Region B (purple) and the right dashed line of Region A (green), as seen in the figure. The scale is adjusted for visible comparison with Fig. 4.6. **Note:** Although the figure title mentions "Upgoing," this plot includes both upgoing (retreating) and downgoing (advancing) sides for the suction surface.

Based on the PSD results from the region under the influence of the nacelle wake (see Fig. 4.10) and the reattachment region[3], both regions are found to be turbulent. The spectrum at Mic 9 (mid row), located within the separated shear layer, also shows similar characteristics. This indicates that the Kapton tape indeed induces an early transition for the middle row of mics, despite being located in the separated shear layer. This conclusion can also be extended to the lower row of microphones.

Hence, this validation concludes that for further tests using the device, the use of a sleeve is imperative for scaled testing at low Re to ensure that regions of increased local flow velocity are not present due to the protruding pressure sensors, while also ensuring that the mics are not adversely affected. A sleeve would still be required for high Re testing, such as for a flight test; however, that is beyond the scope of this study.

4.3 CASE09 (Nacelle ONLY, 0°α) and CASE04 (Nacelle ONLY, 6°α)

This section provides a brief discussion on the nacelle-only cases for both the suction and pressure sides. Since the experiment is carried out at low Re, the formation of an LSB is observed **[23]**. This is an important phenomenon, as it will affect the flow in the slipstream for propeller-on cases at different α values. The results for the suction side are discussed in the following paragraphs.

The p_{rms} plot for CASE09 and CASE04 is shown in Fig. 4.13. The corresponding oil-flow visualisation images are shown in Fig. 4.12. As the α increases from 0° to 6°, the LSB is observed to shift upstream for the suction side. The interaction of the nacelle wake with the LSB is visible for both cases. This was discussed briefly for CASE04 in Section 4.2 wherein it was observed that the nacelle wake induces a turbulent flow as it interacts with the LSB.

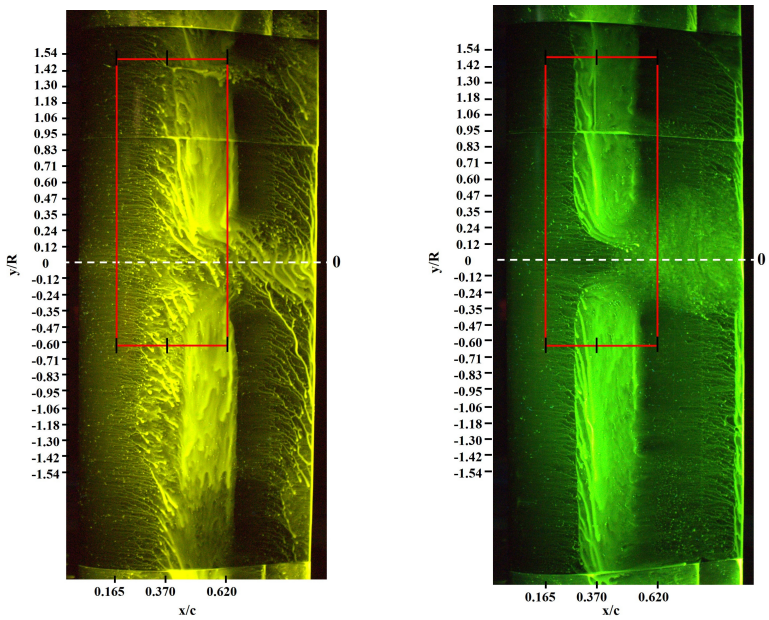

Figure 4.12: (a) CASE09 (nacelle only case at 0°α), (b) CASE04 (nacelle only case at 6°α). Oil-flow visualization for CASE09 and CASE04 (suction side). The red rectangle indicates the region used for p_{rms} analysis.

[3]The PSD for the reattachment region was examined separately and exhibited the expected characteristics typical of turbulence. Hence, the corresponding figure is omitted for brevity, and the discussion is deferred to Section 4.3.

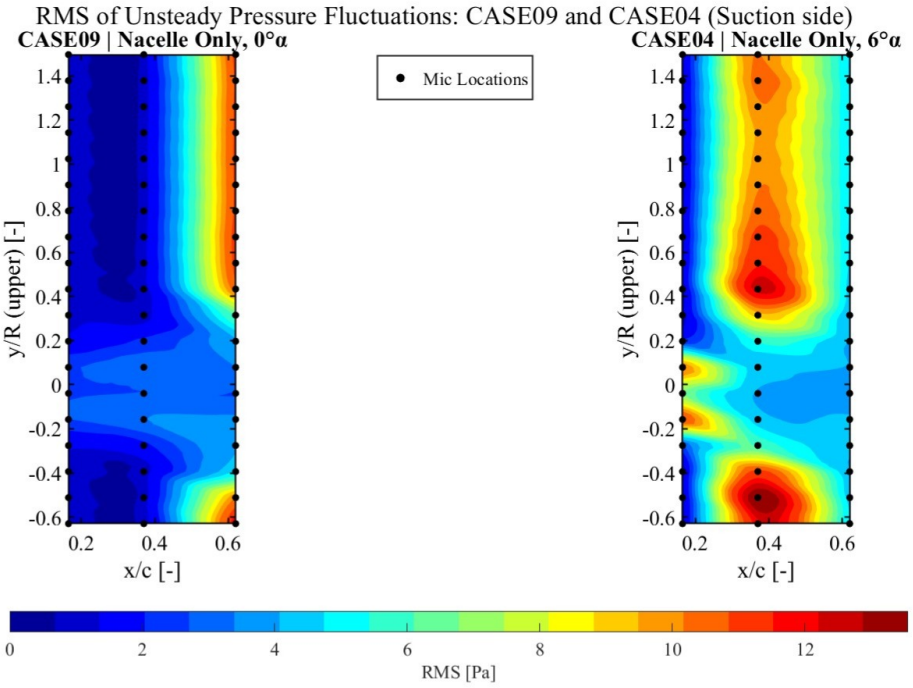

Figure 4.13: RMS of unsteady pressure fluctuations for CASE09 and CASE04 (suction side) for the upper row of microphones.

The upstream shift of the LSB is clearly visible in p_{rms} results shown in Fig. 4.13. The high p_{rms} for both cases corresponds to the separated shear layer of the LSB. The most dominant disturbance in the shear layer is the K-H instability **[47]**. Nieuwstadt et al. (2016) **[50]** state that the K-H instability is related to the base flow and arises from discontinuities in the velocity across a fluid interface. In an LSB, this occurs at a point past the mean separation point of the LBL, where the LBL separates due to natural laminar instability **[47]**. As the α increases, the region of high p_{rms} levels corresponding to the shear layer moves upstream, as seen in Fig. 4.13. The transition to turbulence occurs just ahead of the mean reattachment line of the LSB (see Fig. 4.7). This corresponds to the region of reduced p_{rms} levels at chordwise locations downstream of the separated shear layer as seen for CASE04 in Fig. 4.13. In contrast, the laminar region upstream of the shear layer exhibits even lower p_{rms} levels.

Figures 4.14 and 4.15 show the PSD spectra corresponding to the aforementioned chordwise evolution of the flow on the suction side at a spanwise location of $y/R = 0.91$, highlighting the upstream shift of the LSB as the α increases.

CASE09 (see Fig. 4.14):

1. Mic 6 at $x/c = 0.165$ and Mic 8 at $x/c = 0.370$ are located in the region dominated by laminar flow ahead of the LSB as seen in Fig. 4.14 **(a)** and **(b)**, and the oil-flow results from Fig. 4.12. In the laminar flow region, the pressure fluctuations occur mainly at low frequencies, characterised by a sharp decay in the PSD levels.
2. Fig. 4.14 **(c)** corresponds to Mic 10 at $x/c = 0.620$, which is located in the region influenced by the shear layer of the LSB. The characteristic "hump" of the separated shear layer is visible in the PSD plot. The peak occurs at approximately St_C of 15 and is within the expected range of values corresponding to the dominant disturbances in the shear layer **[47]**.
3. The peaks at high frequencies seem to be present across different flow regions and across all the test cases. They are discussed in Appendix A.7.

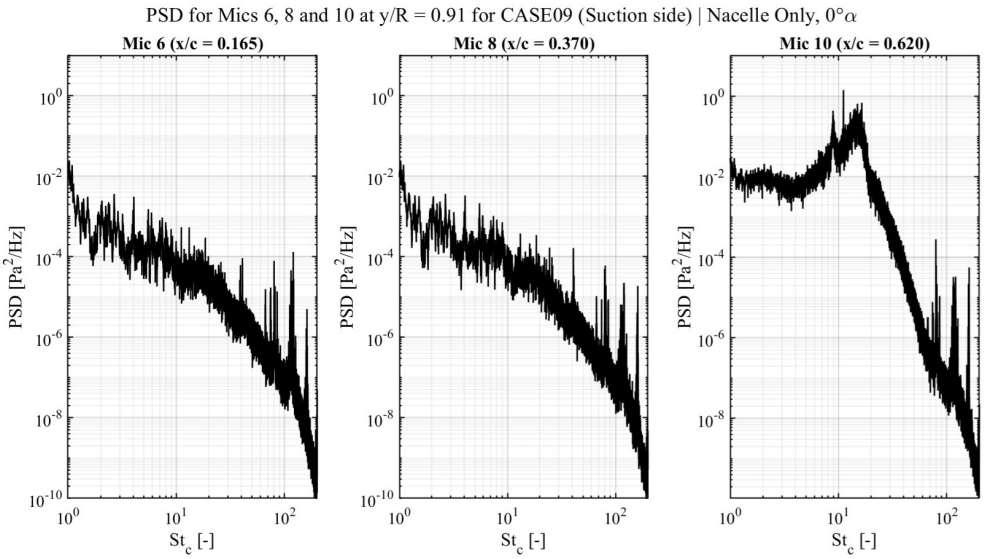

Figure 4.14: PSD for (a) Mic 6 (LBL), (b) Mic 8 (LBL) and (c) Mic 10 (separated shear layer) at $y/R = 0.91$ for CASE09 (Suction side). The PSD is expressed as a function of the chord-based Strouhal number St_C.

CASE04 (see Fig. 4.15):

1. Mic 6 (see Fig. 4.15 **(a)**) corresponds to similar characteristics for CASE09, denoting a region dominated by the LBL.
2. However, the PSD spectra for Mic 8 at $x/c = 0.370$ (see Fig. 4.15 **(b)**) exhibit the characteristic "hump" of the shear layer at $St_C \approx 18.52$ indicating the upstream shift of the LSB and an increase in the fundamental frequency of the K-H instability as the α increases.
3. Mic 10 at $x/c = 0.620$ (see Fig. 4.15 **(c)**) lies downstream of the shear layer of the LSB and is now situated within the TBL. This region can be referred to from Fig. 4.13 and Fig. 4.12. The spectra (see Fig. 4.15 **(c)**) exhibit trends consistent with the expected characteristics of a fully developed TBL **[51] [50]**. A TBL is characterised by chaotic and energetic flow, resulting in elevated PSD levels as compared to the region upstream of the shear layer, across a broad frequency range, followed by decay due to dissipation.

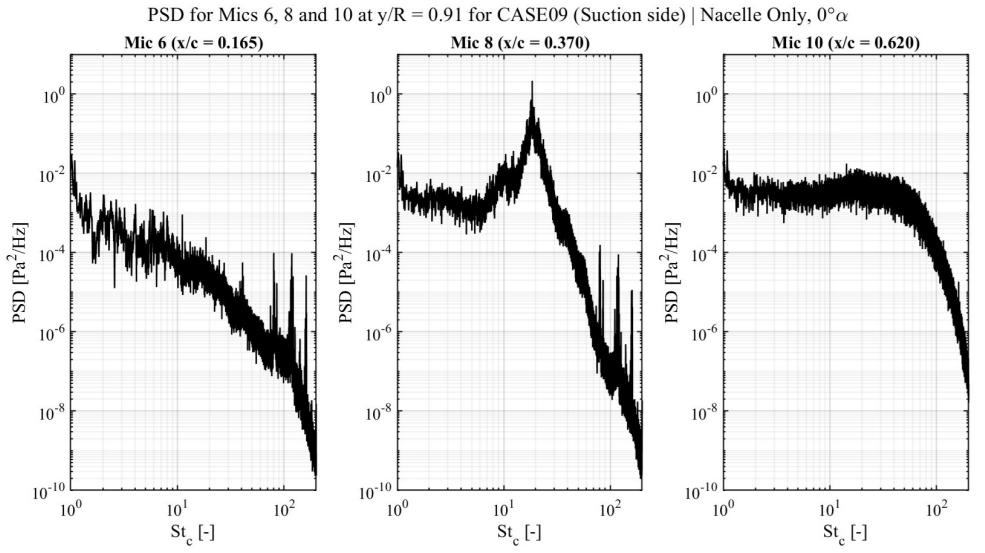

Figure 4.15: PSD for (a) Mic 6 (LBL), (b) Mic 8 (separated shear layer) and (c) Mic 10 (TBL) at $y/R = 0.91$ for CASE04 (Suction side). The PSD is expressed as a function of the chord-based Strouhal number St_C.

On the pressure side for CASE04, the LSB shifts downstream and is beyond the measurement region of the microphones, whereas for CASE09 ($0°\alpha$), the p_{rms} characteristics are similar to those on the suction side, with few discrepancies due to difference in microphone coordinates.

The following sections 4.4 and 4.5 discuss the propeller-on cases and the response of the airfoil immersed in the propeller slipstream. This response is primarily influenced by:

- The aerodynamic loading on the airfoil at different values of α.
- The design and geometric specifications of the airfoil model and the propeller blades.
- The operating conditions, specifically the value of J, which determines the properties of the slipstream. The wind tunnel speed is constant (20 m/s) for all cases.
- The axial distance between the propeller and the airfoil.

4.4 CASE06 ($0.8J$, $30°\beta$ and $0°\alpha$)

This section discusses the propeller-on case of $J = 0.8$. Due to the presence of the slipstream, the LSB is now swept away. The transition induced by the slipstream modifies the dynamics of the transition process within the separated shear layer of the LSB. An LSB occurs at low Re due to the laminar instability that leads to laminar separation, followed by a reattachment of the flow. In such cases, transition to a TBL occurs upstream of the mean reattachment line, driven by the breakdown of vortices into smaller turbulent structures **[47]**.

However, the presence of the slipstream modifies this mechanism, promoting a transition process more characteristic of high Re flows and triggering early onset of transition **[23]** **[21]**.

4.4.1 Suction Side

From Fig. A.5, it can be inferred that at $J = 0.8$, the $30°\beta$ propeller produces a C_T value of 0.27. This is considered a high thrust case for this study. The corresponding propeller speed is 123 rev/s (7380 RPM). However, the efficiency at this operating point is suboptimal.

The radial distribution of sectional thrust on the propeller blade in a positive thrust regime corresponds to a highly loaded tip **[17]**. The magnitude of loading at the tip affects the strength of the tip vortex interaction with the downstream airfoil. In this case, the elevated p_{rms} levels observed near the slipstream edge in Fig. 4.16 suggest strong fluctuations due to the tip vortex as it impinges on the LE of the airfoil and convects downstream along the chord.

In the current study, the microphones closest to the leading edge (on the suction side) are located at $x/c = 0.165$, which is farther away from the tip vortex impingement region; hence, LE phenomena are not a primary focus. To quantify the slipstream interactions downstream on the airfoil surface, the RMS of the pressure fluctuations on the suction side is plotted in Fig. 4.16.

On the retreating blade side, a strong increase in p_{rms} (see Fig. 4.16 **(a)**) is seen inboard of the slipstream edge at $y/R = 0.91$ due to the trace of the tip vortex convecting downstream. The slipstream is displaced in the direction of the centre of rotation of the propeller axis for the retreating blade side. The influence of the tip vortex is strongest at the edge of the slipstream; hence, high values of p_{rms} are observed at the location of the trace of the tip vortex. Furthermore, as explained by S. J. Miley et al. (1987) **[12]** and S. P. Sparks et al. (1983) **[52]**, the axial downwash velocity induced due to the propeller rotation is strongest at the slipstream edge with a decrease in velocity in the region outside the slipstream edge (see Fig. 4.17). Lower p_{rms} levels outside the slipstream edge correspond to this effect. From the oil-flow visualisation image, the trace of the root vortex[4] can also be observed from Fig. 4.16 **(b)**. Furthermore, the pressure fluctuations induced by the nacelle wake can be observed at the region near $y/R = 0$.

[4] To confirm the origin of the root vortex, a nacelle-only test was conducted with the propeller hub rotating but without the blades. In this configuration, no spanwise streak resembling the observed root vortex was observed on the airfoil from the oil-flow visualisation images, thereby ruling out the nacelle as the source. The observed feature is thus attributed to the root vortex generated by the propeller blades.

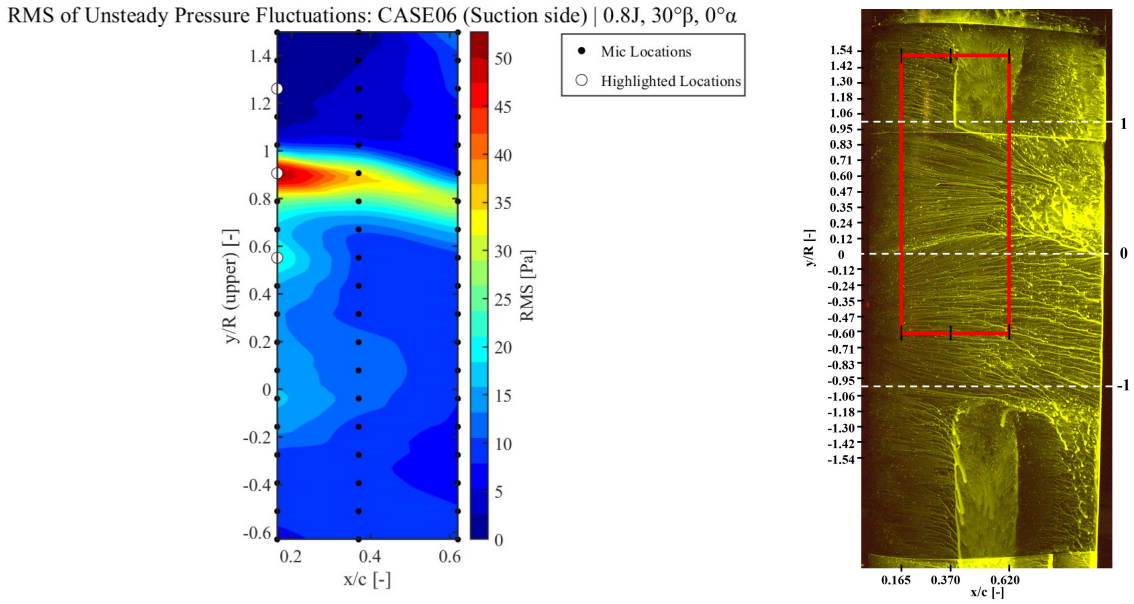

Figure 4.16: (a) RMS of the microphone data on the suction side (upper row of mic data). The points annotated with white circles correspond to the position that would be used for the phase-locked averaging. (b) Oil-flow visualisation for CASE06 suction side. The red rectangle indicates the region spanned by the upper row of microphones. Although the upper row is shown, the y/R axis values correspond to the middle row of microphones (and beyond), as the propeller's spanwise locations were referenced to the mid row. A fixed offset was applied to account for the spanwise separation between rows on the device.

The changes in the airfoil sectional loading at 0°α are caused by the increase in the dynamic pressure (q_∞) inside the slipstream **[21]**. This can be inferred from Fig. 4.17. The spanwise C_p-distribution for CASE06 and CASE09 (nacelle only at 0°α) for the retreating blade side is shown in Fig. 4.18. This shows the increase in the C_p in the presence of a propeller slipstream as compared to the nacelle-only case. CASE06 (solid markers) shows lower C_p values due to propeller-induced effects, while CASE09 (hollow markers) serves as a baseline for comparison in the absence of propeller loading. It is important to note that the airfoil used in this study is the NACA 63_3-018, which is a symmetric airfoil. Therefore, the lift generated at 0°α is expected to be minimal.

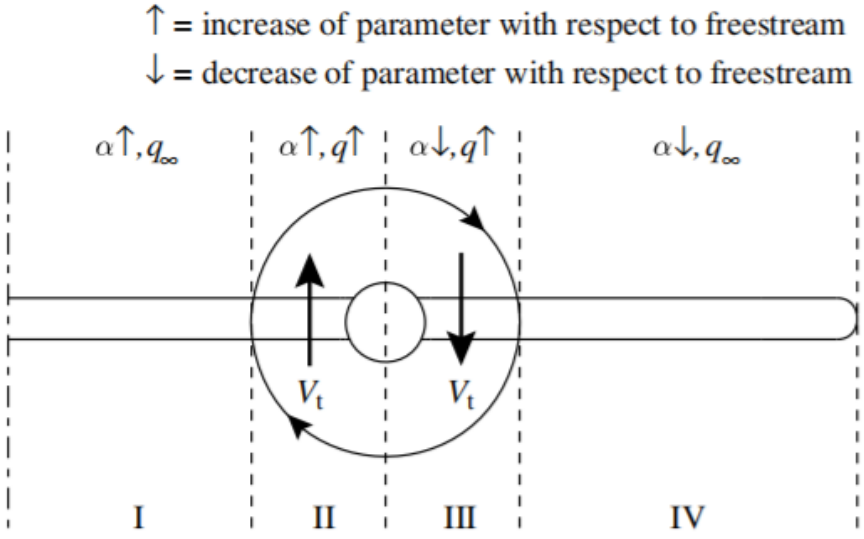

Figure 4.17: Wing-inflow modification due to the propeller for conventional configuration with inboard-up rotation **[53]**.

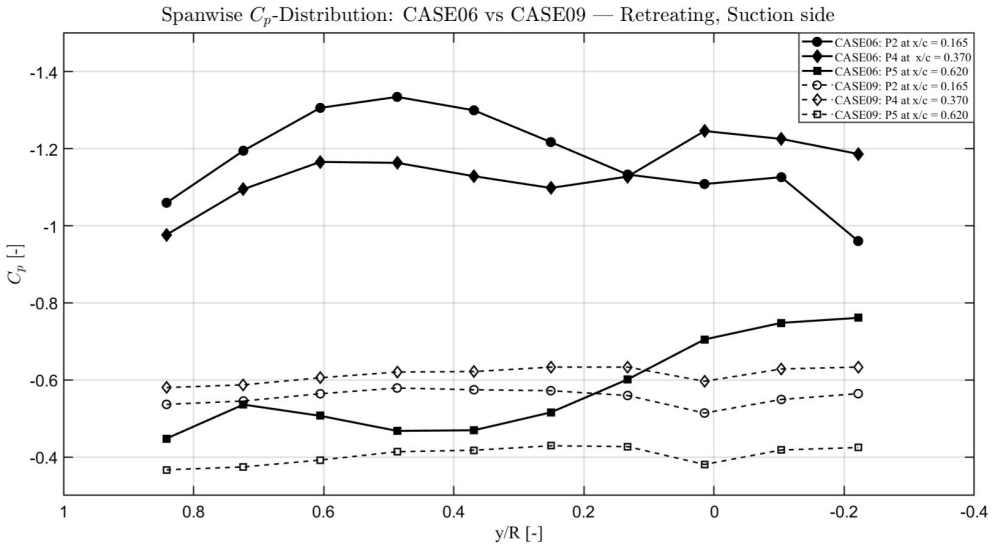

Figure 4.18: Spanwise distribution of surface pressure coefficient (C_p) on the suction side of the airfoil model for CASE06 ($J = 0.8$, 30°β, 0°α) and CASE09 (nacelle-only, 0°α). The results are shown for three chordwise pressure sensor locations ($x/c = 0.165$, 0.370, and 0.620). Each pressure sensor is denoted as 'P' followed by its sensor number.

On the retreating blade side, increased pressure fluctuations are observed inboard of the tip vortex trace in Fig. 4.16 **(a)**. These can be attributed to the interaction between the airfoil boundary layer and the blade wake and the increase in the local effective α in the region of the airfoil surface influenced by the upwash induced by the propeller's rotation. In contrast, an opposite trend occurs on the advancing blade side[5], wherein comparatively lower pressure fluctuations are observed (between y/R = -0.2 to -0.6). This was briefly discussed in Section 1.2 of Chapter 1. p_{rms} distributions indicate that the tip vortex is the dominant source of surface pressure fluctuation on the airfoil. This is in agreement with results and trends from literature **[20]**. Additionally, a region of elevated p_{rms} levels is also observed on the upper right side of the graph in Fig. 4.16 **(a)**. This corresponds to the interaction of the slipstream flow with the separated shear layer of the LSB. This will be discussed in Section 4.5.3. To further investigate the region of high p_{rms} fluctuations, phase-locked averaging (PLA) is performed.

PLA done at the points annotated in Fig. 4.16 **(a)** is shown in Fig. 4.19. In Fig. 4.19, dips at low unsteady C_p values correspond to the low-pressure vortex core convecting chordwise across the airfoil surface. The PLA at y/R = 0.91 corresponds to the location of the highest p_{rms} fluctuation on the retreating blade region. This region is dominated by the trace of the tip vortex, where a periodic pressure response is evident from Fig. 4.19. A similar periodic response is also observed farther inboard for a region immersed in the blade wake. However, the amplitude of the pressure fluctuation in this region is comparatively lower. Outside the slipstream, the surface is primarily subjected to weaker, non-periodic pressure fluctuations. The difference in the dips at low C_p values for each blade is due to a potential misalignment of the pitch angle of each blade or non-uniform blade loading. Strong harmonics at the blade passage frequency (BPF) is observed corresponding to this periodic fluctuations. This can be referred to from Fig. 4.20.

[5] Limited by the spanwise resolution of the upper row of microphones, the tip vortex trace on the suction side advancing blade side is not analysed.

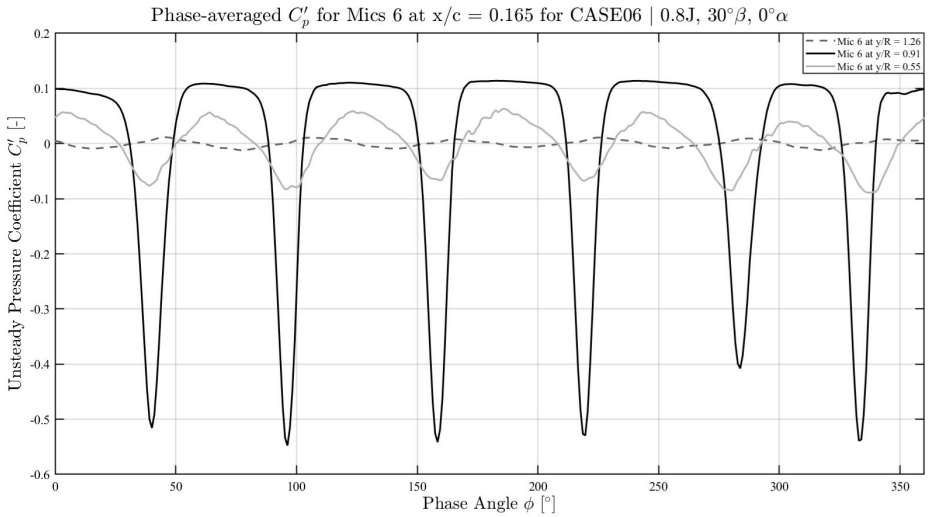

Figure 4.19: Phase-averaged waveforms on the suction side retreating side for Mic 6 at different spanwise positions. The dashed line corresponds to a point outside the propeller slipstream.

The PSD at the locations annotated in Fig. 4.16 **(a)** is plotted in Fig. 4.20 for the suction side retreating blade side. Distinct tonal peaks are observed at the BPF and its harmonics. The periodic pressure response obtained from the PLA corresponds to the tonal component at the BPF. The strength of these peaks diminishes at spanwise positions farther away from the tip vortex trace, where pressure fluctuations are weaker and are characterised by low p_{rms} levels. Additionally, harmonic content near the rotational frequency (RPS) may stem from blade misalignment, non-uniform loading, or structural vibrations of the heavily loaded blades at high RPM. The PSD of the nacelle-only case at 0° α (with the hub rotating at 123 rev/s) showed no peaks at the RPS, ruling out electrical interference or hub-related sources. This is rather related to the aerodynamics of flow structures or structural vibrations.

A difference in the tonal and broadband levels at different spanwise positions is observable. At a position outside the propeller slipstream and ahead of the LSB (see Fig. 4.20**. (a)**), the flow exhibits laminar characteristics and therefore lower broadband levels. The tonal component is still observable. This is due to the viscous mixing of the flows at the propeller slipstream and beyond its boundary. This is further discussed concerning the LSB in Section 4.5.3. The blade wake (see Fig. 4.20**. (c)**) in the inboard section of the propeller blade exhibits comparatively higher broadband levels due to the interaction of the blade wake with the airfoil boundary layer. The PSD at y/R = 0.91, Fig. 4.20 **(b)**, is characterised by the tonal peaks at the BPF and its harmonics, as well as higher broadband levels due to a stronger influence of the tip vortex trace. This is in agreement with the literature **[20]**.

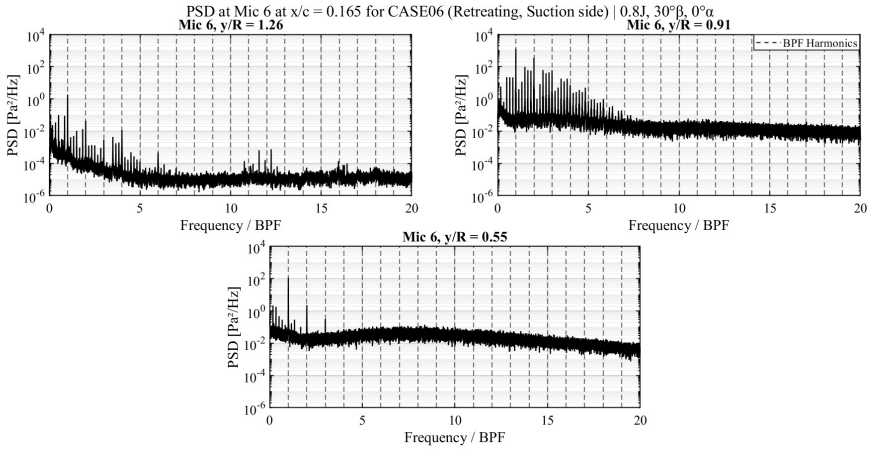

Figure 4.20: PSD of the upper row of microphones on the suction side retreating blade side. (a) Outside the slipstream. (b) At the tip vortex trace. (c) Inboard blade wake region.

4.4.2 Pressure Side

The p_{rms} plot and the oil-flow visualisation image for the pressure side are shown in Fig. 4.21.

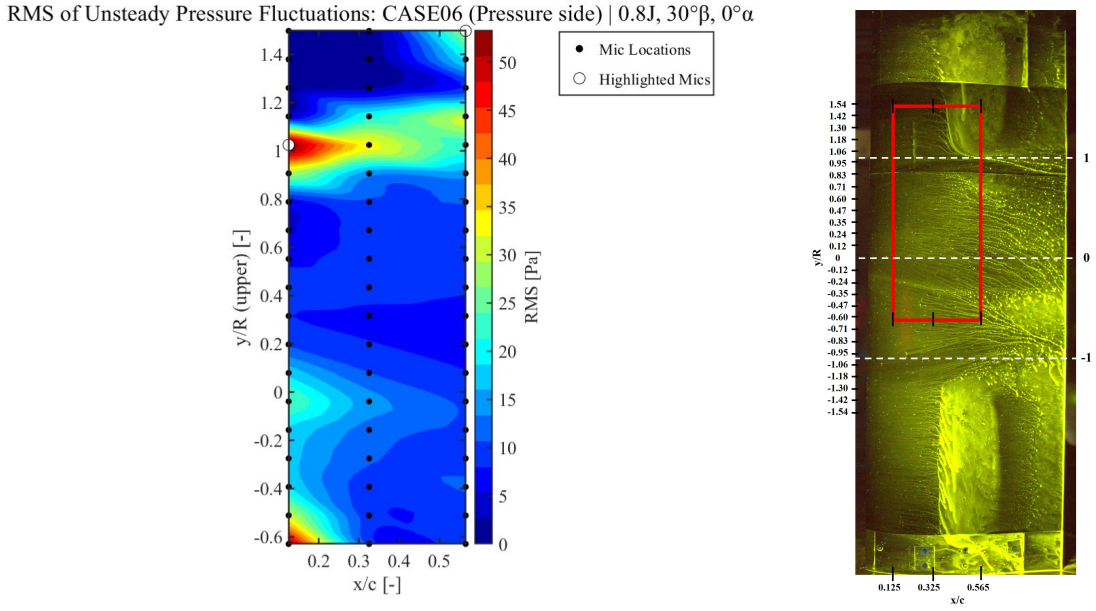

Figure 4.21: (a) p_{rms} of the microphone data on the pressure side advancing blade side (upper row of mic data). The 2 points annotated with white circles corresponds to the position that would be used for the PSD analysis. b) Oil-flow visualisation for CASE06 pressure side. The red rectangle indicates the region spanned by the upper row of microphones. Although the upper row is shown, the y/R axis values correspond to the middle row of microphones (and beyond), as the propeller's spanwise locations were referenced to the mid row. A fixed offset was applied to account for the spanwise separation between rows on the device.

For the pressure side, the trends are expected to be similar to the trends found in the suction side data. This is because the orientation of both the propeller and the airfoil remained unchanged. However, certain discrepancies would arise because, on the pressure side, the microphones and pressure sensors are positioned closer to the LE of the airfoil (the first microphone from the LE is at $x/c = 0.125$), as compared to the suction side case. Additionally, minor deviations in the effective α may occur due to manual alignment errors or lift interference effects within the wind tunnel. However, the discrepancies are not substantial enough to suggest a fundamentally different flow mechanism; it is more likely a result of sensor placement and the corresponding flow structures of that region, which is now comparatively closer to the LE.

For the advancing blade side, the trace of the tip vortex is displaced spanwise away from the propeller rotation axis. As a result, the tip vortex trace is observed at a farther spanwise location compared to the suction side retreating blade side. This trend is in agreement with results from the literature **[20]**. As the tip vortex trace convects downstream along the chord, the amplitude of C_p' corresponding to the low-pressure region of the vortex core decreases (see Fig. A.11). A decrease in the chordwise p_{rms} levels can be observed from Fig. 4.21 **(a)** along the trace of the tip vortex. Furthermore, these fluctuations are also affected by the local skin friction at each microphone location. This leads to a decay in the tonal peaks at the BPF and its harmonics. Furthermore, similar to as discussed in Section 4.4.1, increased p_{rms} values can be observed on the region under the influence of the retreating blade[6] side and inboard of the tip vortex trace (y/R = -0.2 to -0.6). In contrast, on the region influenced by the advancing blade side (y/R = 0.2 to 0.8), comparatively lower p_{rms} values are observed. Similar to the suction side, the root vortex is visible on the pressure side as well (see Fig. 4.16 **(b)**). In both suction and pressure sides, the root vortex is deflected towards the retreating blade side. This is potentially due to the low pressure region corresponding to the retreating blade side[7]. Furthermore, the pressure fluctuations induced by the nacelle wake can be observed at the region near $y/R = 0$. Additionally, a region of elevated RMS levels is also observed on the upper right side of the graph, corresponding to the location of the annotated microphone location in Fig.

[6] Limited by the spanwise resolution of the upper row of microphones, the tip vortex trace on the pressure side retreating blade side is not analysed.

[7] As the α increases to 6° the root vortex is not visible on the pressure side (see Fig. A.10).

4.21 (a). This corresponds to the interaction of the slipstream flow with the separated shear layer of the LSB. This will be discussed in Section 4.5.3.

The location with high p_{rms} values, corresponding to the trace of the tip vortex (see Fig. **4.22 (a)**), exhibits prominent tonal peaks at the BPF and, as noted earlier, at the RPS. In the region outside the slipstream interacting with the LSB (see Fig. **4.22 (b)**), the spectra display the characteristic "hump" associated with the separated shear layer of an LSB. The tonal peaks and elevated broadband levels, when compared to the nacelle-only case, which already exhibits the LSB hump, contribute to the significantly higher p_{rms} values at this location. This suggests that the additional unsteady content introduced by the propeller increases the pressure fluctuations already present due to the LSB leading to the elevated p_{rms} levels.

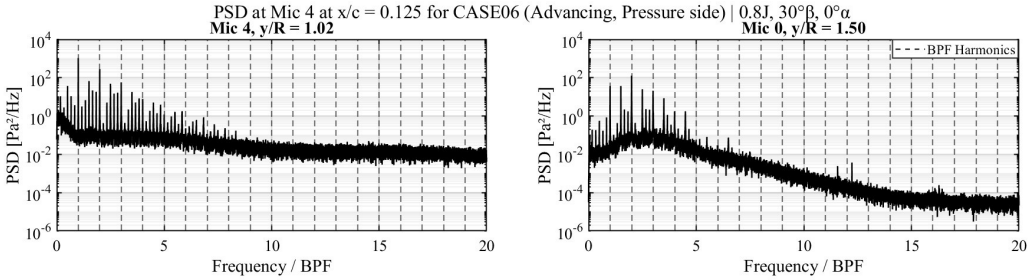

Figure 4.22: PSD of the 2 annotated points for Mic 4 from the p_{rms} plot for the pressure side advancing blade side. (a) At the tip vortex trace. (b) At a spanwise location outside the slipstream, corresponding to a region of high p_{rms} values.

This section presented an analysis of the unsteady surface pressure fluctuations on the airfoil under a positive thrust regime. The results highlighted the dominant influence of the tip vortex, particularly for the highly loaded case, on the surface pressure fluctuations observed on the downstream airfoil model. PSD at key locations helped to interpret relevant flow phenomena, including tonal content at the BPF, broadband turbulent energy, and interactions between the separated shear layer and the propeller slipstream beyond its boundaries.

These findings not only quantify the unsteady pressure behaviour for a positive thrust condition but also align well with trends reported in literature, thereby validating the reliability of the device for investigating the subsequent test cases of this study. Additionally, the results discussed in this section also validates the device for future tests involving propeller slipstream interactions.

4.5 Positive and Negative Thrust Cases at J = 1.8

The positive thrust cases corresponding to the $45°\beta$ propeller are selected for comparative analysis against the negative thrust cases using the $30°\beta$ propeller, as both configurations exhibit their peak efficiency at the same advance ratio of $J = 1.8$ along with an absolute value of thrust coefficient $|C_T| \approx 0.25$ at $J = 1.8$. This can be referred to from Fig. A.5. The rotational speed in these cases is 54.7 RPS (3282 RPM), and the airfoil is tested at $0°$ and $6°\alpha$.

4.5.1 Suction Side

To study the pressure fluctuations for the positive thrust case CASE03 ($1.8J$, $45°\beta$, $6°\alpha$), the p_{rms}[8] and the corresponding oil-flow visualisation[9] are shown in Fig. 4.23.

The region with high fluctuation beyond $y/R = 1$ corresponds to the interaction of the slipstream with the LSB shear layer beyond the slipstream edge. This experiment is conducted at a low Re and hence an LSB is expected, particularly due to the removal of the zigzag trip[10]. This can also be inferred from the corresponding oil-flow visualisation results.

[8] Limited by the spanwise resolution of the upper row of microphones, the tip vortex trace on the suction side advancing blade side is not analysed.

[9] The oil-flow visualization for CASE02 ($1.8J$, $30°\beta$, $6°\alpha$) is discarded due to poor quality, which rendered it unsuitable for analysis.

[10] The trip was placed at the leading edge of the airfoil during the first experiment.

In contrast to CASE06 ($0.8J$, $30°\beta$, $0°\alpha$), a distinct tip vortex trace characterised by elevated p_{rms} levels is not visible in CASE03[11]. Instead, a region of high fluctuations is observed at locations inboard of y/R = 1. This behaviour can be attributed to the low thrust levels[12] generated at the high advance ratio ($J = 1.8$) and low rotational speed (RPM) conditions of CASE03. Under these conditions, the propeller blades are not highly loaded, resulting in a relatively weaker tip vortex and stronger influence from the blade wakes. Higher p_{rms} levels are observed in the inboard region on the retreating blade side as compared to the advancing blade side. This is due to the increase in the local effective α and local V_{eff} on the retreating side as discussed in Section 4.4.1, resulting higher fluctuations compared to the advancing side. This can be referred to from Fig. 4.17 and from the p_{rms} results in Fig. 4.23 **(a)**.

Another indicator of the low momentum in the slipstream for this case is observed in the oil-flow visualisation image. On the retreating blade side, the slipstream sweeps away the LSB. This is attributed to the increase in the local effective α and local V_{eff}. In contrast, on the advancing blade side, unlike the retreating side where the LSB is swept away, the slipstream did not sweep away the LSB. Instead, a delay in the onset of the LSB is observed in Fig. 4.23 **(b)**. This effect was briefly discussed in Section 1.2.

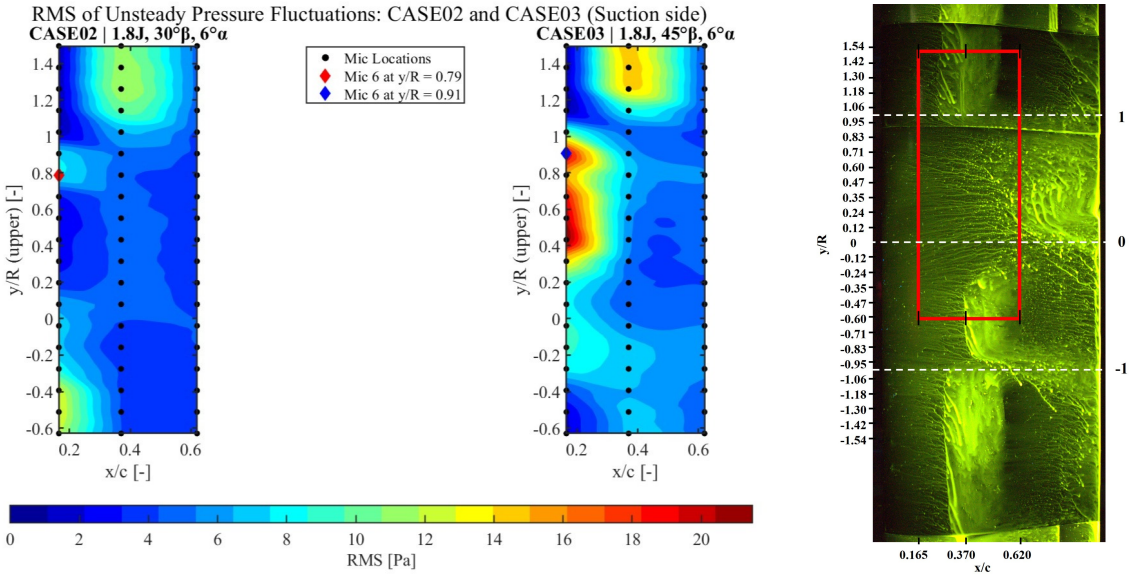

Figure 4.23: (a) p_{rms} of the microphone data on the suction side (upper row of mic data) for CASE03 and CASE02. The annotated point corresponds to the position that would be used for the PSD. (b) Oil-flow visualisation for CASE03 suction side. The red rectangle indicates the region spanned by the upper row of microphones. Although the upper row is shown, the y/R axis values correspond to the middle row of microphones (and beyond), as the propeller's spanwise locations were referenced to the mid row. A fixed offset was applied to account for the spanwise separation between rows on the device.

As the α increases from 0° to 6°, the aerodynamic loading on the airfoil increases. The interaction between the tip vortex core and the airfoil boundary layer leads to higher fluctuations. This interaction appears as elevated p_{rms} levels, particularly inboard of the path of the tip vortex trace. Furthermore, there is a decrease in the magnitude of the low-pressure region in the vortex core (see Fig. 4.24). A decay in the tonal peaks at the BPF is also observed, with an increase in broadband fluctuation levels for a range of low frequencies, as the α increases (see Fig. A.13).

To further investigate the interaction between the tip vortex trace and the increased aerodynamic loading of the airfoil, a comparison is made with CASE08 ($1.8J$, $45°\beta$, $0°\alpha$). At $0°\alpha$, the low-pressure region of the vortex core is localised, while the trend changes as the α increases, where a vortex jitter is expected with increased interactions of the tip vortex core with the airfoil boundary layer. The PLA results used for this comparison correspond to the first spanwise row of microphones, as highlighted in Fig. 4.24 **(a)**.

[11] Unlike the low J cases, the root vortex is not visible on both suction and pressure sides for the high J cases.

[12] The actual thrust levels for CASE03 are lower than those of CASE06. This is because C_T is referenced to n, and the value of n is significantly lower for the $J = 1.8$ cases compared to the $J = 0.8$ cases.

From Fig. 4.24 **(b)** and **(c)**, it can be observed that:

1. At $0°\alpha$, the vortex core is characterised by a periodic and distinct localised low-pressure region. Each localised low-pressure region is followed by a broader high-pressure region due to local pressure recovery. This is in agreement with results from the literature **[54] [18] [20]**.
2. As the α increases to $6°$, the interactions between the vortex core and the airfoil boundary layer increase[13]. This results in a reduction in the magnitude of low pressure in the vortex core. The vortex core at $6°$ exhibits distortions.
3. Increased interactions[14] are now observed in the inboard region, corresponding to the elevated p_{rms} values for CASE03 ($(1.8J,\ 45°\beta,\ 6°\alpha)$) as seen in Fig. 4.23 **(a)**. As discussed, higher pressure fluctuations are observed on the retreating blade side as compared to the advancing side. This effect is enhanced as the airfoil's α is increased. Hence, high p_{rms} values in the region of the blade wake are observed in the retreating blade side. This is illustrated in Fig. 4.23 **(a)** for CASE03.

Additionally, it is important to note that at $6°\alpha$ (as discussed in Section 4.3) the LSB shifts upstream. This is an important result, as the interaction of the LSB with the slipstream, as well as its interaction between successive blade passages, will creep up in the PLA. Phase-locking these effects introduces fluctuations in the averaged signal, with an increasing amplitude at microphones located closer to the LSB region (see Section 4.5.2).

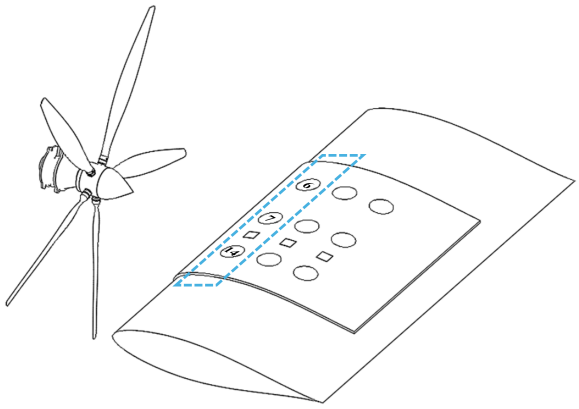

(a) Isometric view of the setup, highlighting mics used for PLA (not to scale)

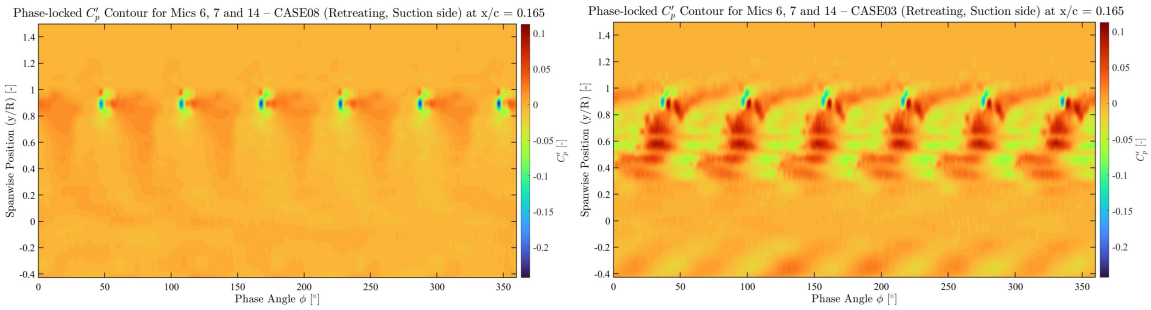

(b) CASE08 ($0°\alpha$)

(c) CASE03 ($6°\alpha$)

Figure 4.24: (a) Illustration of the device layout wrapped around the LE of the airfoil model. The highlighted region indicates the microphones used for PLA contour analysis. The sensor markers are exaggerated for clarity and do not reflect actual dimensions or precise geometry. Circular symbols represent microphones, and square symbols represent pressure sensors, with annotated channel numbers. The propeller depicted here is for illustration purposes only and does not represent the geometry or specifications of the TUD XPROP-S. (b,c) PLA contour for microphones 6, 7 and 14 at $x/c = 0.165$ on the suction side retreating blade side for (b) CASE08, and (c) CASE03.

[13] The horizontal streaks observed between $y/R = 0.4$–1 in Fig. 4.24 **(c)** arise from discrepancies between the middle and lower microphones caused by the Kapton tape. This graph is retained in the analysis, as using only the upper row produced similar trends (with lower resolution and without the streaks). The overall trends remain consistent, and the discrepancy is sufficiently small for reliable comparisons.

[14] The microphones are located farther downstream relative to the initial tip vortex impingement location. As a result, the tip vortex has already undergone significant interactions while convecting before reaching the sensor array.

The PLA results for CASE08 ($1.8J$, $45°\beta$, $0°\alpha$) and CASE07 ($1.8J$, $30°\beta$, $0°\alpha$) are presented in Fig. 4.25. A weaker tip vortex trace is observed in the negative thrust case at $0°$ α. In the positive thrust case (CASE08), periodic pressure fluctuations are observed as localised, with low C_p' values. In contrast, the negative thrust case (CASE07) exhibits C_p' dips that are more broadly distributed across a wider range of phase angles at higher C_p' values. This corresponds to the increased broadband levels for the negative thrust cases with a decay in the tonal peaks at the BPF as compared to the positve thrust cases (see Figures A.14 and A.13).

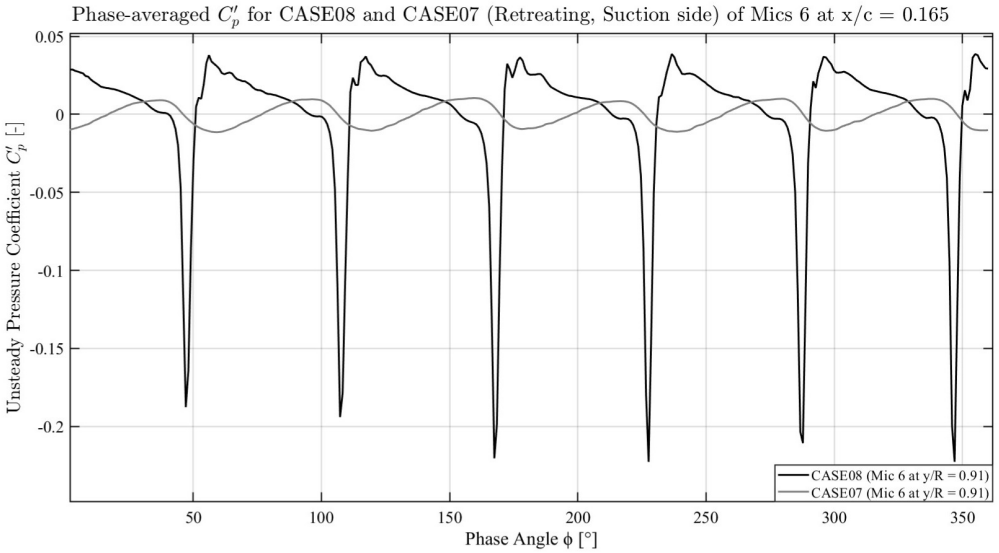

Figure 4.25: Phase-averaged waveforms on the suction side for CASE08 and CASE07 at spanwise positions corresponding to the minimum C_p' values observed along the tip vortex trace.

The p_{rms} for the negative thrust case CASE02 at $6°\alpha$ is shown in Fig. 4.23 **(a)**. It is observed that for the negative thrust case, the pressure fluctuations in the region of the tip vortex trace are lower than those of the positive case. For the positive thrust case, the pressure fluctuations are higher due to a highly loaded blade. The radial sectional thrust distribution for a negative thrust case is different from that of a positive case. In a positive case, the blade is designed such that the outboard section experiences the highest loading. Consequently, the impingement and convection of the tip vortex cause high-pressure fluctuations. However, for the negative thrust case, the outboard or the propeller tips are less negatively loaded or near-zero sectional C_T. The inboard region displays more negatively loaded sections **[26]**, where the blade root regions are under more negative α. Due to the reduced loading near the blade tips in the negative thrust regime, the resulting tip vortex is weaker, resulting in lower pressure fluctuations in its wake. At $0°\alpha$, this weaker tip vortex trace convects at a similar spanwise location as in the positive thrust case, but at $6°\alpha$, it shifts slightly inboard. This shift is potentially due to increased spanwise induced velocities over the airfoil at higher α, as α is the only parameter[15] varied between the two cases. However, it is important to note that direct measurement of blade loading distribution was not feasible in the current study. Therefore, it remains possible that a small positive loading existed near the blade tips for the negative thrust case, as reported in previous studies **[26]** **[25]**.

As discussed in Section 1.3, the reversal of the lift vector and the associated torque also causes a reversal in the direction of swirl imparted to the flow. This can be observed from Fig. 4.23 **(a)** for CASE02, where higher p_{rms} levels are observed in the inboard region on the advancing blade side. Due to the swirl reversal, the advancing blade side now experiences an increase in the local effective α. The trends shown in Fig. 4.17 for a positive thrust case are reversed.

Furthermore, the region of maximum p_{rms} values does not lie in the region of the trace of the tip vortex but in a region beyond the slipstream edge. This is because the p_{rms} levels of the interaction between the slipstream and the LSB shear layer are higher than the p_{rms} levels of the tip vortex trace for the negative thrust case. The slipstream interaction amplifies the already elevated p_{rms} levels of the separated shear layer.

[15] Minimal upstream effect of the airfoil is assumed in the study.

The PSD corresponding to the mic and position[16] where the magnitude of the low C_p region is highest from the phase- averaged waveform, is shown in Fig. 4.26. Tonal peaks at the BPF are observed in the PSD spectra for both cases. However, in CASE02 (negative thrust case at 1.8J), the harmonics of these tonal components decay rapidly as compared to CASE03 (positive thrust case at 1.8J), and the higher-order harmonics become obscured by the elevated broadband levels. This is due to the weaker tip vortex trace. Additionally, this behaviour is closely tied to the distribution of aerodynamic loading on the propeller blades in the two thrust regimes (see Fig. 1.12), wherein for the negative thrust case, inefficient lift generation leads to a reduction in the tonal components [55]. Moreover, negative thrust represents an off-design operating condition, where the propeller encounters complex flow structures and turbulence. These flow conditions correspond to broadband contributions in the PSD, leading to a spectrum dominated by broadband fluctuations for CASE02, as shown in Fig. 4.26 **(a)**. The positive thrust case CASE03 exhibits increased tonal and broadband contributions as compared to the negative thrust case CASE02.

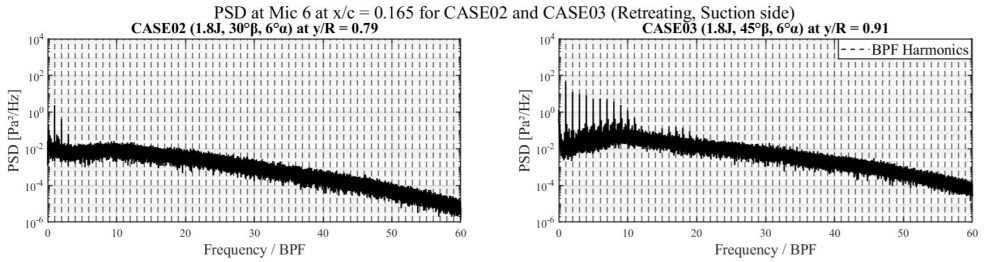

Figure 4.26: The PSD corresponding to the mic and position of the low-pressure region of the trace of the tip vortex for the suction side retreating blade side for (a) CASE02 and (b) CASE03. The location corresponding to the lowest C_p' from the PLA is used for the PSD.

Additionally, the C_p-distribution indicates the effect of reduced q_∞ within the slipstream compared to the region not influenced by the slipstream in the negative thrust regime. To assess the region not under the influence of the slipstream, CASE04 (nacelle-only, 6°α) is used as a baseline. This is shown in Fig. 4.27, which compares the negative thrust case (CASE02) with the nacelle-only configuration (CASE04) at 6°α. The suction on the upper surface is lower for the negative thrust case than the nacelle-only case. This trend is expected, as the propeller slipstream under negative thrust conditions exhibits a reduced dynamic pressure relative to the nacelle-only flow field, particularly for a non-zero α. Additionally, suction on the upper surface for CASE03 (positive thrust case) is higher than CASE02 (negative thrust case), which is also an expected trend (see Fig. A.12).

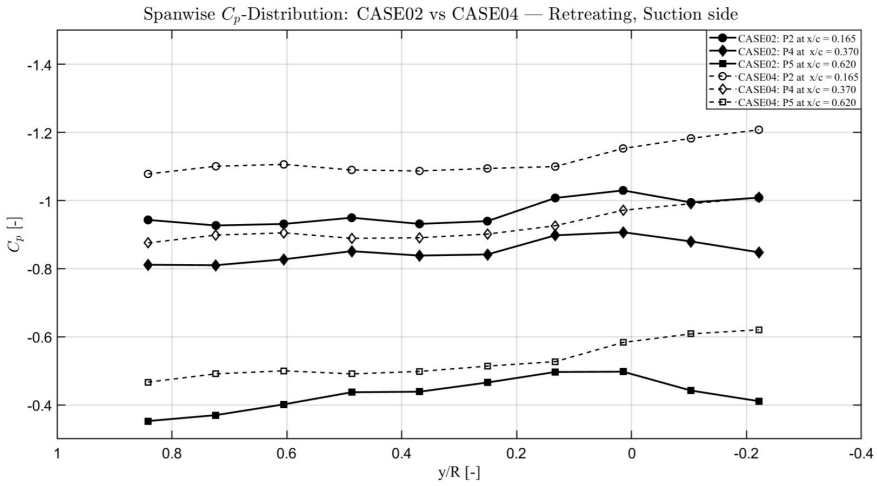

Figure 4.27: Spanwise distribution of surface pressure coefficient (C_p) on the suction side of the airfoil model for CASE02 ($J = 1.8$, 30°β, 6°α) and CASE04 (nacelle-only, 6°α). The results are shown for three chordwise pressure sensor locations ($x/c = 0.165$, 0.370, and 0.620). Each pressure sensor is denoted as 'P' followed by its sensor number.

[16]Multiple microphones and positions were analysed, and the most relevant choice is used for the PSD. The plots used for the selection have been excluded for conciseness.

T. Sinnige et al. (2024) **[56]** found that for a tip-mounted propeller configuration, despite the reduction in q_∞ in a negative thrust case, the overall aerodynamic efficiency was higher than the propeller-off case. The reason was that, despite a decrease in the lift gradient, the reduced friction drag on the wing section inside the slipstream resulted in comparatively higher L/D values than in the propeller-off case. Thus, even though the suction is locally lower, the overall aerodynamic efficiency in the negative thrust configuration may still surpass that of the nacelle-only case.

For the negative thrust cases, increasing the α from $0°$ to $6°$ resulted in elevated broadband levels, primarily due to the increased airfoil loading (see Fig. A.14). This increase in loading also energised the slipstream sufficiently to sweep away the LSB, an effect not observed at $0°\alpha$. The effects of the LSB within the propeller slipstream are elaborated in the next section for the relevant cases.

4.5.2 Slipstream-LSB Interaction Within the Propeller Slipstream

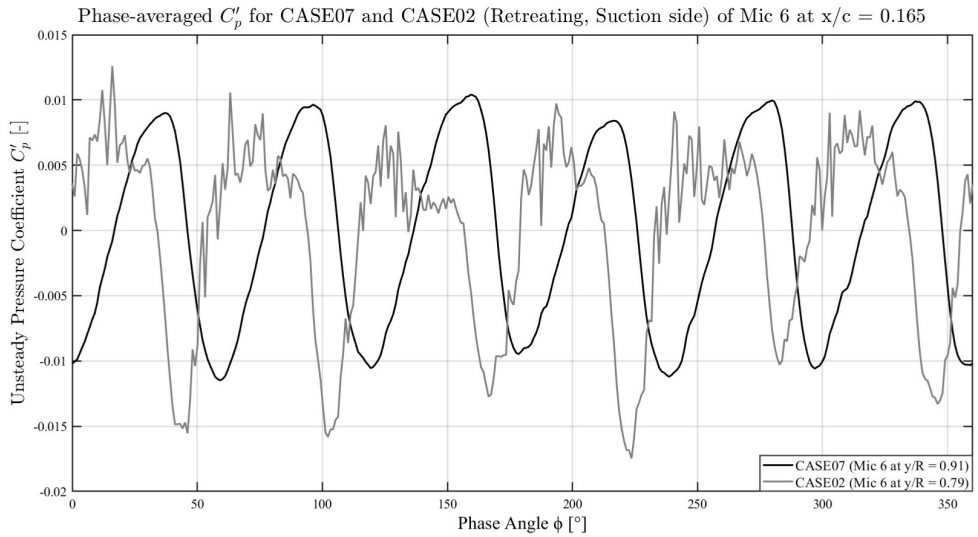

Figure 4.28: Phase-averaged waveform on the suction side retreating blade sides for the two negative thrust cases at Mic 6. The spanwise location corresponding to the lowest C_p' value, identified by evaluating PLA results across multiple spanwise positions, is selected.

From Fig. 4.28, high fluctuations are observed for the phase-averaged results of CASE02 ($1.8J$, $30°\beta$, $6°\alpha$). This is due to two primary reasons: (a) the phase-averaging attempted to phase-lock flow phenomena that do not fluctuate in-phase with the propeller rotation and the BPF, and (b) the number of samples is not sufficient to average out random fluctuations of the LSB[17]. The first reason seems to be the dominant mechanism with the amplification of disturbances closely linked to the behaviour of the LSB with varying α. However, this behaviour is notably more pronounced in the negative thrust case due to the low momentum in the propeller slipstream as compared to the positive thrust case. Irrespective, the trend is similar across all propeller-on cases, with the effects being more pronounced at a higher J value.

At lower advance ratios ($J = 0.8$), this trend is still present, but the amplitude of such fluctuations is lower. This is because, to maintain $J = 0.8$ at a constant tunnel velocity of 20 m/s, the propeller operates at a higher rotational speed (123 RPS), resulting in a higher-momentum slipstream that suppresses LSB-related instabilities more effectively. In contrast, for the $J = 1.8$ cases, where the propeller runs at a lower speed (54.7 RPS) at the same tunnel velocity, the reduced slipstream momentum weakens this suppression, making LSB-related fluctuations more prominent. Among these, the negative thrust case at $J = 1.8$ shows the highest amplitude of these fluctuations as seen for CASE02 ($6°\alpha$), as it experiences even lower slipstream momentum than its positive thrust counterpart.

As seen in Fig. 4.29, Mic 6, which is located in the region of laminar flow, exhibits a smoother phase-averaged result; however, mics located near the LSB shear layer exhibit high fluctuations in the phase-averaged waveform.

[17] The running average and convergence behaviour of different cases can be referred to from Figures A.15, A.16 and A.17.

Furthermore, as the α increases to 6°, the LSB creeps upstream with an increase in the fundamental frequency of the K-H instability (see Section 4.3). Hence, for CASE02, Mic 6 at x/c = 0.165 no longer exhibits a smoother waveform, as seen in Fig. 4.28. This trend is then aggravated for the downstream mics placed near the LSB shear layer. The number of samples for Mic 6 at y/R = 0.91 for CASE07 in Fig. 4.28 is less than the number of samples for the corresponding case for CASE02. However, since the microphone is away from the LSB shear layer, a smoother curve is observed. The issue with the inconsistent number of samples is briefly discussed in Chapter 6.

There is also a possibility of intermittent effects associated with laminar stability, wherein the flow may attempt to revert from turbulent to laminar between successive blade passages. As α increases, the LSB and the associated cyclic transition are expected to shift upstream. The presence and influence of the LSB indicate laminar instability and, consequently, the existence of laminar flow. However, a time-resolved analysis, supported by a time-resolved flow-visualisation technique, is necessary to quantify this intermittent and cyclic transition process more accurately, especially when combined with a case featuring a lower N_B **[9]**. However, such an investigation lies beyond the scope of the present study and is therefore not discussed further.

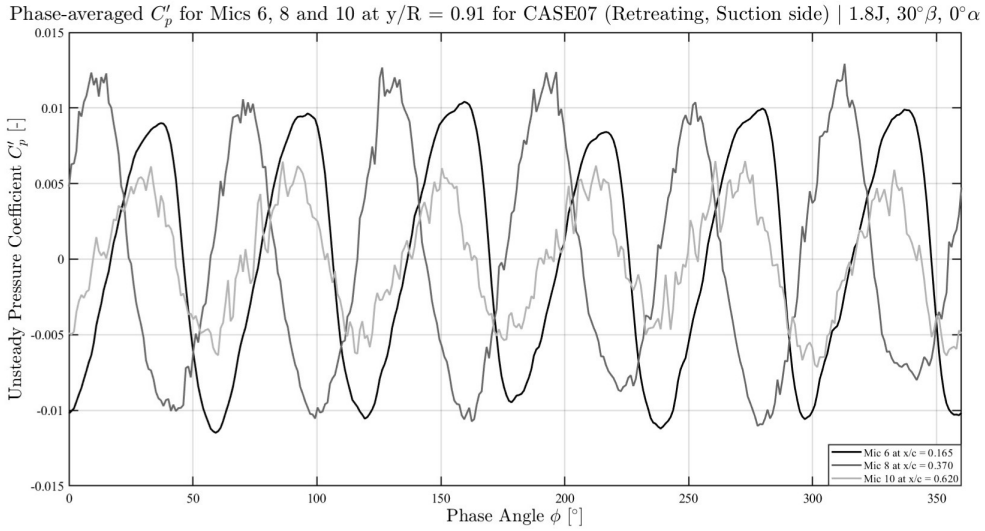

Figure 4.29: Phase-averaged waveform on the suction side retreating blade sides for CASE07 for the chordwise mics at y/R = 0.91.

This effect can also be inferred from the p_{rms} trends for the $1.8J$ cases[18]. The p_{rms} and the oil-flow visualisation results for CASE08 ($45°\beta\ 0°\alpha$) is shown in Fig. 4.30. As can be observed from Fig. 4.30, the propeller slipstream cannot sufficiently suppress and sweep out the LSB. The LSB inside the propeller slipstream can also be observed in the p_{rms} plot from the elevated p_{rms} levels between y/R = 0.4 to 0.8 near x/c = 0.370 on the retreating blade side (y/R conventions can be referred to from Fig. 2.14). On the advancing blade side, at y/R = -0.6 to -0.12 near x/c = 0.6, the elevated p_{rms} levels correspond to the influence of the LSB as from the oil-flow image. A microphone location within these y/R regions has been highlighted in the plot for clarity. Additionally, the trace of the tip vortex is visible at y/R = 0.91 while the nacelle wake is visible[19] near y/R = 0.

This case is particularly important, as the elevated p_{rms} levels, also observed in other $1.8J$ cases, suggest the influence of the LSB and is discussed further in the following sections. However, since oil-flow visualisation captures only the steady-state flow features, it does not always reveal the presence or influence of the LSB as distinctly as in Fig. 4.30. Therefore, the p_{rms} plots of the microphone data will be used for further discussions.

As discussed earlier, an increase in the α leads to a shift of the LSB to a position further upstream, hereby inducing high fluctuations in the PLA data at microphone locations near the LSB region. This region of LSB influence can

[18] Only the region spanned by the upper row of microphones is used for the p_{rms} results due to issues with the data from the middle and lower rows as discussed in earlier sections.

[19] Elevated p_{rms} values are observed beyond $y/R = 1$ and x/c = 0.620, corresponding to the interaction of the slipstream with the LSB outside the slipstream boundary. These values exceed those seen in the 6° cases, possibly due to changes in vortex dynamics with increasing α, wherein a higher percentage of primary vortices break down into smaller scales of turbulence, reducing the observed p_{rms}. However, such high values could also be the result of overshoots in the microphone response, as the measured levels appear unusually high. The vortex dynamics, however, cannot be verified with the current dataset and setup, and is not explored further.

be observed in the p_{rms} plots for CASE03 (45°β, 6°α) and CASE02 (30°β, 6°α), as shown in Fig. 4.31. The corresponding oil-flow visualisation for CASE03 can be referred to from Fig. 4.23.

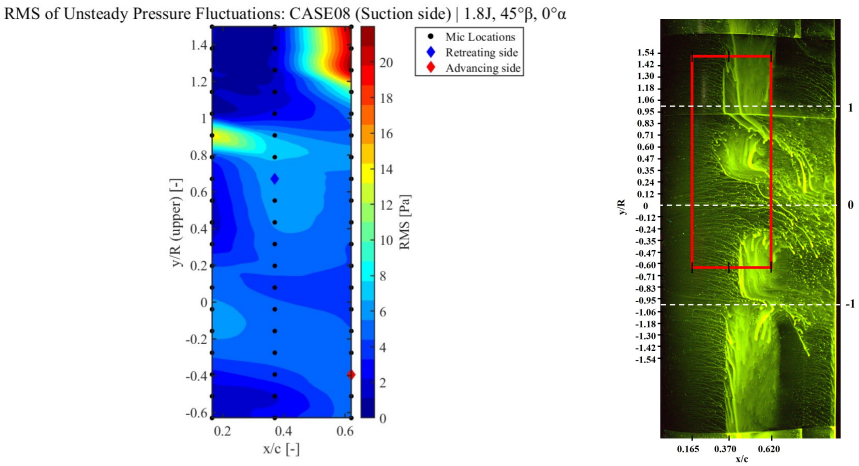

Figure 4.30: (a) p_{rms} of the microphone data on the suction side (upper row of mic data). Annotated points correspond to the region of LSB influence on retreating and advancing sides. (b) Oil-flow visualisation for CASE08 suction side. The red rectangle indicates the region spanned by the upper row of microphones for the p_{rms} plot. Although the upper row is shown, the y/R axis values correspond to the middle row of microphones (and beyond), as the propeller's spanwise locations were referenced to the mid row. A fixed offset was applied to account for the spanwise distance between rows on the device.

It is observed that the influence of the LSB occurs at different regions for the two cases, corresponding to the retreating and advancing blade sides. This is an expected trend, as discussed earlier. In a positive thrust regime, the retreating blade side experiences higher pressure fluctuations and consequently, higher p_{rms} levels. An opposite trend is observed at the advancing blade side, which is more susceptible to the influence of the LSB. In contrast, on the retreating blade side, the LSB is swept away by the higher-momentum flow, as observed in Fig. 4.23.

However, due to swirl reversal, this trend is reversed in the negative thrust case. As a result, the influence of the LSB becomes more pronounced on the retreating blade side, as seen in Fig. 4.31 for CASE02, between y/R = 0.2 - 0.6 (x/c = 0.370), with interactions with the nacelle wake at y/R = 0 and the tip vortex trace at y/R = 0.79. A microphone located within the respective regions of LSB influence for both cases has been highlighted in the plot for clarity.

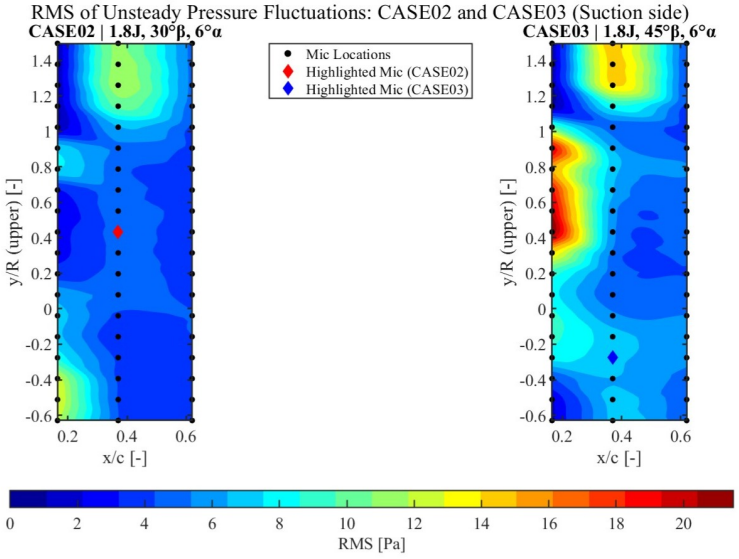

Figure 4.31: p_{rms} of the microphone data on the suction side (upper row of mic data) for CASE03 and CASE02. Annotated points correspond to the region of LSB influence on the corresponding regions for both cases.

Therefore, based on the p_{rms} and PLA results across multiple cases, it is observed that the influence of the LSB within the propeller slipstream becomes more pronounced as the J increases. In contrast, cases at lower J exhibit weaker LSB influence. Moreover, for the high-J cases, the LSB influence is even more significant in the negative thrust regime. This is attributed to the lower momentum in the slipstream for the negative thrust cases, due to a reduced q_∞ as compared to the positive thrust cases.

Furthermore, the effects of the slipstream extend beyond the slipstream edge. This is elaborated in the next section for the relevant cases.

4.5.3 Slipstream-LSB Interaction Beyond the Propeller Slipstream

The p_{rms} plots for CASE03 ($1.8J$, $45°\beta$, $6°\alpha$) and CASE02 ($1.8J$, $30°\beta$, $6°\alpha$), compared against CASE04 (nacelle only, $6°\alpha$) are shown in Fig. 4.32. The p_{rms} of the region corresponding to the LSB outside the propeller slipstream is of primary concern in this section[20] .

As can be observed from Fig. 4.32, there is an increase in the p_{rms} levels for CASE03 as compared to the nacelle only case, beyond $y/R = 1$. A slight increase is also observed for CASE02. Notably, CASE02, representing the negative thrust condition, is characterised predominantly by broadband pressure fluctuations rather than tonal components. This increase can be attributed to the spanwise influence of the propeller slipstream beyond the slipstream edge, as well as the contribution of the tonal and broadband components that, in addition to the shear layer, lead to high p_{rms} levels. The viscous mixing between the flows at the propeller slipstream and the region beyond the slipstream boundary leads to a spanwise influence that extends beyond $y/R = 1$ **[9]** **[52]**.

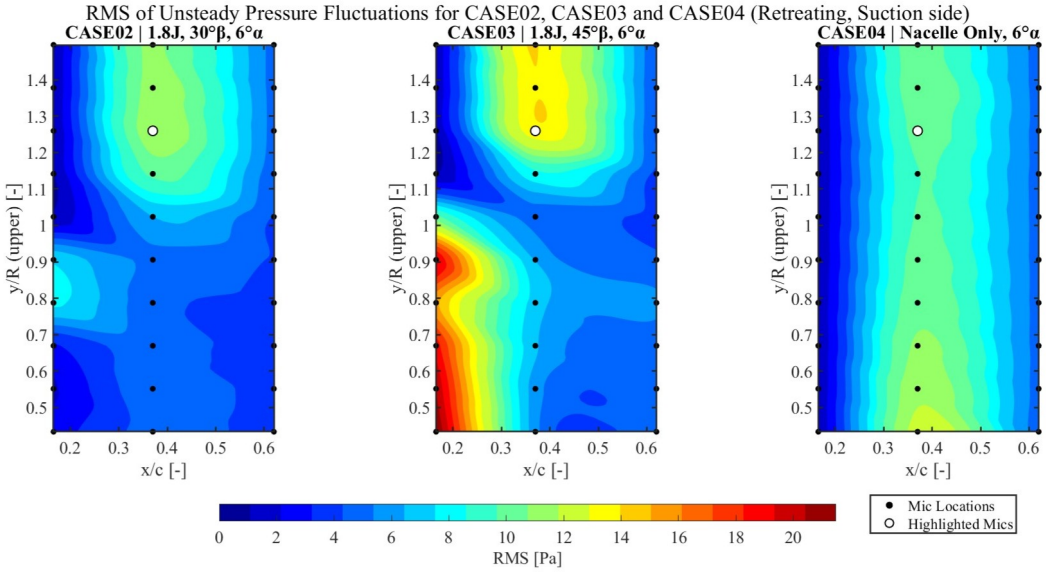

Figure 4.32: RMS of the microphone data on the retreating (upper row of mic data) blade side for the suction side of the airfoil. The subplots correspond to CASE03, CASE02, and CASE04, respectively. The points highlighted with white circles indicate the locations used for the PSD analyses.

The PSD of the aforementioned cases at a spanwise position outside the propeller slipstream is shown in Fig. 4.33. The St_C corresponding to the peak at the dominant disturbance inside the LSB shear layer for CASE04 is 18.5. This corresponds to f/BPF (BPF = 328.2 Hz) $\approx$ 5.64 for the $J = 1.8$ cases[21] and $f/BPF \approx 2.5$ (BPF = 738 Hz) for the $J = 0.8$ cases.

[20] Only the retreating side ($y/R > 0$) is shown because the slipstream edge corresponding to the advancing side (beyond y/R = -1) lies outside the spatial coverage of the upper microphone rows.

[21] Frequencies have been normalized by the blade passing frequency (BPF) of each case to enable consistent comparison across different operating conditions.

As seen from Fig. 4.33 **(a)**, the PSD levels for CASE03 are higher than those for CASE04, with an increase in the broadband levels and additional tonal contributions due to the propeller slipstream. The tonal contributions diminish spanwise as the distance from the slipstream edge increases. Additionally, the characteristic "hump" is not observed at the spanwise location closest to the slipstream edge, likely due to the dominant influence of the slipstream. As the slipstream influence weakens further away, the characteristic "hump" is visible. This trend is also evident in Fig. 4.32 for CASE03, where the elevated p_{rms} levels associated with the shear layer of the LSB are not present at the immediate vicinity of the slipstream edge (near $y/R = 0.91$), but appear slightly farther out ($y/R \approx 1.1$ and beyond). A similar trend is observed for CASE02 in the same figure. However, due to the lower momentum of the slipstream in the negative thrust condition compared to the positive thrust case, the elevated p_{rms} levels associated with the LSB shear layer occur slightly inboard (near $y/R = 0.95$). This is due to weaker influence of the slipstream for the negative thrust case.

From Fig. 4.33 **(b)**, CASE02 exhibits slightly increased broadband levels of PSD (between 10 - 20 f/BPF), along with a distinct tonal contribution due to the slipstream at 1 f/BPF. However, the difference is not significantly high. These trends are consistent with the slight increase in the p_{rms} levels as seen in Fig. 4.32. The primary reason is due to the influence of the propeller slipstream on the LSB shear layer in a region beyond the slipstream boundary **[52] [18]**. The contribution of the tonal components to the LSB shear layer leads to increased PSD levels. This is further enhanced by the increased broadband contributions from the propeller slipstream. As a result, the p_{rms} levels in these regions for the prop-on cases reflect the combined contributions from the LSB shear layer, and the tonal and broadband contributions. The influence of the positive thrust case extends farther beyond the slipstream edge compared to the negative thrust case.

A high-frequency peak at $f/BPF \approx 25$ (approximately 8 kHz) is observed, which corresponds to a harmonic of an upstream tonal peak near 4 kHz (see Section A.7). However, due to elevated broadband levels, this peak at 4 kHz is less distinguishable. Additional harmonics at approximately 12 kHz and 16 kHz are consistently observed across multiple cases and are potentially associated with structural vibrations of the test setup under wind tunnel flow conditions. This is elaborated in Section A.7.

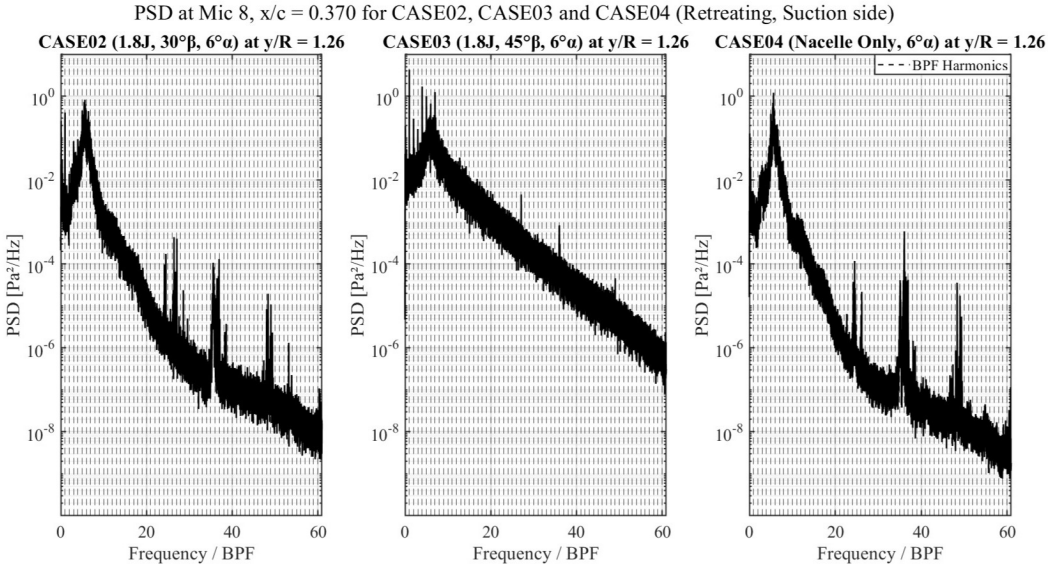

Figure 4.33: PSD of the microphone data on the retreating (upper row of mic data) blade side for the suction side of the airfoil. The subplots correspond to CASE02, CASE03, and CASE04, respectively. Mic 8 ($x/c = 0.370$) at a spanwise position of $y/R = 1.38$ is used for this analysis.

However, at $J = 0.8$, the influence of the slipstream extends across a broader region in the spanwise direction, indicating a stronger influence of the slipstream. The p_{rms} plot for CASE01 ($0.8J$, $30°\beta$, $6°\alpha$) and CASE04 (nacelle only, $6°\alpha$) is shown in Fig. 4.34. As observed from Fig. 4.34, a slight decrease in the p_{rms} values is observed for CASE01 in comparison with CASE04. This is in contrast to the increased p_{rms} trend observed for CASE03 and CASE02 in the vicinity of the slipstream boundary.

Notably, $J = 0.8$ corresponds to a high-RPM case, where a strong slipstream influence on the LSB shear layer is expected. It is also observed that as this influence weakens towards higher y/R values, elevated levels of p_{rms}, similar to those in the nacelle-only case, appear, a trend similar to CASE03 and CASE02 but at farther spanwise positions. This can be referred to from Fig. 4.34 at y/R = 1.50 and x/c = 0.370.

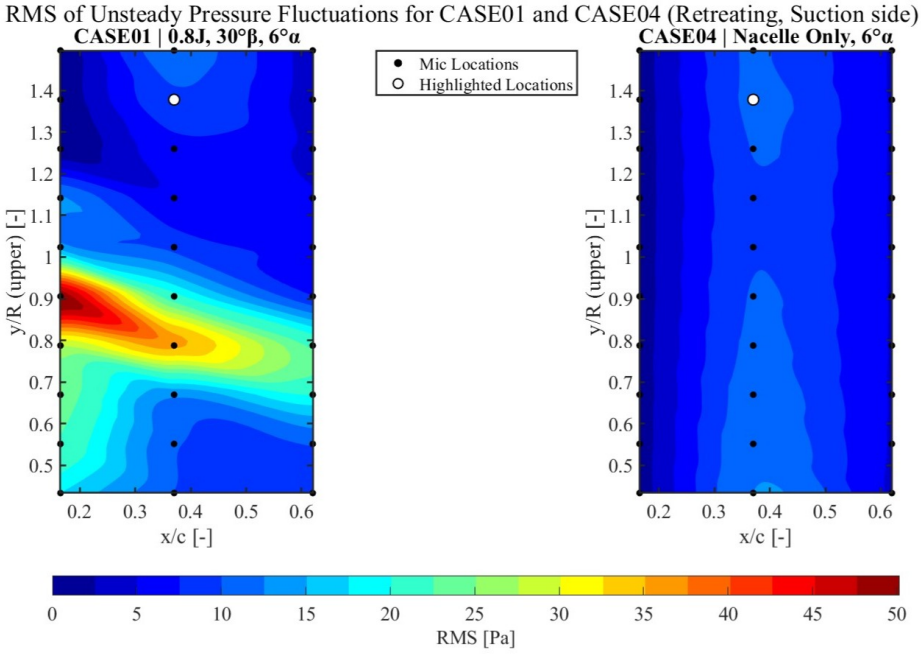

Figure 4.34: p_{rms} of the microphone data on the retreating (upper row of mic data) blade side for the suction side of the airfoil. The subplots correspond to CASE01 and CASE04, respectively. The annotated points indicate the locations used for the PSD analyses.

Fig. 4.35 compares the PSD spectra between CASE01 and CASE04 at a location on the suction side retreating blade side, situated beyond the expected slipstream edge at an even farther point (y/R = 1.38) than the previous cases. The influence of the propeller is still evident at this location, suggesting that the slipstream effects extend farther spanwise than initially expected. The trend observed in Fig. 4.35 is potentially due to the combination of two effects- (a) the extended effect of the propeller slipstream of a lower J value that induces turbulent effects at the shear layer, and (b) the tonal excitation at the fundamental frequency of the dominant disturbance in the separated shear layer due to the harmonics of the propeller RPS. The value at $f/BPF \approx 2.5$ (BPF = 123 Hz) corresponds to St_C = 18.5 for CASE04, where St_C = 18.5 corresponds to the K-H instability in the LSB shear layer.

An increase in both the tonal and broadband components is observed for CASE01, primarily due to the viscous mixing of the propeller slipstream with the flow beyond the slipstream boundary. At this lower value of J, the propeller operates in a heavily loaded regime, generating stronger pressure fluctuations within the slipstream. Consequently, the interaction between the slipstream and the separated shear layer becomes more pronounced. Unlike the high-J cases where the slipstream has a limited or weaker influence, at low J, stronger interactions with the shear layer promote earlier transition to turbulence.

However, despite the observed increase in both tonal and broadband levels, the p_{rms} levels for CASE01 remain lower than those for CASE04 beyon the slipstream edge. One potential reason is that one of the higher harmonics of the propeller RPS (f/BPF = 2.5) (as annotated in Fig. 4.35 **(a)**) aligns closely with the frequency of the dominant disturbance of the LSB separated shear layer. This harmonic effectively acts as an external tonal excitation source[22], potentially promoting early transition **[47] [57]**. This leads to a reduction lower p_{rms} levels at spanwise locations beyond the slipstream edge for CASE01 as compared to CASE04. It is important to note that this trend also includes contributions from the stronger influence of the slipstream in a low J condition. As

[22] It is important to note that in the current study, acoustic forcing was not done deliberately to target the LSB, hence the influence on the mean flow characteristics of the LSB and the vortex dynamics of the natural and forced cases for different excitation frequencies are not discussed further.

explained by J. Kurelek (2021) **[47]**, when the frequency of the excitation matches the frequency of the dominant source of disturbance in the LSB shear layer, the K-H instability, it leads to vortex formation at an upstream location. Furthermore, the momentum needed for the reattachment is comparatively lower at this frequency **[58]**. This promotes an early onset to transition.

For CASE01, both of the discussed effects contribute towards promoting transition, and hence a reduction in p_{rms} is observed as compared to the LSB separated shear layer for CASE04. The relative contribution of the two effects varies with distance from the slipstream edge. Close to the slipstream boundary, the influence of the slipstream-induced turbulence dominates, with little or no presence of the shear layer. As the spanwise distance increases, the slipstream influence weakens and the impact of the shear layer becomes more prominent, often indicated by a characteristic "hump" in the spectra. The second effect is visible at farther spanwise locations. At farther spanwise locations, an increase in the p_{rms} can be seen due to a decrease in both effects. This increased p_{rms} corresponds to the shear layer of the natural LSB. This can be referred to from Fig. 4.34 at y/R = 1.5 and x/c = 0.370. The PSD for the same is shown in Fig. 4.35 **(a)**. However, it is important to note that the individual contributions of both effects are difficult to analyse, particularly for the tonal excitation, in the absence of flow visualisation data capturing the vortex dynamics of the LSB. Irrespective, a decrease in p_{rms} is indeed observed for the low J case in the vicinity of the slipstream boundary as compared to the high J and nacelle only case.

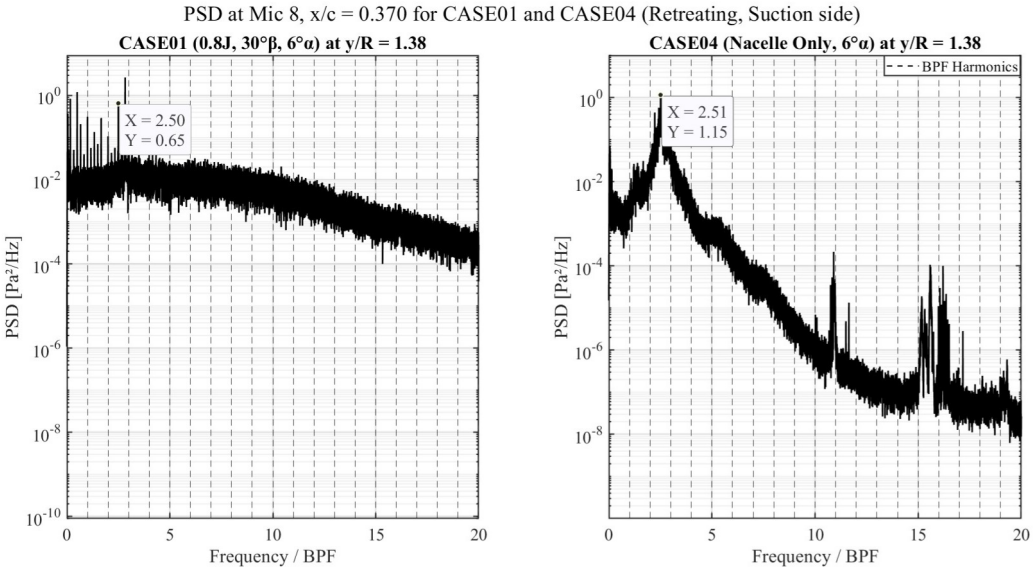

Figure 4.35: (a) CASE01, (b) CASE04. PSD of the microphone data on the retreating (upper row of mics data) blade side for the suction side of the airfoil. The subplots correspond to CASE01 and CASE04, respectively. Mic 8 (x/c = 0.370) at a spanwise position of y/R = 1.38 is used for this analysis. The annotated point in CASE04 indicates the frequency of the most dominant disturbance in the separated shear layer. In CASE01, the annotated peak marks the closest RPS harmonic to this frequency, indicating a possible tonal excitation.

5

Conclusions and Recommendations

This study investigated the unsteady aerodynamic effects of a pusher-propeller operating upstream of an airfoil model, focusing on both positive and negative thrust regimes. A novel measurement device, a flexible PCB embedded with microphones and pressure sensors, was used to quantify unsteady pressure data across multiple spanwise and chordwise locations. This research was motivated by the need to better understand unsteady propeller–wing interactions with a focus on surface pressure fluctuations. In particular, the positive and negative thrust regimes were investigated based on these unsteady surface pressure fluctuations. There is a dearth of literature on unsteady surface pressure fluctuations in the negative thrust regime for open-rotor propellers. A majority of prior studies have focused on time-averaged analyses or qualitative flow visualisations. The study can be extended to wake-interaction effects in the negative thrust regime.

The work was divided into two experimental campaigns:

1. PCB Validation: The initial phase of the campaign involved validating the device, during which both the microphones and pressure sensors were assessed to ensure their responses were consistent with expectations for the given test conditions.
2. Comparative study across thrust regimes: The second phase examined propeller-on cases at various advance ratios, including both positive thrust and negative thrust conditions.
   (a) In positive thrust cases, the presence of a strong, coherent tip vortex trace led to an increase in the pressure fluctuations, with periodic fluctuations corresponding to tonal peaks at the blade passing frequency (BPF) and its harmonics. The p_{rms} levels corresponding to the surface pressure fluctuations decreased as J increased from 0.8 to 1.8, with a further reduction for the negative thrust cases. In the negative thrust cases, the tip vortex was weaker and exhibited lower tonal content with a dominance of broadband fluctuations, along with a strong decay in the tonal harmonics at BPF. Due to the lower freestream dynamic pressure (q_∞) within the propeller slipstream, reduced suction was observed on the wing surface compared to the nacelle-only case, when comparing the spanwise C_p distribution.
   (b) The influence of the LSB within the slipstream was observed to strengthen with increasing J, with the effect being most pronounced in the negative thrust regime.
   (c) The slipstream influence extends well beyond its boundary, affecting unsteady behaviour across the entire span. At low J, the slipstream interacted with the LSB shear layer, triggering earlier transition to turbulence. In contrast, at high J, the combined influence of tonal and broadband components

significantly contributed to elevated p_{rms} levels within the shear layer and across the region beyond the slipstream edge.

A significant insight from the study is that the device works as intended and can be used in the propeller slipstream to quantify surface pressure fluctuations, with some required improvements. The results from the device for the low J case were in agreement with those from the literature.

Three major limitations of the measurement device were identified during the study. Addressing these issues is important not only for improving its performance in future work but also for successfully commissioning the device for experimental campaigns in the future:

1. The protrusion of the pressure sensors and their detrimental effect on the measurement data need to be addressed by designing a sleeve that minimises this height difference while ensuring a flush surface around the microphones.
2. Although the sampling duration was set to 30 seconds during each experiment (from the device's DAQ interface, see Fig. A.4), the device recorded less than 10 seconds of data in most cases, resulting in a mismatch between the intended and actual recording durations. An exception is CASE12 ($9°\alpha$, nacelle-only), where the device successfully recorded approximately 30 seconds of data.
3. The flexible portion of the device imposes limitations when attempting to reposition the device spanwise, and its geometry is not well-suited for capturing flow phenomena near the LE in airfoil test models. These limitations are primarily a result of the device being initially designed for measurements on the Cessna Skymaster, where the spanwise positioning and flow conditions differ significantly from those of an airfoil test section. Thus, the issue appears to stem more from design priorities and application-specific objectives, rather than sensor capability alone.

Recommendations for Future Work

To build upon the findings of this study, future efforts should focus on:

1. Improving sensor integration and surface conformity, possibly with a custom-made sleeve to eliminate reliance on adhesive tapes.
2. Expanding the design to allow higher chordwise resolution and modular spanwise shifting for complete coverage, particularly at the leading and trailing edges.
3. Using synchronised flow visualisation techniques (e.g., Schlieren, PIV) to complement pressure-based observations and identify vortex structures more clearly.
4. Extend the study to wake interaction effects in a distributed propulsion configuration in the negative thrust regime.

While the present study focused on a specific propeller–airfoil configuration, the insights gained apply to a broader range of propulsion–airframe interaction problems. This is largely due to the minimisation of upstream interference and the effective isolation of slipstream effects on the downstream airfoil. The observed pressure fluctuations induced by the slipstream are expected to be relevant for applications such as distributed propulsion systems with wake interference and for operations at low Reynolds number regimes. Furthermore, the use of a flexible surface-mounted measurement device offers a practical framework for capturing unsteady aerodynamic loading in similar experimental settings. With further refinement, this methodology can be extended to more detailed investigations of propeller-wake interactions across different configurations and operating conditions. Additionally, with proper follow-ups and improvements, this off-the-shelf device offers a significant financial advantage for experimental campaigns. Unlike conventional techniques that require drilling holes and installing flush-mounted sensors, which often involve complex fabrication and integration, this device provides a non-intrusive and off-the-shelf alternative that reduces setup time and cost while maintaining high spatial resolution. Finally, the study can be extended to further investigations of unsteady surface pressure fluctuations in the regenerative thrust regime. This is particularly relevant for distributed propulsion systems during descent, where negative thrust operation may influence wake interference effects between adjacent propeller slipstreams.

In conclusion, this work demonstrates the validity of the novel measurement device and its capability to quantify unsteady surface pressure fluctuations in both positive and negative thrust regimes. The device proved to be a valuable tool for capturing propeller–wing interaction effects and holds promise for application in future wind tunnel investigations in low Re conditions.

6

Limitations of the Study

The validation of the device and its usage in the propeller wake-wing interaction investigation yielded interesting and insightful results. However, there are three key limitations of the campaign that need to be addressed.

1. A significant limitation of the second experiment was the issue with the data from the middle and lower rows of microphones. Due to disturbances introduced by the Kapton tape, the signals from these microphones were found to be unreliable and not representative of the actual flow conditions, with discrepancies with respect to the data from the upper row of microphones. As a result, data from these rows had to be discarded, which significantly reduced the spatial coverage of the experiment. This loss of data had consequences: comparisons, such as the spanwise asymmetry between the advancing and retreating blade sides in the negative thrust regime, were limited, with no coverage of the advancing side tip vortex trace. Similarly, a complete spanwise RMS analysis, including both sides of the wing, was not possible, limiting the scope of quantifying the unsteady pressure fluctuations.
2. Although the sampling time for the experiments was 30 secs, the actual recorded sampling time was often below 10 seconds, with inconsistencies observed across multiple test cases. This irregularity in data acquisition posed a significant limitation, as insufficient sampling time compromises statistical convergence.
3. Since a time-resolved flow visualisation was not incorporated in the study, the investigation was unable to fully resolve the impact of the LSB in the negative thrust regime.

Addressing these limitations would improve the fidelity of pressure measurements in future wind tunnel campaigns involving non-uniform inflow or propeller-wing interference using the flexible PCB device.

References

[1] E. W. M. Roosenboom, A. Heider, and A. Schröder. “Investigation of the Propeller Slipstream with Particle Image Velocimetry”. In: *AIAA Journal* 46.2 (2012), pp. 442–449. DOI: 10.2514/1.33917. URL: https://doi.org/10.2514/1.33917.

[2] R. Duivenvoorden et al. “Experimental Investigation of Aerodynamic Interactions of a Wing with Deployed Fowler Flap under Influence of a Propeller Slipstream”. In: *Proceedings of the AIAA Aviation 2022 Forum*. AIAA 2022-3216, Special Session: Aerodynamics and Performance of Integrated Propeller Systems I. American Institute of Aeronautics and Astronautics, 2022. DOI: 10.2514/6.2022-3216. URL: https://doi.org/10.2514/6.2022-3216.

[3] P. Ruchała. “Aerodynamic Interference Between Pusher Propeller Slipstream and an Airframe – Literature Review”. In: *Journal of KONES* (2017). URL: https://www.google.com/url?sa=t&rct=j&q=&esrc=s&source=web&cd=&ved=2ahUKEwj58IiVltOOAxWf9LsIHeHUDXEQFnoECBcQAQ&url=https%3A%2F%2Fyadda.icm.edu.pl%2Fbaztech%2Felement%2Fbwmeta1.element.baztech-47262c08-9597-4dab-896e-b884efdcbf6d%2Fc%2Fruchala_Aerodynamic_Interference_Between.pdf&usg=AOvVaw1LnitVFFFNyPx-wCZA1h_p&opi=89978449.

[4] R. T. Johnston and J. P. Sullivan. “Propeller Tip Vortex Interactions”. In: *28th Aerospace Sciences Meeting*. 1990. DOI: 10.2514/6.1990-437. URL: https://doi.org/10.2514/6.1990-437.

[5] Y. Furusawa and K. Kitamura. “Unsteady Numerical Simulation on Angle-of-Attack Effects of Tractor-Propeller/Wing and Pusher-Propeller/Wing Interactions”. In: *AIAA Scitech 2020 Forum*. 2020, pp. 1–18. DOI: 10.2514/6.2020-1030. URL: https://doi.org/10.2514/6.2020-1030.

[6] L. Veldhuis. “Review of Propeller-Wing Aerodynamic Interference”. In: *Proceedings of ICAS 2004, Paper No. 6.3.1*. Accessed: Dec. 26, 2024. 2004. URL: https://research.tudelft.nl/en/publications/review-of-propeller-wing-aerodynamic-interference-icas-2004-631.

[7] S. Farokhi. “Pressure-Time History of Pylon Wake on a Pusher Propeller in Flight”. In: *AIAA Journal* 6.6 (2012), pp. 758–768. DOI: 10.2514/3.23282. URL: https://doi.org/10.2514/3.23282.

[8] J. Yin, A. Stuermer, and M. Aversano. “Aerodynamic and Aeroacoustic Analysis of Installed Pusher-Propeller Aircraft Configurations”. In: *AIAA Journal* 49.5 (2012), pp. 1423–1433. DOI: 10.2514/1.C031704. URL: https://doi.org/10.2514/1.C031704.

[9] F. M. Catalano. “On the Effects of an Installed Propeller Slipstream on Wing Aerodynamic Characteristics”. In: *Acta Polytechnica* 44.3 (2004). DOI: 10.14311/562. URL: https://doi.org/10.14311/562.

[10] F. Catalano and J. Stollery. “The Effect of a High Thrust Pusher Propeller on the Flow over a Straight Wing”. In: *AIAA 11th Applied Aerodynamics Conference*. 1993. DOI: 10.2514/6.1993-3436. URL: https://doi.org/10.2514/6.1993-3436.

[11] S. Choi and J. Ahn. “A Computational Study on the Aerodynamic Influence of a Pusher Propeller on a MAV”. In: *40th AIAA Fluid Dynamics Conference*. Vol. 1. 2010. DOI: 10.2514/6.2010-4741. URL: https://doi.org/10.2514/6.2010-4741.

[12] S. J. Miley, R. M. Howard, and B. J. Holmes. “Wing Laminar Boundary Layer in the Presence of a Propeller Slipstream”. In: *AIAA Journal* 25.7 (2012), pp. 606–611. DOI: 10.2514/3.45630. URL: https://doi.org/10.2514/3.45630.

[13] R. Howard, S. J. Miley, and B. J. Holmes. “An Investigation of the Effects of the Propeller Slipstream on a Laminar Wing Boundary Layer”. In: *SAE Technical Paper* 850859 (1985). DOI: 10.4271/850859. URL: https://doi.org/10.4271/850859.

[14] T. Sinnige et al. “Pusher-Propeller Installation Effects in Angular Inflow”. In: *22nd AIAA/CEAS Aeroacoustics Conference*. 2016. DOI: 10.2514/6.2016-2875. URL: https://doi.org/10.2514/6.2016-2875.

[15] J. H. Cho. “Experimental and Numerical Investigation of the Power-On Effect for a Propeller-Driven UAV”. In: *Aerospace Science and Technology* 36 (2014), pp. 55–63. DOI: 10.1016/J.AST.2014.04.001. URL: https://doi.org/10.1016/J.AST.2014.04.001.

[16] H. Benyamen, A. McKinnis, and S. Keshmiri. “Effects of Propwash on Horizontal Tail Aerodynamics of Pusher UASs”. In: *IEEE Aerospace Conference Proceedings*. 2020. DOI: 10.1109/AERO47225.2020.9172481. URL: https://doi.org/10.1109/AERO47225.2020.9172481.

[17] N. van Arnhem. “Unconventional Propeller–Airframe Integration for Transport Aircraft Configurations”. Accessed: Jun. 28, 2025. PhD thesis. Delft University of Technology, 2022. ISBN: 978-94-6384-304-1. DOI: 10.4233/uuid:4d47b0db-1e6a-4f38-af95-aafd33c29402.

[18] R. T. Johnston and J. P. Sullivan. “Unsteady Wing Surface Pressures in the Wake of a Propeller”. In: *AIAA Journal* 30.5 (2012), pp. 644–651. DOI: 10.2514/3.46393. URL: https://doi.org/10.2514/3.46393.

[19] D. Witkowski, R. Johnston, and J. Sullivan. “Propeller/Wing Interaction”. In: *27th Aerospace Sciences Meeting*. 1989. DOI: 10.2514/6.1989-535. URL: https://doi.org/10.2514/6.1989-535.

[20] T. Sinnige et al. “Unsteady Pylon Loading Caused by Propeller-Slipstream Impingement for Tip-Mounted Propellers”. In: *AIAA Journal* 55.4 (2018), pp. 1605–1618. DOI: 10.2514/1.C034696. URL: https://doi.org/10.2514/1.C034696.

[21] H. Aminaei, M. Dehghan Manshadi, and A. R. Mostofizadeh. “Experimental Investigation of Propeller Slipstream Effects on the Wing Aerodynamics and Boundary Layer Treatment at Low Reynolds Number”. In: *Proceedings of the Institution of Mechanical Engineers, Part G: Journal of Aerospace Engineering* 233.8 (2018), pp. 3033–3041. DOI: 10.1177/0954410018793703. URL: https://doi.org/10.1177/0954410018793703.

[22] S. Corcione et al. “Experimental Assessment of Aero-Propulsive Effects on a Large Turboprop Aircraft with Rear-Engine Installation”. In: *Aerospace* 10.1 (2023), p. 85. DOI: 10.3390/aerospace10010085. URL: https://doi.org/10.3390/aerospace10010085.

[23] E. A. Elsaadawy and C. P. Britcher. “Experimental Investigation of the Effect of Propeller Slipstream on Boundary Layer Behavior at Low Reynolds Number”. In: *18th Applied Aerodynamics Conference*. 2000. DOI: 10.2514/6.2000-4123. URL: https://doi.org/10.2514/6.2000-4123.

[24] S. Ljunggren, I. Samuelsson, and K. Widig. “Slipstream-Induced Pressure Fluctuations on a Wing Panel”. In: *AIAA Journal* 26.10 (2012), pp. 914–919. DOI: 10.2514/3.45861. URL: https://doi.org/10.2514/3.45861.

[25] R. Nederlof, D. Ragni, and T. Sinnige. “Energy-Harvesting Performance of an Aircraft Propeller”. In: *Journal of Aircraft* 62.2 (2025). Published online: 10 Mar 2025. DOI: 10.2514/1.C038005. URL: https://doi.org/10.2514/1.C038005.

[26] T. Sinnige et al. “Aerodynamic Performance of a Wingtip-Mounted Tractor Propeller Configuration in Windmilling and Energy-Harvesting Conditions”. In: *AIAA Aviation 2019 Forum*. American Institute of Aeronautics and Astronautics. Dallas, Texas, 2019. DOI: 10.2514/6.2019-3033. URL: https://doi.org/10.2514/6.2019-3033.

[27] J. Goyal et al. “Aerodynamic and Aeroacoustic Characteristics of an Isolated Propeller at Positive and Negative Thrust”. In: *AIAA AVIATION 2021 FORUM*. American Institute of Aeronautics and Astronautics. 2021. DOI: 10.2514/6.2021-2187. URL: https://doi.org/10.2514/6.2021-2187.

[28] M. Drela and M. H. Youngren. *XROTOR Download Page*. Retrieved 12 July 2025. 2011.

[29] TU Delft. *Propeller Models – TU Delft*. Accessed: 13 July 2025.

[30] Bosch Sensortec. *BMP390: Digital Pressure Sensor Datasheet*. Accessed: 2025-03-02. 2021. URL: https://www.bosch-sensortec.com/media/boschsensortec/downloads/datasheets/bst-bmp390-ds002.pdf.

[31] SPW0690LM4H-1. *SPW0690LM4H-1 Digital Bottom Port MEMS Microphone: Datasheet (Rev. A)*. Accessed: July 8, 2025. 2024. URL: https://static1.squarespace.com/static/6488b0b8150a045d2d112999/t/674f6bc6538d2a6a09185701/1733258186031/SPW0690LM4H-1_Cameron_Datasheet_RevA-1.pdf.

[32] Technische Universiteit Delft. *Device and method for measuring pressure fluctuations on an aerodynamic surface*. NL Patent NL2036392B1, published March 12, 2024. Accessed July 8, 2025. 2024.

[33] M. Drela. *XFOIL: Subsonic Airfoil Development System*. Accessed: July 12, 2025. 2001.

[34] TU Delft - Faculty of Aerospace Engineering. *M-Tunnel - Low-Speed Wind Tunnels*. Accessed: 2025-03-02. 2025. URL: https://www.tudelft.nl/lr/organisatie/afdelingen/flow-physics-and-technology/facilities/low-speed-wind-tunnels/m-tunnel.

[35] J. G. Herriot. *Blockage corrections for three-dimensional-flow closed-throat wind tunnels, with consideration of the effect of compressibility*. Tech. rep. NACA-RM-A7B28. Research Memorandum, Langley Aeronautical Laboratory. National Advisory Committee for Aeronautics (NACA), 1947. URL: https://ntrs.nasa.gov/api/citations/19930093811/downloads/19930093811.pdf.

[36] S. Luesutthiviboon et al. "Aeroacoustic Benchmarking of Trailing Edge Noise from NACA 633–018 Airfoil with Trailing□Edge Serrations". In: *AIAA Journal* 61.1 (2023), pp. 329–354. DOI: 10.2514/1.J061630.

[37] Airfoil Tools. *NACA 633-018 Airfoil Data*. Accessed: 2025-03-02. 2025. URL: http://airfoiltools.com/airfoil/details?airfoil=naca633018-il.

[38] R. de Vries et al. "Aerodynamic Interaction Between Propellers of a Distributed-Propulsion System in Forward Flight". In: *Aerospace Science and Technology* 118 (2021), p. 107009. DOI: 10.1016/j.ast.2021.107009. URL: https://doi.org/10.1016/j.ast.2021.107009.

[39] N. van Arnhem et al. "Engineering Method to Estimate the Blade Loading of Propellers in Nonuniform Flow". In: *AIAA Journal* 58.12 (2020), pp. 5245–5257. DOI: 10.2514/1.J059485. URL: https://doi.org/10.2514/1.J059485.

[40] D. L. Loving and S. Katzoff. *NASA- MEMO-3-17-59L*. NASA Memorandum NASA-MEMO-3-17-59L. Work of the U.S. Gov. Public Use Permitted. Hampton, VA, United States: NASA Langley Research Center, 1959. URL: https://ntrs.nasa.gov/citations/19980228035.

[41] M. E. Goldstein. *Aeroacoustics*. Illustrated. Advanced Book Program. McGraw-Hill International Book Company, 1976. ISBN: 0070236852, 9780070236851.

[42] MathWorks. *pwelch - Power Spectral Density Estimate Using Welch's Method*. https://nl.mathworks.com/help/signal/ref/pwelch.html. The MathWorks, Inc. 2024.

[43] N. D. Katopodes. "Chapter 5 - Viscous Fluid Flow". In: *Free-Surface Flow: Environmental Fluid Mechanics*. Butterworth-Heinemann, 2019, pp. 324–426. DOI: 10.1016/B978-0-12-815489-2.00005-8. URL: https://doi.org/10.1016/B978-0-12-815489-2.00005-8.

[44] Y. Liu, J. Liu, and F. P. Gao. "Strouhal number for boundary shear flow past a circular cylinder in the subcritical flow regime". In: *Ocean Engineering* 269 (2023), p. 113574. DOI: 10.1016/J.OCEANENG.2022.113574. URL: https://doi.org/10.1016/J.OCEANENG.2022.113574.

[45] ScienceDirect. *Strouhal Number - Engineering Topic*. Accessed: March 3, 2025. 2023. URL: https://www.sciencedirect.com/topics/engineering/strouhal-number.

[46] J. D. Anderson. *Fundamentals of Aerodynamics*. 5th. [Online]. Available: http://www.worldcat.org/isbn/9780073398105. McGraw-Hill, 2011. ISBN: 9780073398105.

[47] J. W. Kurelek. "The Vortex Dynamics of Laminar Separation Bubbles". Accessed: Jun. 15, 2025. PhD thesis. University of Waterloo, 2021. URL: http://hdl.handle.net/10012/16667.

[48] Y. Zhou and Z. Wang. "Effect of Surface Roughness on Laminar Separation Bubble over a Wing at a Low-Reynolds Number". In: *49th AIAA Aerospace Sciences Meeting including the New Horizons Forum and Aerospace Exposition*. 2011. DOI: 10.2514/6.2011-736. URL: https://doi.org/10.2514/6.2011-736.

[49] C. M. Ho and P. Huerre. "Perturbed Free Shear Layers". In: *Annual Review of Fluid Mechanics* 16.1 (1984), pp. 365–422. DOI: 10.1146/annurev.fl.16.010184.002053. URL: https://doi.org/10.1146/annurev.fl.16.010184.002053.

[50] F. T. M. Nieuwstadt, B. J. Boersma, and Jerry Westerweel. *Turbulence: Introduction to Theory and Applications of Turbulent Flows*. Cham, Switzerland: Springer, 2016. ISBN: 978-3-319-31597-3. DOI: 10.1007/978-3-319-31599-7.

[51] S. B. Pope. *Turbulent Flows*. Cambridge: Cambridge University Press, 2000.

[52] S. P. Sparks and S. J. Miley. *Development of a Propeller Afterbody Analysis with Contracting Slipstream*. Tech. rep. 830743. SAE Technical Papers, 1983. DOI: 10.4271/830743.

[53] T. Sinnige et al. "Wingtip-Mounted Propellers: Aerodynamic Analysis of Interaction Effects and Comparison with Conventional Layout". In: *Journal of Aircraft* 56.1 (2019), pp. 295–312. DOI: 10.2514/1.C034978.

[54] J. H. Dittmar and D. G. Hall. *The Effect of Swirl Recovery Vanes on the Cruise Noise of an Advanced Propeller*. NASA Technical Memorandum NASA-TM-103625. AIAA-90-3932. Cleveland, Ohio: NASA Lewis Research Center, 1990.

[55] P. Candeloro et al. "An Experimental Study of the Aeroacoustic Properties of a Propeller in Energy Harvesting Configuration". In: *Fluids* 7.7 (2022), p. 217. DOI: 10.3390/fluids7070217. URL: https://doi.org/10.3390/fluids7070217.

[56] T. Sinnige and B. Della Corte. "Aerodynamic Performance of a Tip-Mounted Propeller-Wing System at Positive and Negative Thrust". In: *AIAA Aviation Forum and ASCEND*. 2024. DOI: 10.2514/6.2024-3520.

[57] K. B. Zaman and D. McKinzie. "Control of Laminar Separation over Airfoils by Acoustic Excitation". In: *27th Aerospace Sciences Meeting*. 1989. DOI: 10.2514/6.1989-565.

[58] M. Nishioka, M. Asai, and S. Yoshida. "Control of Flow Separation by Acoustic Excitation". In: *AIAA 2nd Shear Flow Conference*. 1989. DOI: 10.2514/6.1989-973.

A

Appendix

A.1 Control and DAQ Interfaces

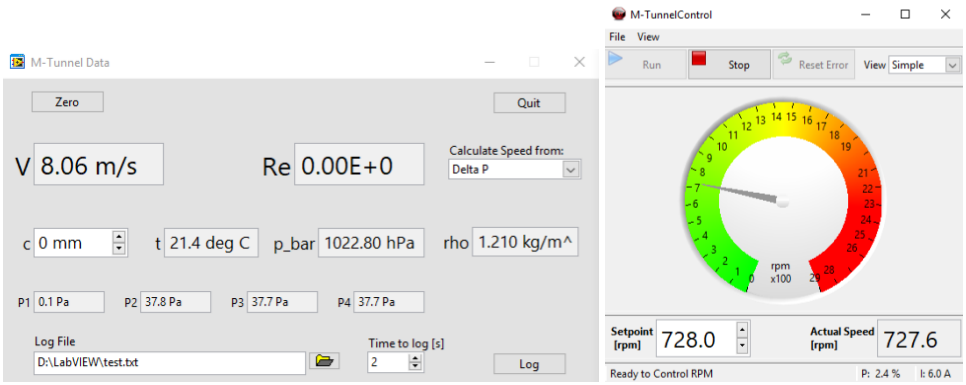

Figure A.1: (a) M-Tunnel Data interface window, (b) M-Tunnel Control interface window

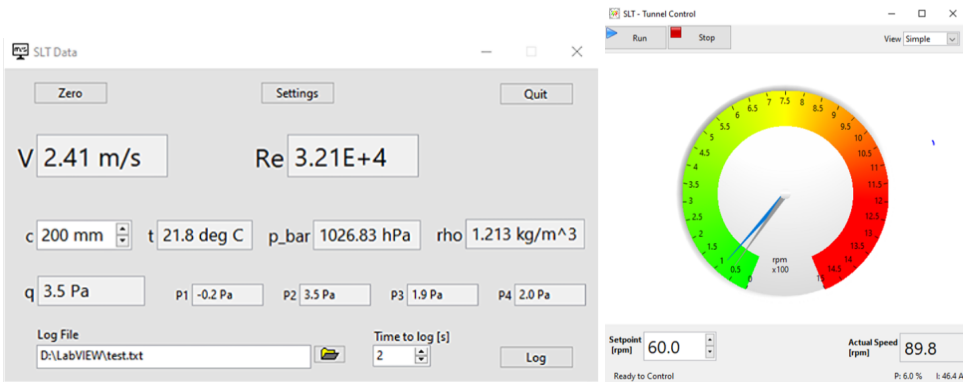

Figure A.2: (a) SLT Data interface window, (b) SLT Control interface window

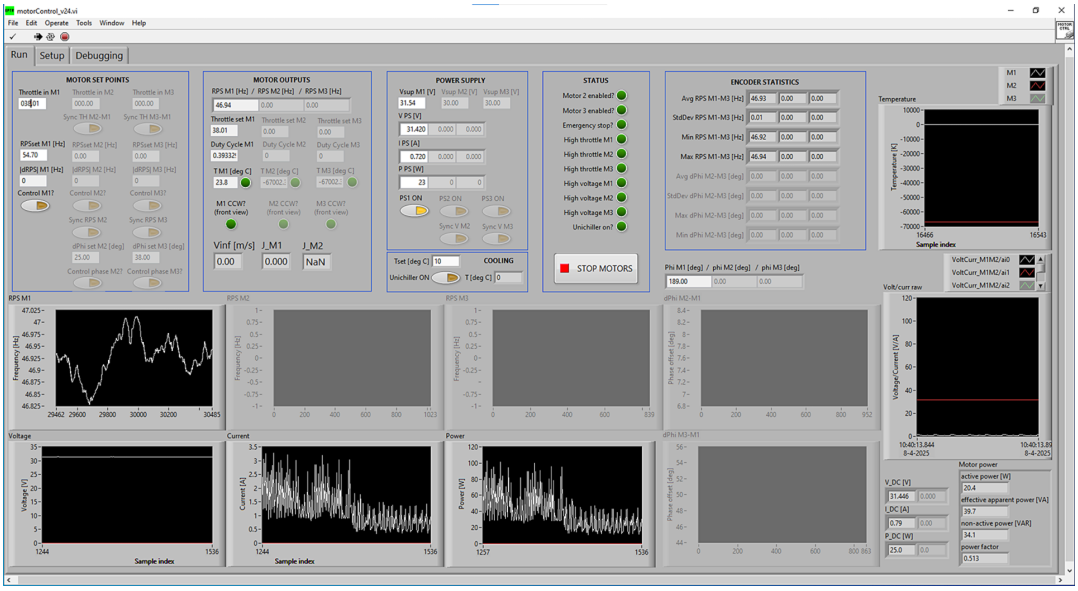

Figure A.3: Motor Control interface window used during the second experiment.

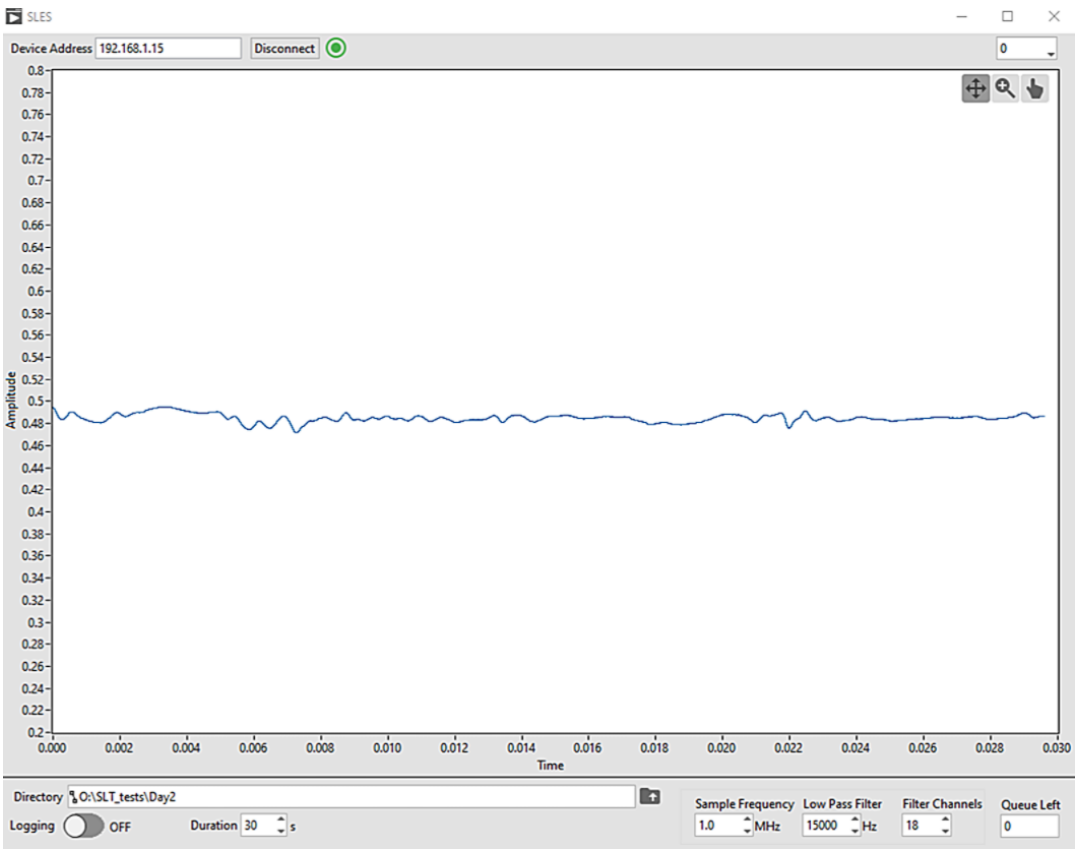

Figure A.4: SES DAQ interface.

The number of channels can be selected by entering the value in the Filter Channels tab. The Logging toggle can be used to start logging the data. The Connect/Disconnect button (highlighted green) is used to connect to the device. Furthermore, a dropdown menu located at the top-right corner (currently at Mic 0) allows the user to toggle between different microphones to monitor their respective data in the graph. The graph in Fig. A.4 shows the amplitude variation over time for the selected microphone channel. The sampling time is set at 30 seconds.

A.2 TUD-XPROP (Ø406.4 mm): Propeller Performance

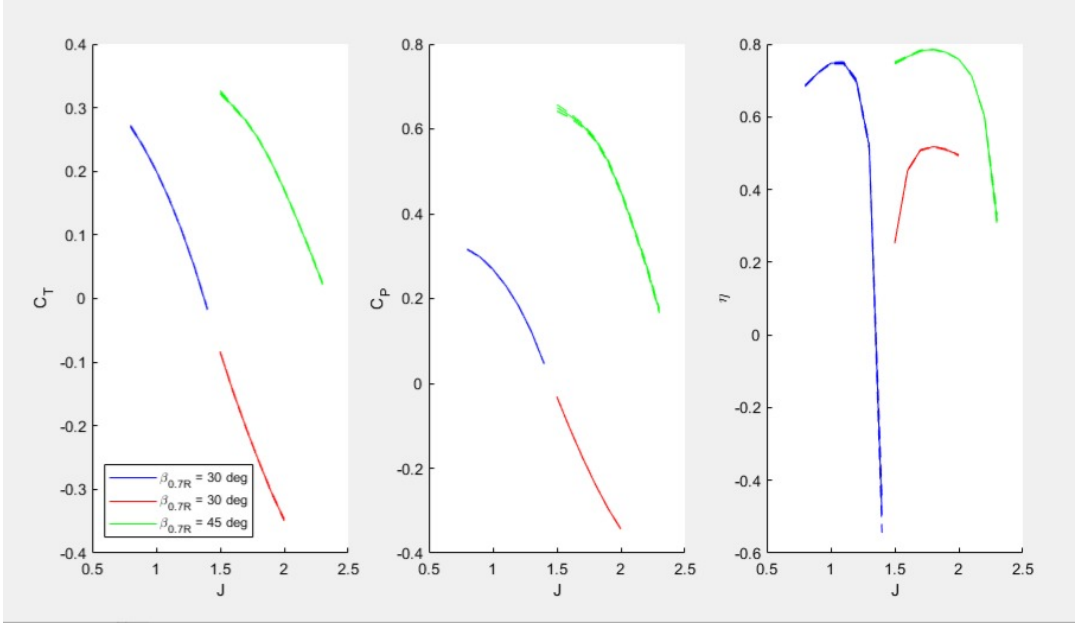

Figure A.5: Performance data for TUD-XPROP (Ø406.4 mm) propeller.

A.3 Calibrated Results of the 18 Microphones

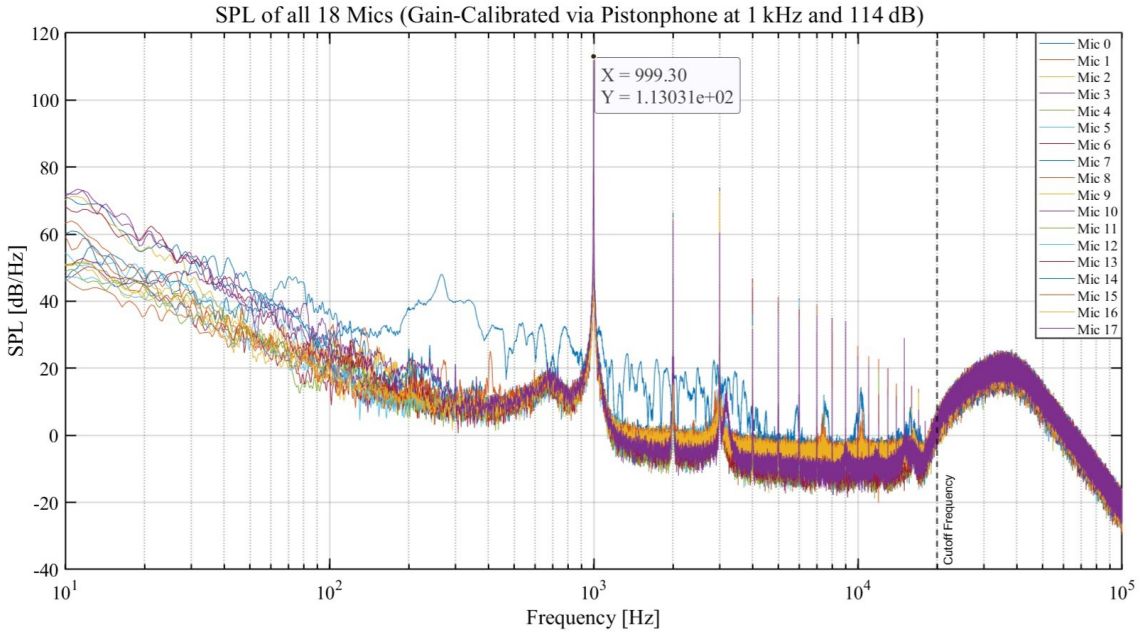

Figure A.6: SPL of all 18 microphones.

A.4 CASE B Plots

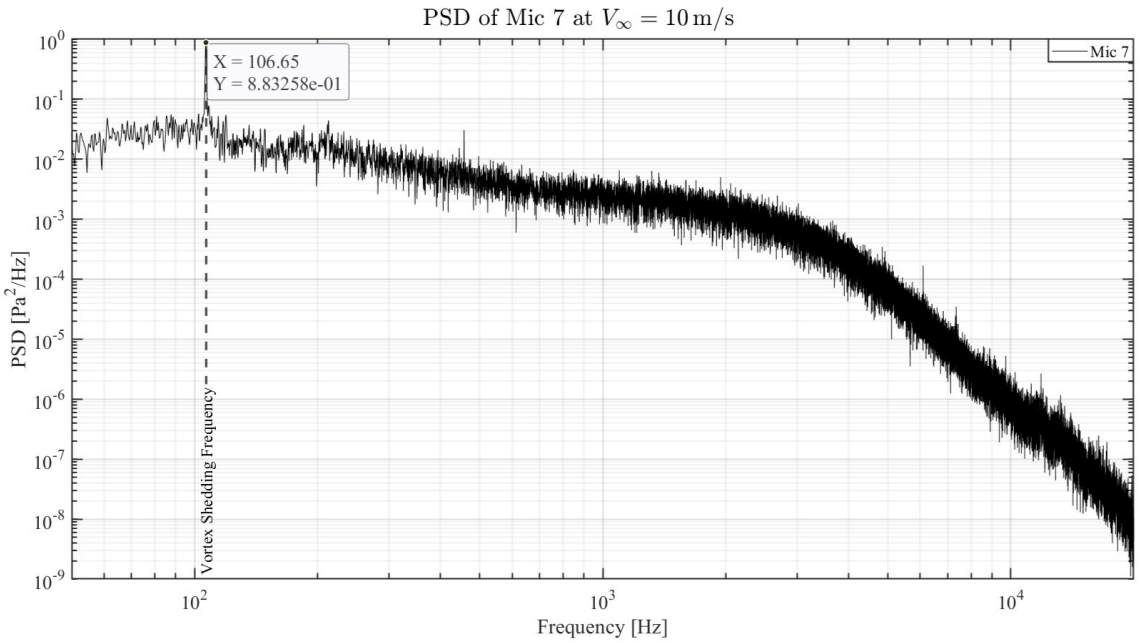

(a) $V_\infty = 10\,\mathrm{m/s}$

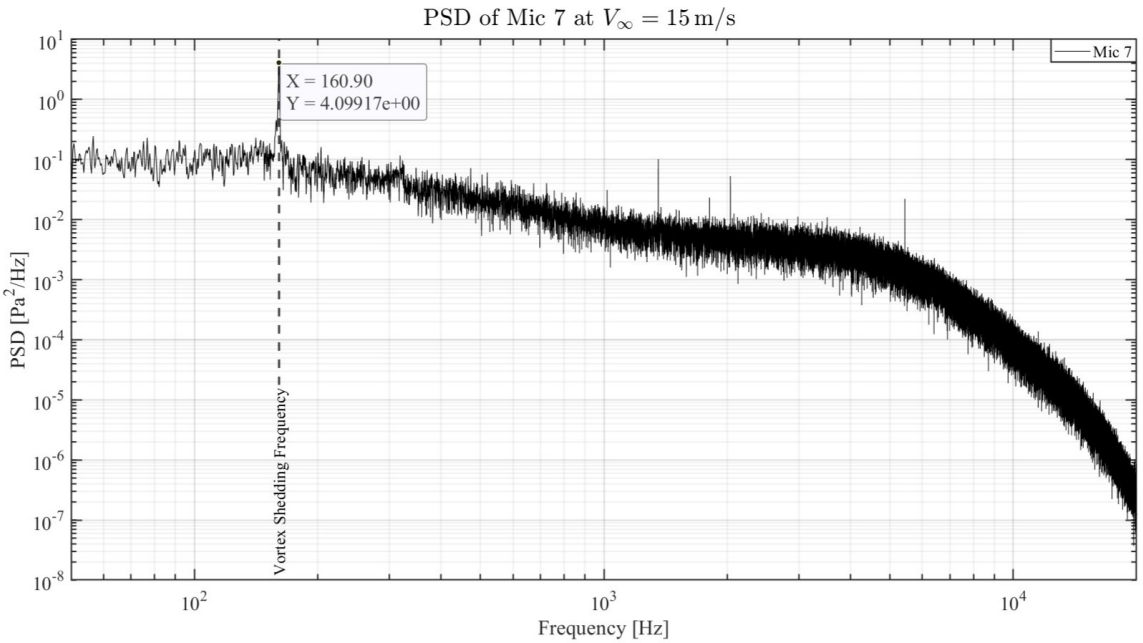

(b) $V_\infty = 15\,\mathrm{m/s}$

Figure A.7: Power spectral density (PSD) of Mic 7 for CASE B at two freestream velocities.

A.5 Pressure Sensors Validation

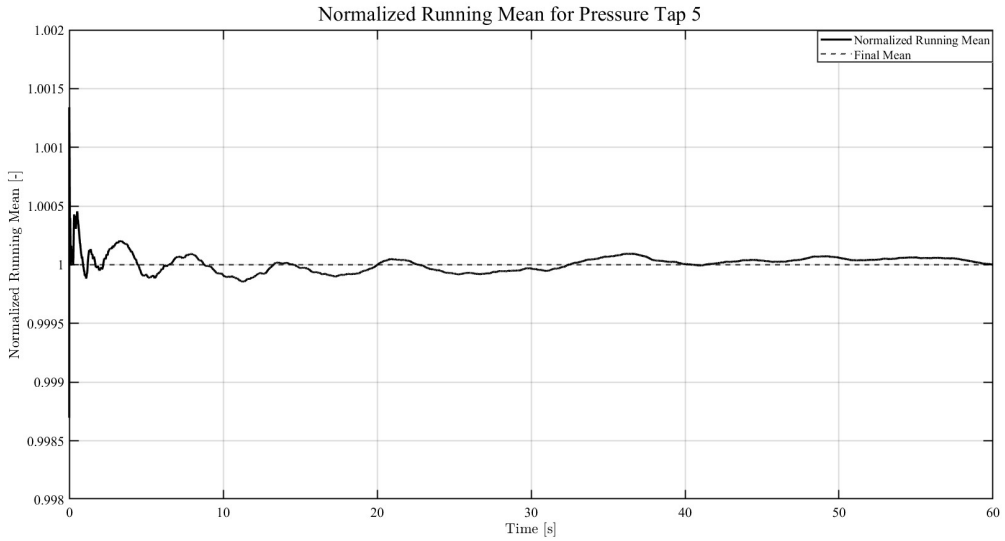

Figure A.8: Normalised running mean for pressure tap 5.

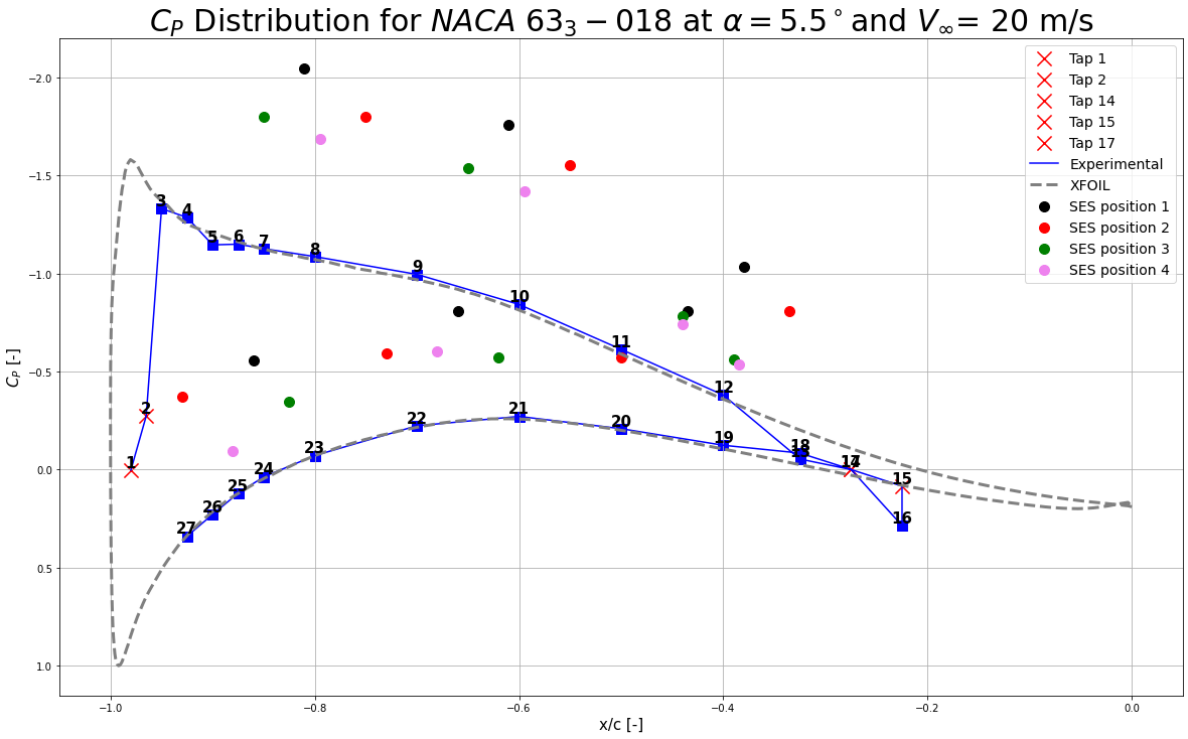

Figure A.9: Comparison of C_p distribution over the suction side of the NACA $63_3 - 018$ airfoil. The plot includes data from the pressure taps, predictions from XFOIL, and measurements from the embedded pressure sensors in the device. The results show the discrepancy in the measured data for the pressure sensors of the device with respect to the pressure taps and XFOIL data. For clarity: SES (Sensor Embedded Sleeve) in the figure legend denotes the flexible PCB device (referred to simply as the device).

A.6 Second Experiment Results

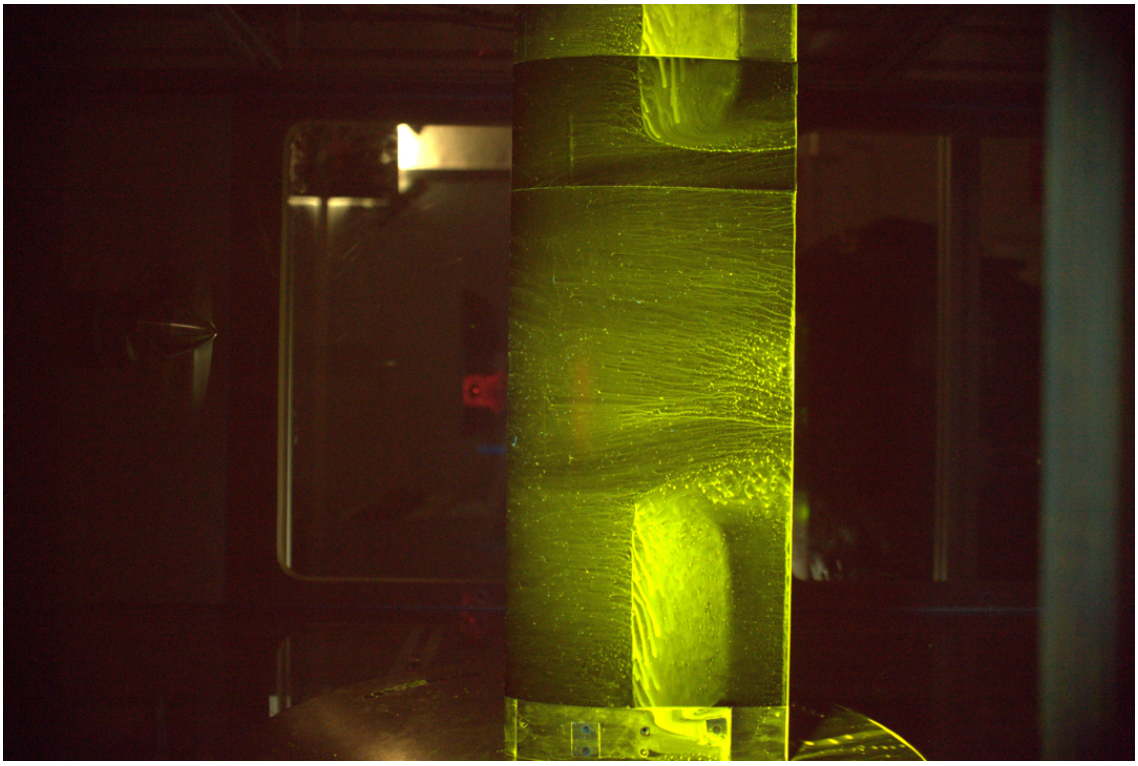

Figure A.10: Oil-flow visualisation for CASE01 ($0.8J$, $30°\beta$, $6°\alpha$) pressure side. See Fig. 4.1 for the propeller rotation direction and conventions.

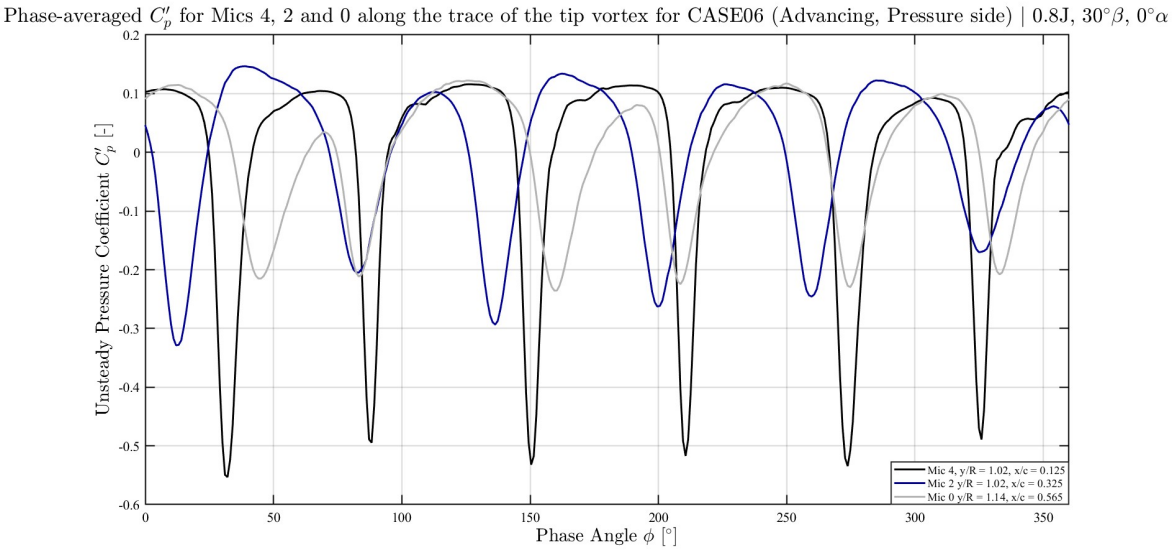

Figure A.11: Phase-averaged waveforms on the pressure side advancing blade side for Mics 4, 2 and 0 at different spanwise positions across the path of the tip vortex trace as seen in Fig. 4.16.

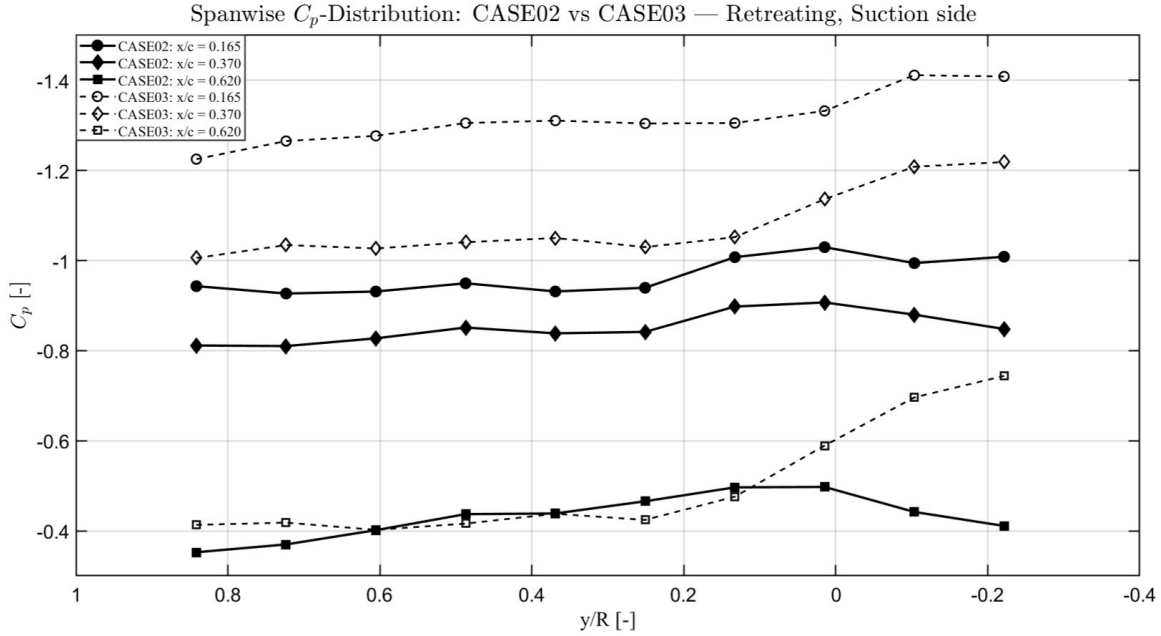

Figure A.12: Spanwise distribution of surface pressure coefficient (C_p) on the suction side of the airfoil model for CASE02 ($J = 1.8$, $30°\beta$, $6°\alpha$) and CASE03 ($J = 1.8$, $45°\beta$, $6°\alpha$). The results are shown for three chordwise pressure sensor locations ($x/c = 0.165$, 0.370, and 0.620). Each pressure sensor is denoted as 'P' followed by its sensor number.

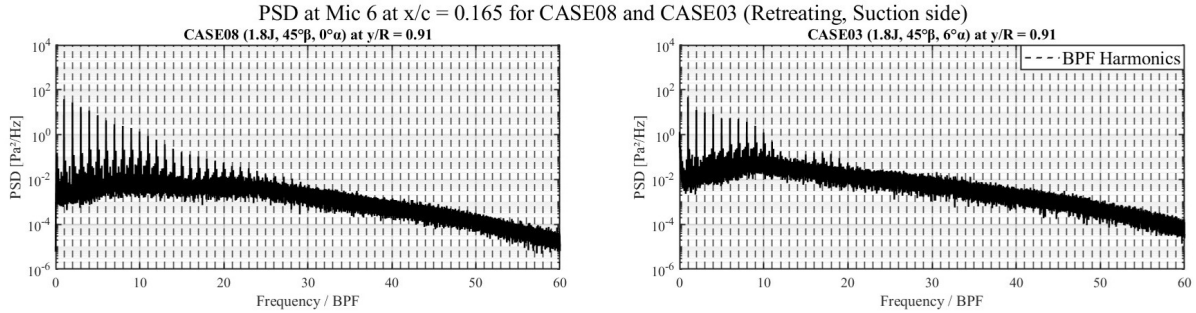

Figure A.13: The PSD corresponding to the mic and position of the low-pressure region of the trace of the tip vortex for the suction side retreating blade side for CASE08 and CASE03. The location corresponding to the lowest C_p' from the PLA is used for the PSD.

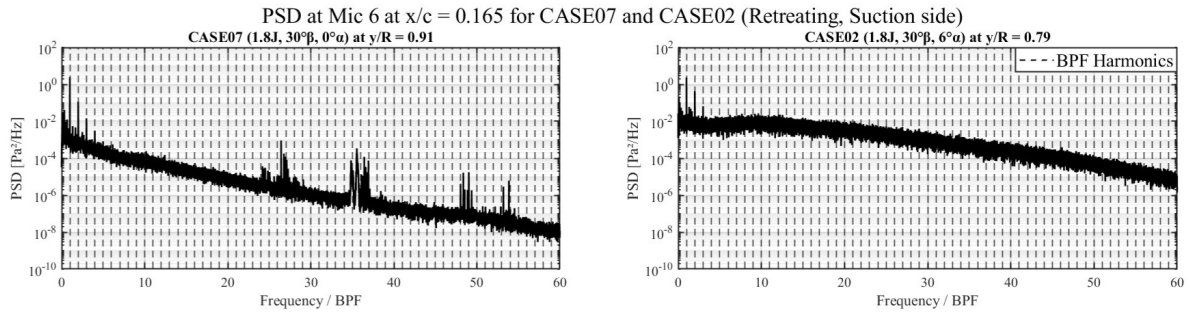

Figure A.14: The PSD corresponding to the mic and position of the low-pressure region of the trace of the tip vortex for the suction side retreating blade side for (a) CASE07 and (b) CASE02. The location corresponding to the lowest C_p' from the PLA is used for the PSD.

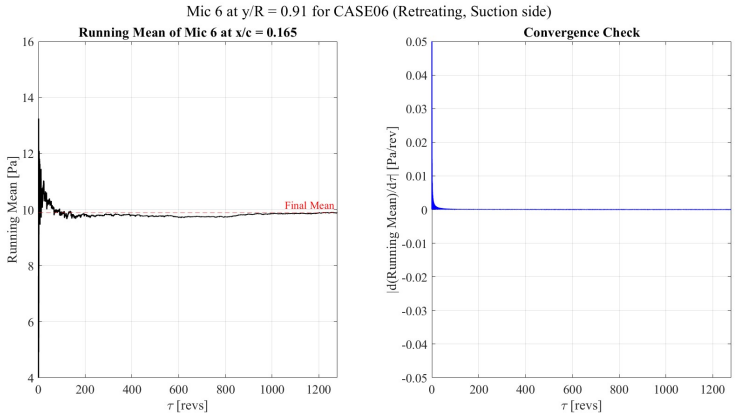

Figure A.15: CASE06 ($0.8J$, $30°\beta$, $0°\alpha$): (a) Running mean of Mic 6 over non-dimensional time τ. (b) Absolute value of the first derivative of the running mean with respect to τ, used to quantify the rate of convergence. The corresponding PLA can be referred to from Fig. 4.19. The scale has been adjusted for clarity.

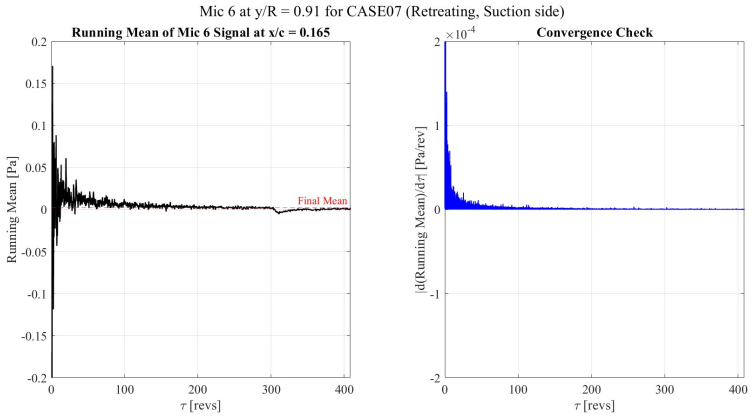

Figure A.16: CASE07 ($1.8J$, $30°\beta$, $0°\alpha$): (a) Running mean of Mic 6 over non-dimensional time τ. (b) Absolute value of the first derivative of the running mean with respect to τ, used to quantify the rate of convergence. The corresponding PLA can be referred to from Fig. 4.28. The scale has been adjusted for clarity.

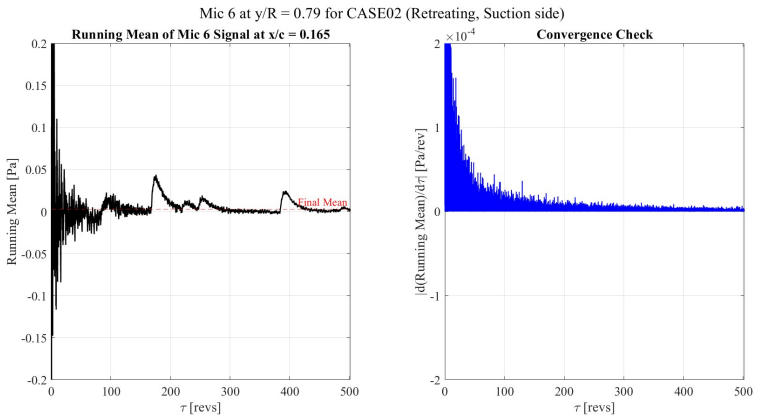

Figure A.17: CASE02 ($1.8J$, $30°\beta$, $6°\alpha$): (a) Running mean of Mic 6 over non-dimensional time τ. (b) Absolute value of the first derivative of the running mean with respect to τ, used to quantify the rate of convergence. The corresponding PLA can be referred to from Fig. 4.28. The scale has been adjusted for clarity.

For negative thrust cases, where the pressure fluctuation magnitudes are inherently low, the convergence of the first derivative, i.e. the rate of change of mean, rather than the running mean, serves as a more reliable indicator of statistical convergence. The first derivative is given by Eq. A.1.

$$\left|\frac{d(\text{running mean})}{d\tau}\right| \approx \left|\frac{\text{running\_mean}(i+1) - \text{running\_mean}(i)}{\Delta\tau}\right| \tag{A.1}$$

A.7 The High Frequency Harmonics

As seen in Fig. A.18, there is a peak at a fundamental frequency at $f/BPF \approx 12.45$, which corresponds to a frequency of approximately 4 kHz. Subsequent harmonics are observed at approximately 8 kHz, 12 kHz, and 16 kHz. To determine whether these peaks correspond to specific flow phenomena in a particular case, several comparisons are conducted.

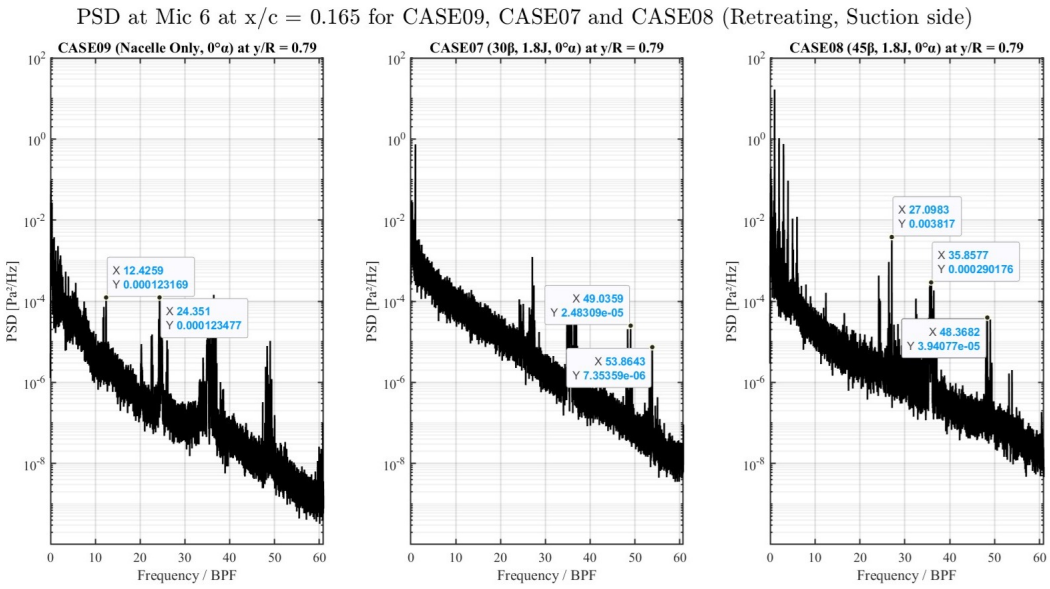

Figure A.18: PSD corresponding to Mic 6 at $y/R = 0.79$ for CASE09, CASE07 and CASE08. The first subplot highlights the first two harmonics of the fundamental frequency, the second subplot annotates the fourth harmonic, and the third subplot displays the second, third and fourth harmonics.

The PSD for the nacelle-only case with the tunnel off did not yield these peaks. Hence, it can be inferred that these peaks do not correspond to any electrical noise from the electrical equipment of the setup (apart from the propeller motor). However, the PSD for the nacelle only and propeller-on cases (see Fig. A.18) yielded these peaks, which meant that electrical remnants from the propeller motor are not responsible for these peaks since the motor was not operational during the nacelle only case. Furthermore, the role of structural vibrations in the propeller sting is also ruled out, as the peaks appear in the nacelle-only (propeller-off) cases.

In Fig. A.19, it is observed that the harmonics persist across different parts of the flow- at the LBL ahead of the LSB, inside the separated shear layer of the LSB, and the TBL downstream of the shear layer. The lower harmonics at the TBL are not visible due to higher broadband levels, but the harmonic corresponding to 16 kHz is visible in the TBL spectra.

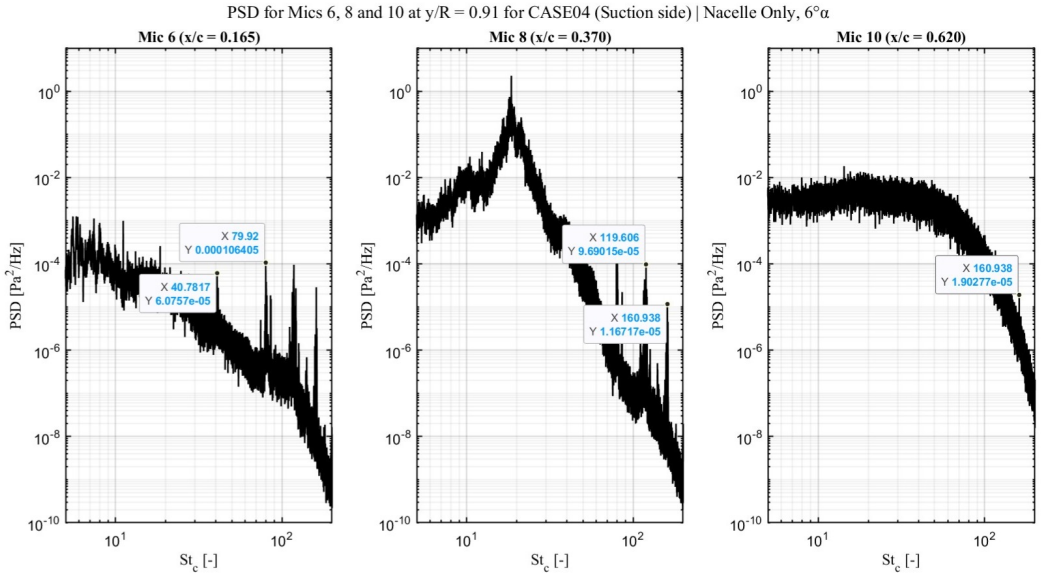

Figure A.19: PSD corresponding to Mics 6, 8 and 10 at $y/R = 0.91$ for CASE04. The first subplot highlights the first two harmonics of the fundamental frequency, the second subplot annotates the third and fourth harmonics, and the third subplot displays the fourth harmonic.

These observations indicate that these peaks cannot be attributed to a specific flow phenomenon, as they consistently appear across all cases under varying flow conditions and also across different regions of the flow field for a single condition. One plausible explanation is that these peaks arise from structural vibrations of the test section, induced by the flow in the wind tunnel, and occur irrespective of whether the propeller is operational, as long as the tunnel is operational.

A.8 Blockage Correction Tables

The τ_1 and κ_1 values used for the solid blockage boundary corrections are shown below in Fig. A.20 and Fig. A.21, respectively.

Tunnel shape		Body of revolution	Three-dimensional wing with span-to-breadth ratio				
			$\frac{2s}{B} = 0$	$\frac{2s}{B} = 0.25$	$\frac{2s}{B} = 0.50$	$\frac{2s}{B} = 0.75$	$\frac{2s}{B} = 1.00$
Circular		0.797	0.797	0.812	0.828	0.859	—
Square		.812	.812	.818	.836	.874	0.951
Rectangular	B/H = 10/7	.863	.863	.864	.866	.884	.916
	B/H = 7/4	.946	.946	.941	.930	.923	.937
	B/H = 2	1.028	1.028	1.017	.990	.967	.962
	B/H = 7/2	1.729	1.729	1.630	1.436	1.204	1.160
	B/H = 2/7	1.729	1.729	1.783	1.896	2.196	2.665
	B/H = 1/2	1.028	1.028	—	—	—	1.180
	B/H = 7/10	.863	.863	—	—	—	1.110

Figure A.20: Values of τ_1 for various tunnel shapes and configurations [35].

$\frac{t}{c}$ = 0.XX	Ellipse	Joukowski section	Conventional NACA sections 00XX	NACA low-drag sections			
				16-0XX	64-0XX	65-0XX	66-0XX
0.06	0.938	——	0.941	0.938	0.962	0.965	0.987
.09	.965	0.991	.972	.962	.961	.967	.984
.12	.993	1.016	1.005	.997	.987	.989	1.006
.15	1.019	1.045	1.035	1.028	1.019	1.020	1.032
.18	1.046	1.068	1.063	1.062	1.047	1.051	1.057
.21	1.072	1.083	1.090	1.090	1.073	1.079	1.079
.25	1.108	——	1.128	1.128	——	——	——
.30	1.152	——	——	——	——	——	——
.35	1.196	——	——	——	——	——	——
.50	1.329	——	——	——	——	——	——
1.00	1.772	——	——	——	——	——	——

Figure A.21: Values of κ_1 for various base profiles [35].